



EUROPEAN
COMMISSION

Community Research



CARBOWASTE

Treatment and Disposal of Irradiated Graphite and Other Carbonaceous Waste

Grant Agreement Number: **FP7-211333**



Deliverable D-3.3.2

Report on analysis of impurity and isotope sites before and after treatment

Author(s):

Dirk Vulpius, Kathrin Baginski, Christian Fischer, Corrado Rizzato, Markus Baier
Forschungszentrum Juelich GmbH (Germany)

Abbie Jones, Lorraine McDermott; University of Manchester (UK)

Daniela Diaconu; Institute for Nuclear Research Pitesti (Romania)

Document Number: CARBOWASTE-D-1211-3.3.2

Date of issue of this report: 21/11/2012

Project co-funded by the European Commission under the Seventh Framework Programme (2007 to 2011) of the European Atomic Energy Community (EURATOM) for nuclear research and training activities

Dissemination Level

PU	Public	
RE	Restricted to the partners of the CARBOWASTE project	
CO	Confidential, only for specific distribution list defined on this document	X

Start date of project: **01/04/2008**

Duration: **60 Months**

Distribution list

[illegible]

CARBOWASTE		
Work package: 3 Task: 3.3	CARBOWASTE document no: CARBOWASTE-1211-D-3.3.2 (e.g. May 2008 as date of issue: 0805)	Document type: D=Deliverable
Issued by: Forschungszentrum Juelich GmbH (DE) Internal no.: CW1211-Deliverable-3-3-2-final-c		Document status: Draft/Review/Final

Document title
Report on analysis of impurity and isotope sites before and after treatment
Executive summary
<p>There are many types and sources of irradiated nuclear graphite waste and therefore it is unlikely a comprehensive database of empirical data for all this waste could ever be achieved. Therefore to gain an understanding of the location and stability of impurities / radioactive isotopes in selected irradiated graphite waste before and after various treatments. The latest scientific techniques will be employed to investigate where and how impurities / radioactive isotopes are located within virgin and irradiated nuclear graphite. Thus leading to a robust understanding of the value of various treatment options.</p> <p>This understanding may then be called upon in deciding and validating the most appropriate options for the disposal of irradiated nuclear graphite waste, so that it is also valid to evaluate the direct disposal of graphite without treatment. The results that come out from this task will also be added to the characteristics database in task 3.2 and 3.5.</p> <p>In this Task UoM, CIEMAT, FZJ work in characterisation after and before treatment. CEA, SCK-CEN, INR participate in the characterisation of their waste forms without treatment. WP6 has been involved to provide evaluation criteria for direct disposal.</p> <p>The main results from this task are as follows:</p> <p>The locations and the chemical forms (chemical bonds) of radionuclides in neutron-irradiated nuclear graphite have been determined in order to develop principal strategies for the management of graphitic nuclear waste. Due to the relatively low concentration of radionuclides in neutron-irradiated nuclear graphite (< 1 ppm) direct spectroscopic methods are not applicable to investigate chemical structures. Therefore, methods by analogy have been applied. Such methods are investigations of the chemically detectable precursors of radionuclides in neutron-irradiated nuclear graphite and subsection of irradiated graphite to different chemical reactions followed by measurements of the radionuclide-containing reaction products by sensitive radiochemical methods. The paper discusses the applicability of these methods. The radionuclides investigated in this study can be divided into three parts: tritium, radiocarbon and metallic activation and fission products. Tritium can be bound in neutron-irradiated nuclear graphite as strongly adsorbed tritiated water (HTO), in oxygen-containing functional groups (e.g. C—OT) and as hydrocarbons (C—T). Radiocarbon is covalently bound with the graphite structure. The activity can be described by a homogeneously distributed part and a heterogeneously distributed part (enriched on surfaces or in hotspots). Metallic radionuclides can be bound as ions or covalent metal-carbon compounds. The distribution of all these radionuclides is mainly dependent on the distribution of their inactive precursors.</p>

Revisions						
Rev.	Date	Short description	Author	Review	Task Leader	WP Leader
00	dd/mm/yyyy	Issue	Name, Organisation Signature	Name, Organisation Signature	Name, Organisation Signature	Name, Organisation Signature
01	21/11/2012	First issue	Vulpus FZJ	Jones UoM	Vulpus FZJ	Pina CIEMAT
02	dd/mm/yyyy	2 nd Issue				

Table of Content

1. OBJECTIVES OF THE TASK	7
2. ACTIVATION PROCESSES & CHEMICAL REACTIONS	8
2.1 Tritium	8
2.2 Radiocarbon	8
2.3 Chlorine	8
2.4 Metallic Radionuclides	9
2.5 Radiation Damages	9
2.6 Wigner Energy	10
3. GRAPHITE SAMPLES	10
3.1 AVR Fuel Pebble Graphite	10
3.2 AVR Reflector Graphite	11
3.3 Merlin Graphite	12
3.4 Saint-Laurent A2 Graphite	13
3.4.1 General considerations about UNGG reactors	13
3.4.2 Saint-Laurent A2 reactor - short history	14
3.4.3 Graphite stack description	15
3.5 British Experimental Pile Grade Zero Graphite	18
3.6. TRIGA 14MW research reactor	19
4. METHODS FOR ANALYSES	19
4.1 Scanning Electron Microscopy	19
4.2 SIMS	21
4.3 RAMAN	22
4.3.1 UoM Raman Spectroscopy Studies	22
4.3.2 ENS Raman Spectroscopy Studies	24
4.4 X-Ray Photoelectron Spectroscopy	26
4.5 Porosimetry	26

4.6 X-Ray Diffraction	28
4.7 X-Ray Fluorescence Spectroscopy	29
4.8 Digital Autoradiography	30
4.9 Thermal treatment	30
4.10 Electrolysis	32
4.11 Multichannel γ spectrometry	33
4.12 Liquid scintillation measurement	38
5. LOCATIONS AND CHEMICAL BOUNDS OF IMPURITIES AND RADIONUCLIDES BEFORE TREATMENT	41
5.1 Structure of Nuclear Graphite, its Impurities and their Activation Products	41
5.2 Thermal Treatment	49
5.3 Electrolysis	61
6. SPECIAL EFFECTS ON ISOTOPE SITES AFTER TREATMENT	64
6.1 SIMS Analyses before and after Thermal Treatment	64
6.2 XPS Analyses before and after Thermal Treatment	87
7. EVALUATION OF TREATMENT OPTIONS	96
8. SUMMARY	97
9. REFERENCES	98

1. Objectives of the Task

Worldwide over 250,000 tons of neutron-irradiated graphite from nuclear reactors are temporarily retained in interim storage facilities and reactor stores. There is a lack of comprehensive concepts for the management or final disposal of contaminated nuclear graphite.

For the conditioning of neutron-irradiated nuclear graphite it is necessary to know the location and the chemical bond of contaminating radionuclides. Only with this knowledge, we can predict the release or retention characteristics of radionuclides in neutron-irradiated nuclear graphite. Starting from this knowledge, we are able to develop methods for treatment of used nuclear graphite with respect to safer final disposal or reuse of graphite for new nuclear and non-nuclear applications. Also the recovery of radionuclides like tritium and radiocarbon for commercial uses could be a favourable option on account of the worldwide increasing request of these rare isotopes. If we know the location and the chemical bond of these isotopes in neutron-irradiated nuclear graphite, we can easily develop chemical or physical methods for their recovery and enrichment.

The location and the chemical bond of radionuclides in neutron-irradiated nuclear graphite cannot be determined directly, for example by spectroscopic methods, because the concentration of radionuclides in neutron-irradiated nuclear graphite is extremely low (< 1 ppm). However, the problem can be solved only indirectly. The method applied in this study is to subject graphite samples to different chemical reactions and to measure the radionuclide-containing reaction products by sensitive radiochemical methods. This allows conclusions to be drawn concerning the original form and locations of radionuclides in neutron-irradiated nuclear graphite. Parallel to these experiments, it is necessary to study the physical and chemical structure of virgin and irradiated nuclear graphite. The purpose of this study is to know the matrix in which the radionuclides are bound. If the structure of the matrix is known, conclusions about how and where radionuclides may be bound can be drawn. The third important task is to determine the impurities in virgin nuclear graphite, which are later transformed in radionuclides by neutron irradiation in a nuclear reactor. Because these impurities are present in higher concentrations (some 100 ppm), the locations and chemical bonds of these impurities can be successfully determined in certain cases. In the same way, other impurities like oxygen or oxygen-containing compounds which can react with radionuclides to form volatile compounds can be determined. For these reasons, it is necessary to carry out a variety of well-focused and fine-tuned experiments and to compare the results of these experiments with each other. In evaluating all the data it is possible to make reasonable assumptions about the locations and chemical bonds of radionuclides in neutron-irradiated nuclear graphite.

There are many types and sources of irradiated nuclear graphite waste and therefore it is unlikely a comprehensive database of empirical data for all this waste could ever be achieved. Therefore to gain an understanding of the location and stability of impurities / radioactive isotopes in selected irradiated graphite waste before and after various treatments. The latest scientific techniques will be employed to investigate where and how impurities / radioactive isotopes are located within virgin and irradiated nuclear graphite. Thus, extensive information will be supplied, which will lead to a more robust understanding of the value of various treatment and disposal options.

This understanding may then be called upon in deciding and validating the most appropriate options for the disposal of irradiated nuclear graphite waste, so that it is also valid to evaluate the direct disposal of graphite without treatment. The results that come out from this task will also be added to the characteristics database in task 3.2 and 3.5.

The most important feature of irradiated graphite is the chemical purity of the original graphite. The initial chemical composition fundamentally controls the isotopes that become activated on irradiation, and hence determines the radionuclide inventory, and the ease with which it may be managed or disposed.

The radionuclide inventory of graphite is dominated by H-3, C-14 and Cl-36.

2. Activation Processes & Chemical Reactions

2.1 Tritium

Tritium is created throughout the graphite from lithium impurities, and diffuses at a slow rate to reach pore surfaces where it exchanges with adsorbed hydrogen bearing molecules. Adventitious tritium from ternary fission events will also tend to become absorbed at the pore surfaces. Release in normal operation then occurs through exchange with hydrogen bearing molecules in the coolant (hydrogen, water and methane in CO₂-cooled systems), creating a quasi 'steady state' [2].

2.2 Radiocarbon

The dominant route for formation of C-14 is previously speculated to be dominated via the reaction N-14(n,p)C-14. Nitrogen is incorporated into the graphite matrix because graphite manufacture is typically done in air. Nitrogen may also be present in varying concentrations in the coolant gas and may therefore be deposited on the graphite surface. A second, significant pathway is via C-13(n,γ)C-14. Production from either O-16 or directly from O-17 via O-16(n,γ)O-17(n,α)C-14 is a minor, but non-trivial, route in coolants containing oxygen isotopes [1].

2.3 Chlorine

The use of either chlorine gas or freons in the purification process of graphite manufacture to remove certain metallic impurities as their volatile chlorides, can lead to residual Cl-35 contamination. Chlorine-36, arising from activation of residual chlorine used in the graphite purification process, represents another significant contaminant of radioactive waste graphite. This isotope is important as it is long lived and poorly retarded by geological barriers.

In addition to the activated radionuclides, graphite may also be contaminated with radionuclides arising within the reactor circuit, from either fuel element failure or activation products circulated in the coolant.

2.4 Metallic Radionuclides

Radioisotopes from corrosion products and lesser impurities [2] may include: Ca-41, Fe-55, Ni-59, Ni-63, Co-60, Ag-110m, and Cd-109. Further, quantities of fission products (Sr-90, Zr-93, Tc-99, Pd-107, Cd-113m, Sn-121m, I-129, Ba-133, Cs-134, Cs-137, Pm-147, Sm-151, Eu-152, Eu-154, Eu-155, etc.), as well as some uranium and transuranic elements (mainly Pu-238, Pu-239, Pu-240, Pu-241, Am-241, Am-243, Cm-242, Cm-243 and Cm-244), will arise as a result of fuel failures during operation of the reactor, or from traces of uranium carried into the core on fuel-element surfaces after fabrication.

The radionuclide inventory of graphite can be divided into two categories:

- Short lived isotopes. These isotopes have short half-lives and decay to insignificant levels after a few tens of years. They may pose issues for handling graphite immediately after reactor shutdown, but are less relevant to the consideration of reactor graphite disposability due to NDA's current Safe Store policy which delays Magnox reactor decommissioning for 80 to 100 years. Short lived radionuclides typically include, Co-60 (half-life ~5.3 years) and H-3 (half-life ~12.3 years);
- Long-lived isotopes. These are key radionuclides for extraction during graphite treatment processing because they may pose radiological health issues through their release to the biosphere over the long term. These typically include, Cl-36 (half-life ~301,000 years), but principally C-14 (half-life ~5,730 years).

The source of the radionuclides in graphite is likely to be a combination of the activation of an original impurity in the graphite (some of which may be gas trapped in the closed pores) together with contamination introduced in the coolant during reactor operation.

The radionuclide inventory of any sample of irradiated graphite should be understood prior to treatment to enable the most appropriate technology to be selected. The treatment of irradiated graphite may offer the opportunity to separate the important radionuclides (such as C-14) from the less problematic radionuclides.

2.5 Radiation Damages

Nuclear graphite components are polycrystalline in nature and their physical irradiation property changes are dominated by irradiation-induced changes to the graphite crystallites. The effect of irradiation on the crystallites is to expand in one direction and shrink, to a lesser extent, in the other direction. The consequence of this crystal dimensional change on the polycrystalline graphite component is critically dependent on the manufacturing route and the irradiation temperature. The changes in bulk volume lead to corresponding changes in density [2].

The irradiation damage produced in graphite by energetic neutrons has been extensively studied because of the use of graphite as a moderator in thermal nuclear reactors. The effects of irradiation on the structure of graphite have also been reviewed by Bradford and Steer [3]. In the early stages of irradiation, crystal dimensional change rates may be slow and there will be little, if any, closure of porosity and increase in structural connectivity. As irradiation proceeds, the rate of graphite material growth in the c-axis will increase and the original thermal stress cracks produced during manufacture will be closed. The rate at which this occurs is initially

slow but increases as irradiation proceeds. This crystal shape change in the graphite matrix drives closure of porosity and an increase in the structural connectivity, causing the modulus to increase slowly.

Under continued irradiation, expansion along the c-axis will begin to strain the graphite structural network. Where this strain cannot be relieved by the breaking and reforming of connecting bonds, new porosity will be generated by microcracking. It was highlighted that due to the distribution of the pore and crystallite sizes, pore generation will not occur simultaneously and uniformly in all regions of the material. Consequently some regions of the bulk material will still be undergoing pore closure whilst others undergo pore growth.

Bradford and Steer [3] summarised that bulk dimensional change is the result of two processes; the underlying shrinkage of graphite crystalline and pore generation.

2.6 Wigner Energy

Irradiated graphite may contain stored Wigner energy. Wigner energy is energy stored within the graphite matrix in the form of displaced atoms. The quantity of accumulated stored energy is a function of fast neutron flux, irradiation time and temperature. The higher the irradiation temperature, the lower is the amount of stored Wigner energy. Wigner energy may be released if the graphite is heated to above its irradiation temperature, although a temperature in excess of 2000 °C is required to purge all Wigner energy [2].

It has been stated that in Magnox-type reactors, graphite temperatures lie in the range 180 – 360 °C and accumulation of Wigner energy is limited to the cooler regions and even here the total stored energy saturates at levels which ensure that release rates upon heating are comfortably below the specific heat capacity [4].

The potential risk of triggering an inadvertent release of Wigner energy during graphite decommissioning and treatment is recognised as being small for the UK commercial reactor fleet. However, a management strategy for graphite may require the safe release of any stored Wigner energy to be taken into account.

3. Graphite Samples

3.1 AVR Fuel Pebble Graphite

At the Jülich Research Centre a new type of high temperature reactors was developed. The operator was the Experimental Reactor Consortium (Arbeitsgemeinschaft Versuchsreaktor, AVR). The core of this reactor consisted of a pebble bed in which the fuel was embedded in graphite pebbles with a diameter of 60 mm. In these pebbles the fuel was dispersed as coated particles. The fuel zone of one pebble had a diameter of 50 mm and was enclosed by a 5 mm thick fuel-free graphite shell (see Figure 3.1.1). Flakings of this outer shell collected from the bottom of the reactor after irradiation as well as samples of virgin fuel pebble graphite were used for the following experiments.

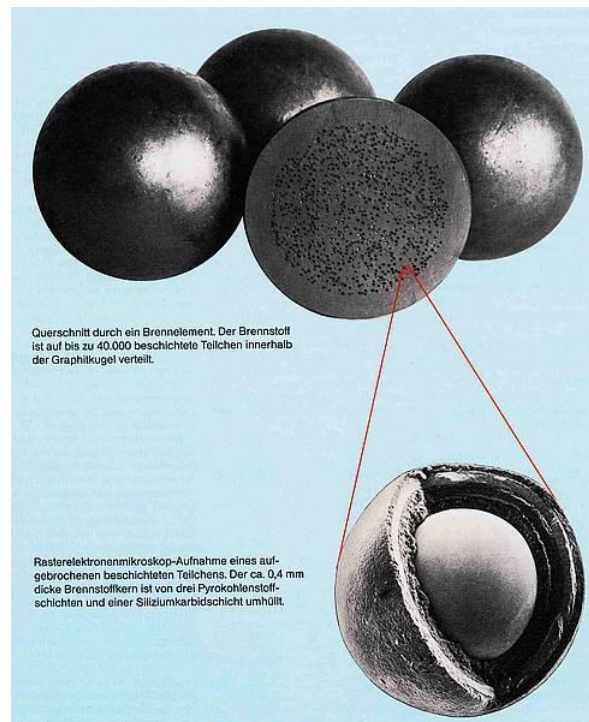


Figure 3.1.1: Sectional view of an AVR fuel pebble

3.2 AVR Reflector Graphite

The AVR reactor was a graphite-moderated gas-cooled high temperature reactor. Also the reflector was made of graphite (see Figure 3.2.1). In preparation of the dismantling of the reactor samples of the reflector have been taken. These samples as well as samples of virgin AVR reflector graphite were used for the described experiments.

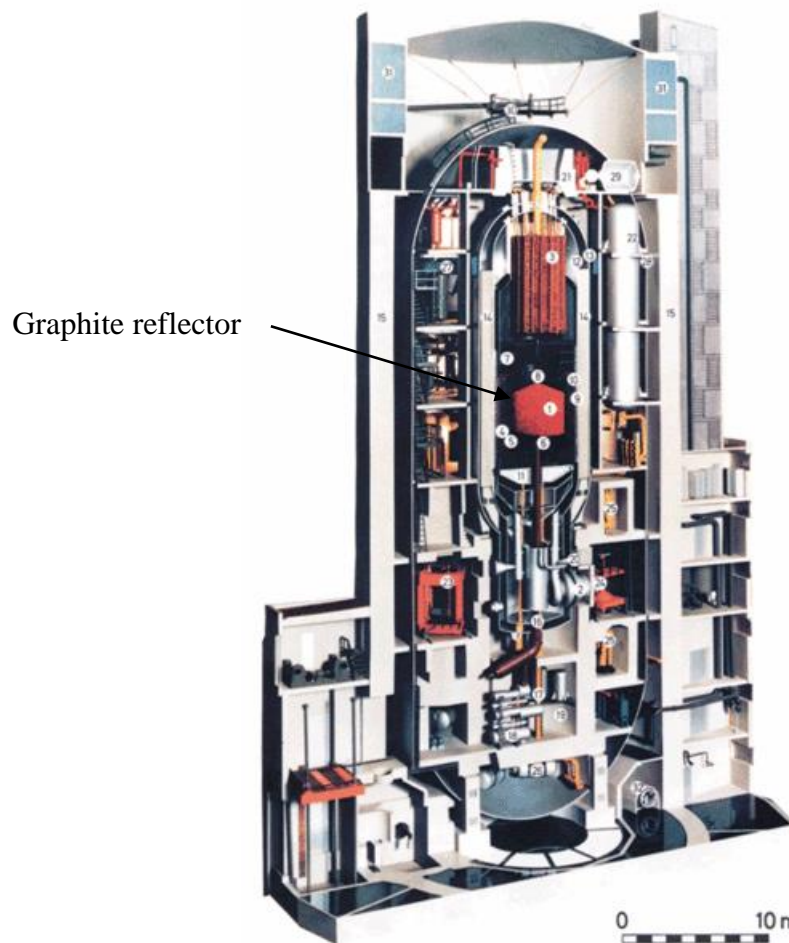


Figure 3.2.1: Schematic view of the AVR reactor

3.3 Merlin Graphite

At the Jülich Research Centre two types of material test reactors were in operation: the Merlin reactor or FRJ-1, a light water moderated swimming pool reactor, and the DIDO reactor or FRJ-2, a heavy water moderated reactor. During the dismantling process of the Merlin reactor irradiated graphite samples of the thermal column (see Figure 3.3.1) have been taken. These samples were used for experiments described in this report.

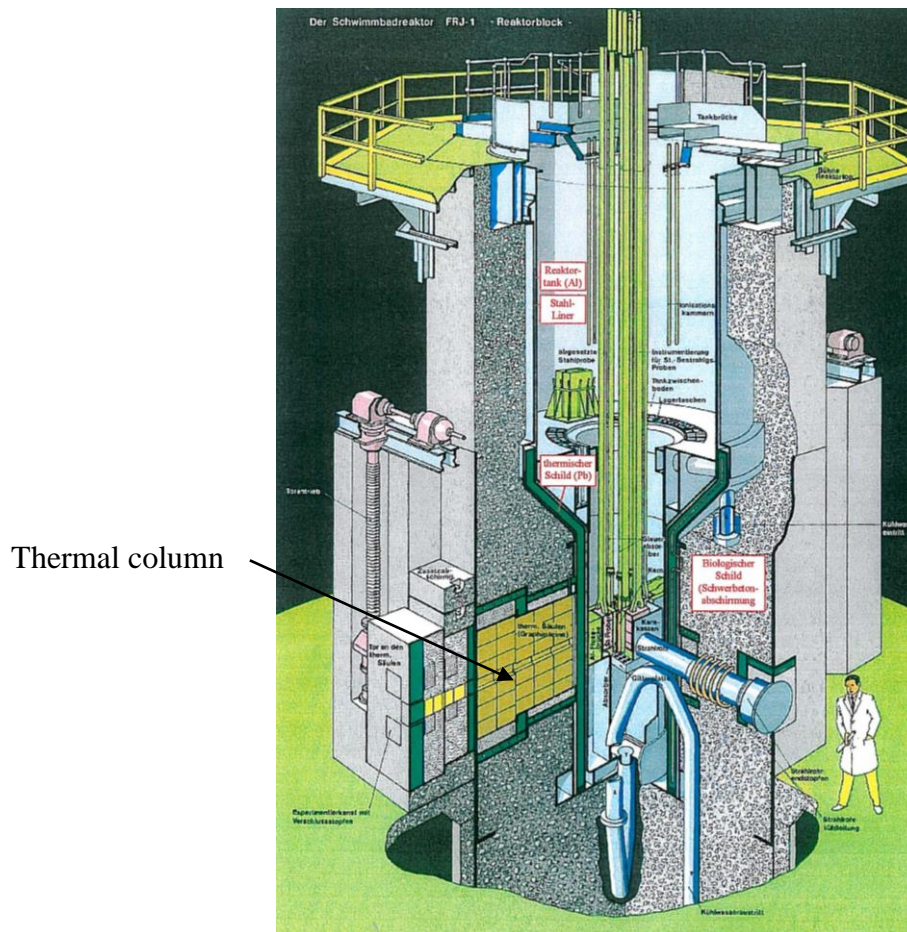


Figure 3.3.1: Schematic view of the Merlin reactor (FRJ-1)

3.4 Saint-Laurent A2 Graphite

The Saint-Laurent A2 reactor (see Figure 3.4.2) was a French UNGG reactor (Uranium Naturel Graphite Gaz). Irradiated graphite samples used in this report came from the 5120 mm position (near reactor kernel). Virgin graphite samples were also used.

3.4.1 General considerations about UNGG reactors

EDF (Électricité de France) operated in France six gas-cooled reactors, all shutdown now for at least fifteen years. These reactors are of so-called in French, “UNGG” reactor type (Uranium Naturel Graphite Gaz). They were graphite moderated, cooled by carbon dioxide and fuelled with natural metallic uranium.

The design of UNGG reactors is, in its general principle, very close to that of the British Magnox reactors, that was developed independently at the same period in United Kingdom. In the absence of uranium enrichment, graphite was used as a moderating material with a very high

level of purity due to the necessity of the highest transparency to neutrons. Graphite has been also chosen as a mechanical support of the fuel cartridges (graphite sleeves) and as a biological shield in some reactors. A scheme of the main possible uses of graphite in UNGG reactors is shown in Figure 3.4.1. The irradiated graphite from the pile or from the biological shield still lies in the reactors. The graphite sleeves that are not already shipped to the final repository are stored in silos.

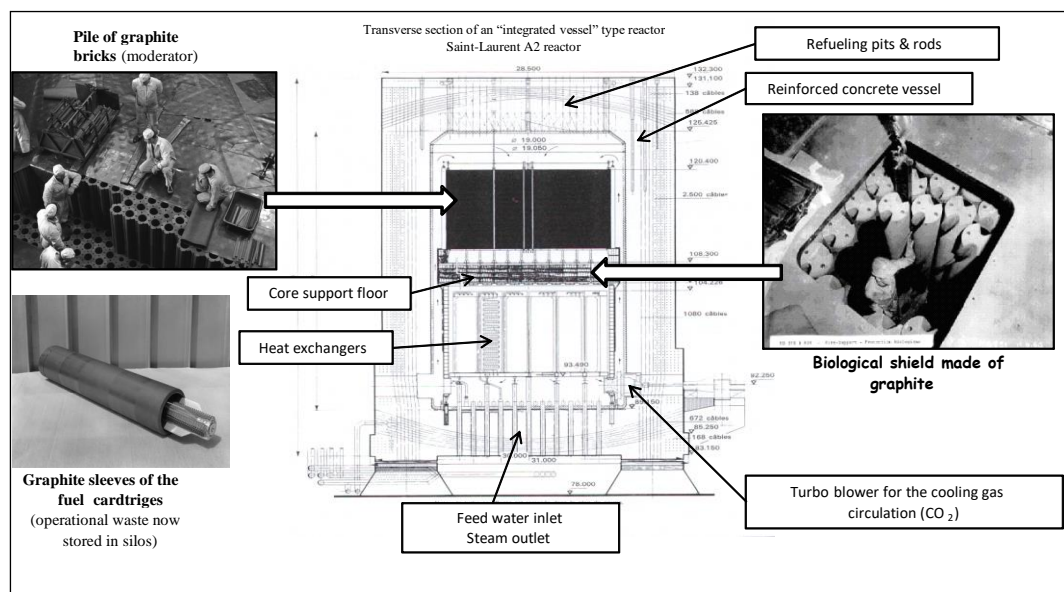


Figure 3.4.1: Uses of graphite in EDF UNGG reactors; different designs were developed, in this scheme an “integrated vessel” type reactor is presented (approximate external dimensions: 50 m height / 28.5 m diameter)

3.4.2 Saint-Laurent A2 reactor - short history

The Saint-Laurent A2 (SLA2) reactor was commissioned in August 1971. The pressure vessel of this reactor is built of pre-stressed concrete which also acts as biological shielding. The coolant is CO₂ which circulates from top to bottom at a pressure of 29 bar in the space between the graphite and the Mg-Zr alloy fuel cladding. The operating temperature ranges between 240 °C (top) and 470 °C (bottom). The thermal power is 1,700 MW. The gross electrical power is 530 MWe and the net electrical power in nominal operation is 515 MWe. The thermal neutron flux (from 10⁻⁵ eV to 0.5 eV) in the central zone of the core and in the maximum flux plane is $3.12 \cdot 10^{13} \text{ n cm}^{-2} \text{ s}^{-1}$.

It should also be noted that this reactor was shut down between March 1980 and September 1982 following an incident which led to the melting of two fuel elements at the bottom of the F5 M19 C14 channel (loss of cooling of the channel as a result of its obstruction by a metal plate, leading to overheating of the fuel elements).

The SLA2 reactor was finally shutdown on May 25, 1992. It was operated during 11 years full equivalent operating power. It has been de-fuelled and has been placed in a safe enclosure mode (ventilated by air with a moisture content limited to 50 %) until the final dismantling is performed.

EDF received the authorization to fully dismantle the SLA2 reactor by decree 2012-510 of May 18, 2010. All non-nuclear parts of SLA2 nuclear unit have been dismantled (dismantling IAEA level II achieved - figure 2). Up to now, final dismantling (level III) is planned by 2030-2040.



Figure 3.4.2: Saint-Laurent A1 (left) and Saint-Laurent A2 (right) UNGG reactors (current state 2012)

3.4.3 Graphite stack description

The graphite stack of the SLA2 reactor has the form of a cylinder with a vertical axis 15.73 m in diameter (13.43 m of moderator surrounded by a 1.15 m thick reflector) and 10.2 m high. The total mass of graphite is 2,440 tons including 1,580 tons of moderator and 860 tons of reflector (Figure 3.4.3).

The stack's network of graphite bricks is a hexagonal mesh with a pitch of 225.16 mm. The elementary graphite blocks are prismatic bars with a hexagonal base whose distance between two opposite faces is equivalent to the network mesh. The side-by-side juxtaposition of 4,429 bars forms a bed, the SLA2 stack consisting of 8 superimposed beds (bed No. 1 is that at the bottom of the stack). Thus, the bars are superimposed and the stack may also be regarded as the juxtaposition of 4,429 columns. The graphite stack comprises:

- The lateral reflector consisting only of 828 solid columns surrounding the core;
- The moderator (or core) consisting of 3,601 columns: 345 solid columns, 181 bored to 84 mm for the control rods and 3,075 columns bored to 140 mm (basically for the fuel elements).

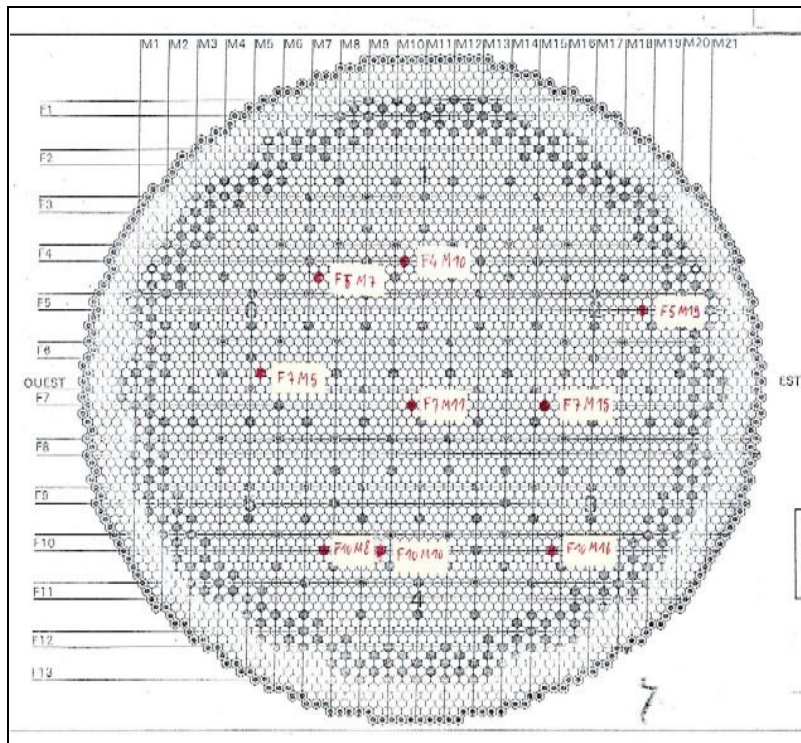


Figure 3.4.3: Section through the graphite stack of the Saint-Laurent A2 reactor - Juelich graphite cores were sampled from the F4M10 (hexagonal cell) C19 (fuel channel)

SLA2 Graphite

The graphite of SLA2 stack was manufactured by the Pechiney/SERS company between May 1966 and November 1967. This graphite was made from Lima coke, underwent one impregnation and was purified using MgF_2 . During its manufacture it was tested particularly with regard to effective cross-sections, density measurements and other properties described in the above table.

Ashes (ppm)	B (ppm)	Li (ppm)	Co (ppm)	Cl (ppm)	Thermal neutron absorption cross section (mbarn)	density
98	0.11	0.07	0.05	-	3.76	1.68

Concerning radionuclide inventory of the irradiated SLA2 graphite from the pile, it has been determined as described in Carbowaste report T-3.4.3 and corresponds to the following values for the main radionuclide of interest:

3H	^{10}Be	^{14}C	^{36}Cl	^{41}Ca	^{60}Co	^{63}Ni	^{137}Cs
$8.9 \cdot 10^4$	19.1	$7.7 \cdot 10^4$	37.9	83.7	$4.0 \cdot 10^3$	$3.5 \cdot 10^4$	47.0

These values are in Bq/g and related to January 2012. They take no account of the influence of leaching phenomena of the underwater dismantling process. They are over-estimated mean values as described in Carbowaste report T-3.4.3.

The radionuclide inventory for Cesium-137, a trace element for the fission reactions, shows that the decontamination operations adopted following the fuel element melting have been effective. In fact, this incident has no detectable effects in terms of contamination of the graphite. The levels of Cesium-137 are equivalent in all the EDF reactors whether fusion of fuel elements has occurred or not. The presence of Cesium-137 in very low quantities and the heavy nuclei produced are explained by the fission of traces of uranium present in the original graphite. These traces were identified in the analyses performed on the graphite at the time of their manufacture and now evidenced by the identification calculation-measurement method used for the radionuclide inventory assessment.

Core sampling

The SLA2 reactor stack was subjected to core drilling in 2005 during which 180 cores were extracted. Remote controlled tools introduced into the fuel channels of the stack were used. This technique is the same to the technique implemented for monitoring the wear of the graphite during operation. The remote-control tool (Figure 3.4.4) was introduced from accesses through the re-fuelling pits at the top of the reactor into the channels, and performed coring on either side of the graphite bricks (Figure 3.4.5) in the direction perpendicular to the channels with a diameter of about 20 mm.

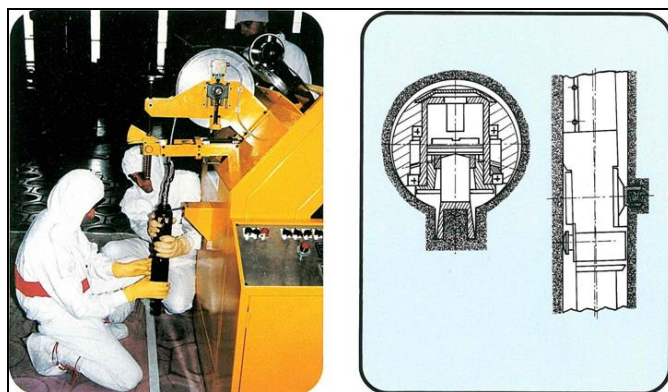


Figure 3.4.4: Remote controlled tool used for graphite stack sampling in UNGG reactors

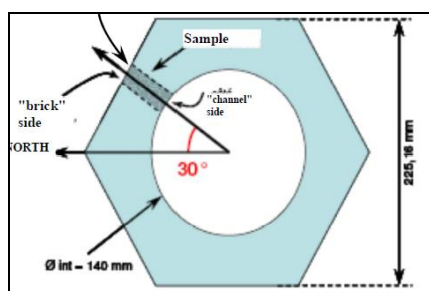


Figure 3.4.5: Schematic view of coring in a graphite brick

Samples sent to FZ Juelich

5 Samples were sent to Juelich coming from F4M10 cell C19 channel. They were chosen as being distributed over the height of the fuel channel in order to correspond to the operating temperature range in SLA2 reactor, as shown in the following table:

Adress	Height	Temperature °C	dose rate $\mu\text{Sv/h}$	Mass sample (g)
F4M10C19	1680	443	185	17,5
F4M10C19	2460	446	193	22
F4M10C19	5120	391	462	20,5
F4M10C19	7880	294	107	20,5
F4M10C19	9260	258	9	23

3.5 British Experimental Pile Grade Zero Graphite

British Experimental Pile Zero (BEPO) Energy Reactor was commissioned in 1948 and closed in 1968 and was one of the first UK experimental pile reactors to be built. BEPO was graphite moderated, air cooled and initially fuelled with natural uranium metal in aluminium cans. Two grades of enriched uranium fuel were used at a later date within the reactor. This reactor had a low power output of 6MW_T . BEPO was initially used for the production of plutonium however this was later transferred to the Windscale piles with BEPO function becoming principally that of a research reactor, which included isotope production and irradiation behaviour of graphite. In addition BEPO was used for the research of coolant compositions in Magnox and AGR systems.

The graphite used in this reactor core was sourced from Canada and referenced as AXGP [A3, A4]. Prior to sampling the BEPO core was annealed twice, firstly in 1954 then again in 1958 following the Windscale piles accident [A2, A5]. In 1975, a four inch core was trepanned from the BEPO core, the trepanned sample was drilled through the control face of the pile, steel shielding, concrete bioshield and the 20 columns of graphite blocks [A6]. From this a four inch core of the samples used for analysis at The University of Manchester. This four inch diameter core was initially taken in 1975 to provide radioisotope data on the graphite, steel and concrete, plus to evaluate the Wigner energy. This core was retrieved using a diamond-tipped hole cutter using no coolant or lubricant. After retrieval the core was re-sealed. Samples were obtained from channels 1, 13a, 16, 20 and 21, channel 1 is located at the core edge and channel 21 located at the core centre. The activity of each sample increases relative to the Fluence received and its location within the core [A6], Figure 3.5.1 shows the Fluence and activity of the samples utilised in this study.

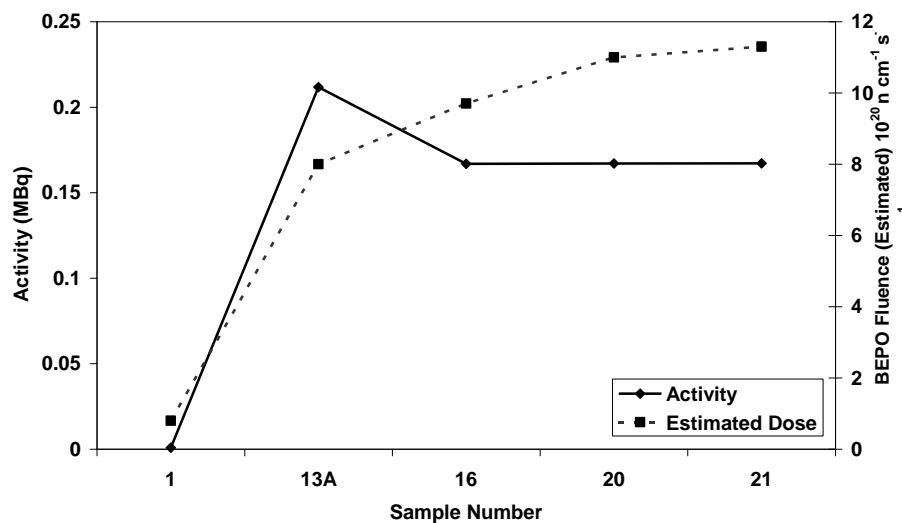


Figure 3.5.1: Estimated Fluence received by each channel analysed within the BEPO core and isotopic activity for BEPO channels analysed

3.6. TRIGA 14MW research reactor

The TRIGA reactor is actually composed of the material testing reactor (MTR) – Steady State Reactor TRIGA SSR (14 MW) and Annular Core Pulsing Reactor TRIGA ACPR.

The TRIGA reactor thermal column is a graphite block (1716x1144x710 mm) formed by 98 rectangular graphite cells (12 rows x 8 bricks) in aluminium cladding placed in the reactor pool, on the north side of the steady state core. A number of graphite cells are already removed from the thermal column and stored.

The graphite used in the thermal column of TRIGA reactor has been provided by an UK producer in the '50s and consists in sintered graphite blocks in aluminium cladding with a density of 1.63 g/cm³. The total graphite in a brick is 23.64 kg and the whole column weights 2.3 t. Original documents regarding the graphite characteristics have been lost and no data on the impurities content was available.

4. Methods for Analyses

4.1 Scanning Electron Microscopy

FZJ: A Quanta 200 FEG microscope (FEI Comp.) coupled with a device for energy-dispersive X-ray spectroscopy (EDAX, Inc.) was used.

INR: Scanning Electron Microscopy (SEM) & Energy-dispersive X-ray spectroscopy (EDS) – for morphology and impurities localization

Microstructure and elemental analysis of the virgin and irradiated samples were investigated using VEGA TESCAN Electron Microscope. Polished graphite samples have been prepared for elemental analysis while rupture surfaces have been used for morphology investigation. The virgin graphite microstructure showed a preponderant magma like structure resulted in the fabrication process (Figure 4.1.1), with embedded plates and micro-bares (Figure 4.1.2).

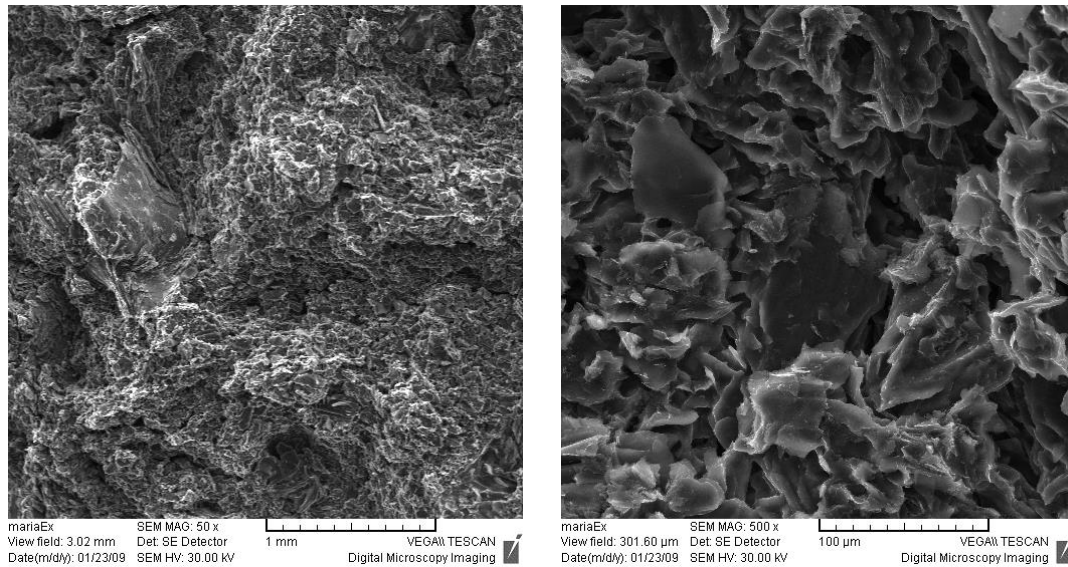


Figure 4.1.1: Virgin graphite microstructure – magma-like structure (left: x50; right: x500)

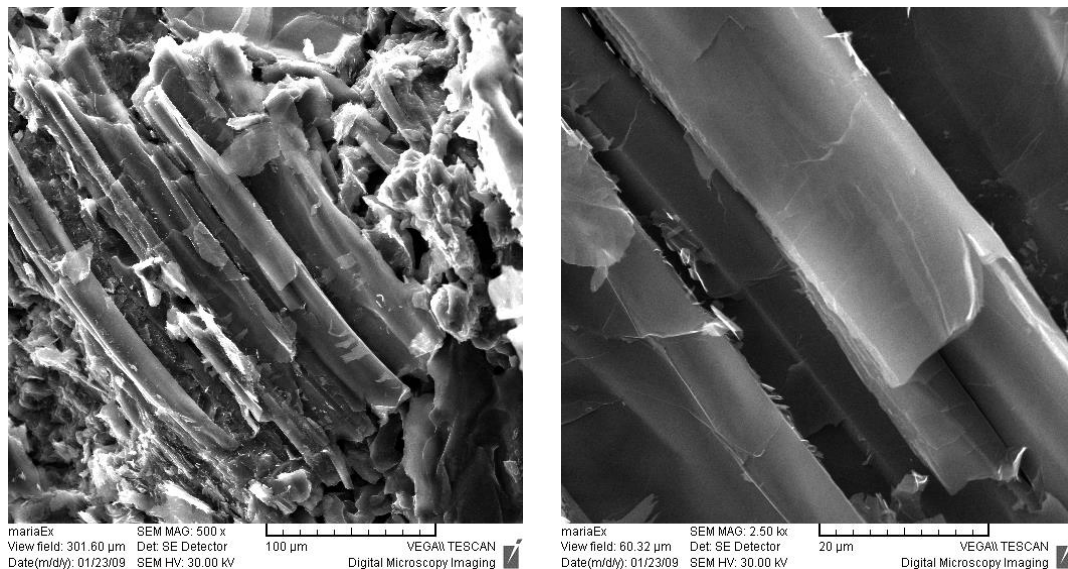


Figure 4.1.2: Embedded plates of graphite (left: x500; right: x2500)

Interconnected irregular large porosity (100-400 µm) alternates with smaller round pores (< 50 µm) – Figure 4.1.3. Porosity of virgin graphite sample was also observed with this technique, showing interconnected irregular large porosity (100-400 µm) that alternates with smaller round pores (< 50 µm)

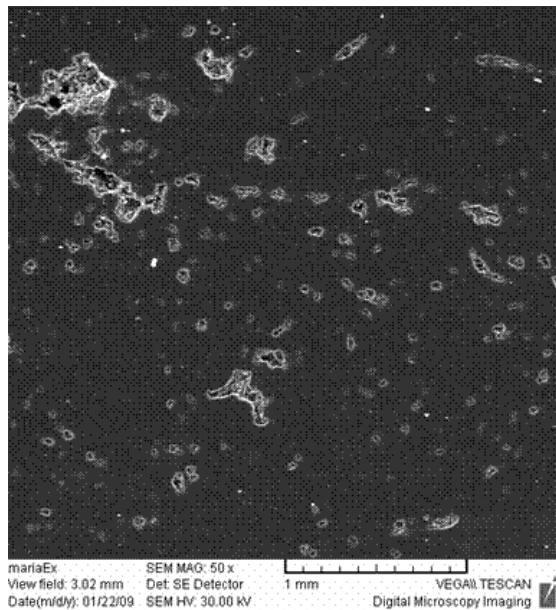


Figure 4.1.3: Porosity as shown by SEM for a virgin graphite sample

Impurities most frequently identified in the pores as small particles attached to the graphite plates are: Ca, Si, Ba, O. Other impurities found are: Cl, K, Na, S.

It should be mentioned that part of Si found on the sample surface could arise from the process of sample preparation for element analysis that supposes the polish with SiC. The distribution of the elements identified is shown in the Figure 4.1.4.

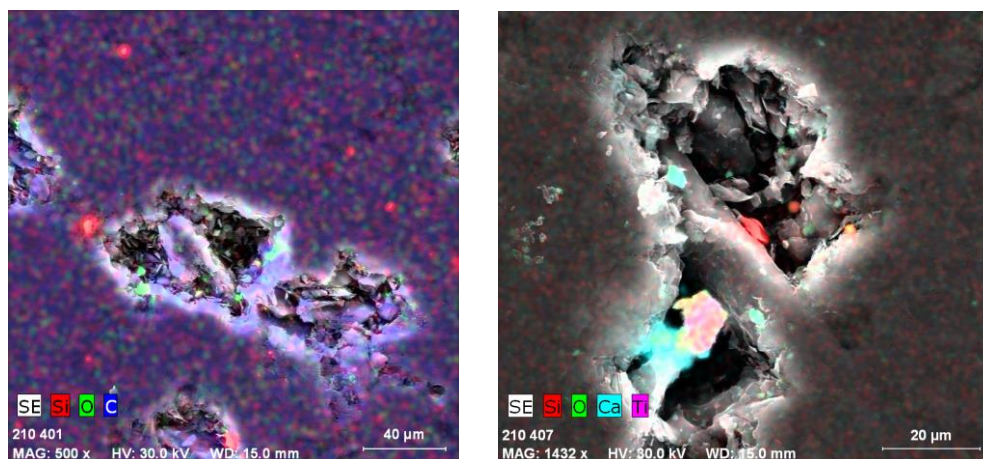


Figure 4.1.4: Secondary electrons image and elements distribution in virgin graphite

4.2 SIMS

FZJ: The SIMS measurements were made using a TOF-SIMS IV system (ION-TOF GmbH, Münster, Germany). This device is equipped with a time-of-flight ion detector so that mass resolutions are possible up to 0.001 mass units. Before each measurement, the mass scale was calibrated to the ^1H peak. The depth profiles were determined by evaluating the mass spectra of each graphite sample. In this way, small displacements of the mass scale were corrected so that depth profiles from different graphite samples were comparable.

4.3 RAMAN

4.3.1 UoM Raman Spectroscopy Studies

Raman spectroscopy is a technique which relies on the inelastic (Raman) scattering of light by the molecules within a material and is therefore, a non-destructive technique. In carbon materials Raman is used to determine the degree of crystallinity ranging from poorly ordered carbon to high order in graphite and diamond [7-11]. Principally, when a monochromatic beam of light impinges on a sample, a fraction of the light is scattered. The majority of this scattered light is elastically scattered. However, a small fraction is scattered at wavelengths different to that of the incident beam due to inelastic scattering. This change in frequency is called the Raman Effect. The resulting Raman spectrum corresponds to a particular bonding assignment. It is useful in the analysis of carbon- carbon bonding as one can ascertain information such as bonding type (sp^2/sp^3), structural characterisation, phase purity and crystallite size from the Raman spectrum.

The assignment of the band or peaks in the Raman spectrum is relatively straightforward in carbon materials and gives an insight into the molecular structure of carbon [10-11]. The G peak (located at 1580 cm^{-1}) is dominant in single crystalline graphite and is due to the bond stretching of all sp^2 atoms both in the aromatic rings and chains. This peak typically exhibits a FWHM (Full Width at Half Maximum intensity) value less than 20 cm^{-1} and is accompanied by the second harmonic (2D) at 2700 cm^{-1} which is indicative of highly crystalline graphite. In polygranular graphite and baked carbon material there is a D-peak present around 1350 cm^{-1} . This is assigned to the breathing mode of disordered sp^2 atoms in rings and may increase in intensity relative to the G-peak with decreasing crystallite size [11].

The degree of disorder within graphite has been studied by Tunstra and Koenig [12] who noted the ratio of the D-peak intensity to that of the G-peak varied inversely with crystallite size (L_a), where crystallite size was obtained from the FWHM of x-ray diffraction peaks:

$$\frac{I(D)}{I(G)} = \frac{C(\lambda)}{L_a} \quad (1)$$

Where C is the bond force constant of 4.4 nm at $\lambda = 514.5\text{ nm}$.

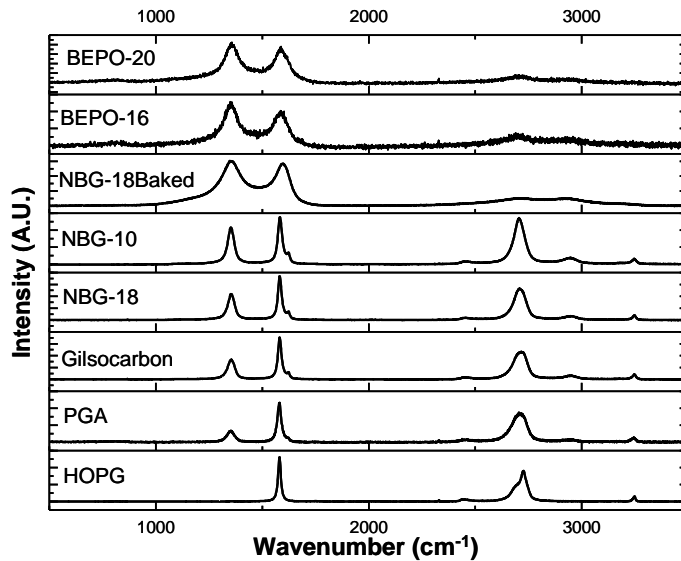


Figure 4.3.1: Raman Spectra of various nuclear graphite grades including VHTR grades and UK irradiated BEPO graphite

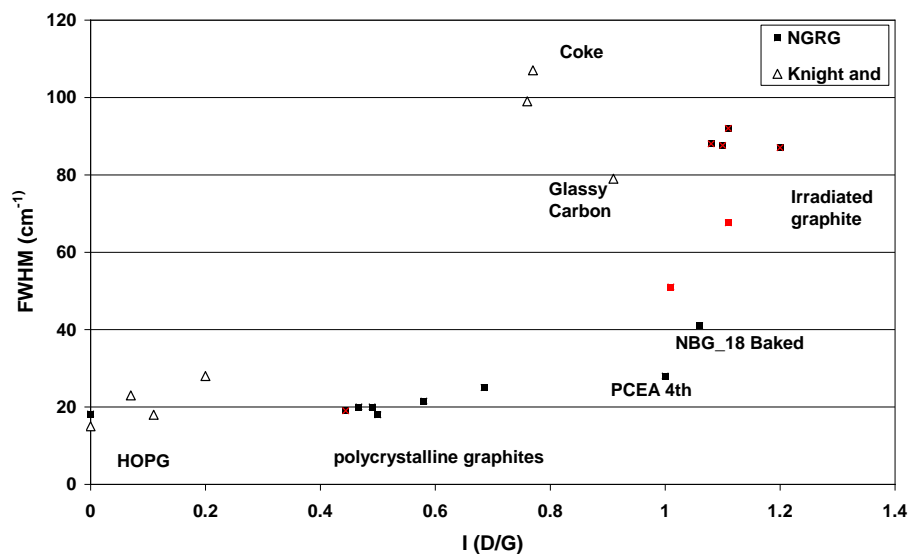


Figure 4.3.2: Raman ratio of $I(D)/I(G)$ against Full width half maximum of the G-peak to show the structural disordered of various nuclear graphite grades including VHTR grades and UK irradiated BEPO graphite

Figure 4.3.1 shows the Raman spectra of several polygranular nuclear graphites and irradiated nuclear graphite from the British Experimental Pile grade Zero (BEPO) reactor. A reduction in the G-peak intensity relative to virgin graphite and low irradiation BEPO graphite is evident with increasing fluence. The FWHM of the G-peak also increases in graphite samples which have undergone fast neutron irradiation. The irradiated graphite samples also show the magnitude of the D-peak increases with increasing fluence. This is indicative of increased structural disorder from the presence of both sp^2 and amorphous sp^3 carbon phases. Figure 4.3.2 shows

the Raman G-peak FWHM as a function of the I (D)/(G) ratio for various graphite and coke materials. Results from this group are compared with those of Knight and White [13]. The highly ordered pyrolytic graphite (HOPG) shows little peak broadening and is directly comparable with that of Knight and White. The general behaviour of unirradiated polycrystalline nuclear graphite is that the FWHM is less than 20 cm^{-1} and the I (D)/(G) ratio is below one. Neutron irradiated samples show larger values both in terms of FWHM and I(D)/I(G) ratio, similar baked graphite, coke and glassy carbon. These methods are now being used to quantify the effects of fast neutron irradiation and graphite manufacture on crystallite size and order/disorder within graphite crystals.

4.3.2 ENS Raman Spectroscopy Studies

Principally, ENS's work started by characterizing the virgin nuclear graphite of Saint Laurent des Eaux, France (SLA2), using Raman microspectrometry. This technique was particularly attractive due to the high spatial resolution ($\sim 1 \mu\text{m}$) achieved and that Raman provides less averaged information, in comparison with X-ray diffraction (XRD). Moreover, analyses were quick, operationally straightforward, non-destructive and requiring minimal sample preparation.

Compared to a single crystal of graphite (as for the Highly Oriented Pyrolytic Graphite (HOPG)), Raman spectrum of nuclear graphite exhibited additional bands labelled D for "Defect" bands, which are known to be characteristic for finite crystals of graphite. The polarization of the laser spot was used to distinguish preferentially oriented from randomly oriented crystals. Our result ensured that the nuclear graphite is composed of small crystallites more or less randomly oriented in the area of the laser spot. This aspect has been confirmed by X-ray Diffraction analyses.

Raman mapping of virgin nuclear graphite was performed, using the structural parameter R_2 , (D_1 area relative to the whole bands area). Compared to HOPG, virgin nuclear graphite featured a clear repartition on the defect band area. This showed the heterogeneity of the nuclear graphite, at a micrometric scale, in terms of the organization degree. This variation could be directly related to the composition of the nuclear graphite consisting in two main phases: the binder (coal-tar pitch) and the filler (petroleum coke) heated at 2800°C . Petroleum cokes are generally the more graphitizable of the two, and this aspect could give a noticeable decrease of the defect bands in Raman spectrum. Additional experiments are now initiated by combined Raman mapping, scanning electron microscopy and optical microscopy in order to distinguish between the binder and the filler in the nuclear graphite.

In order to select any treatment option for irradiated nuclear graphite, it is necessary to obtain a comprehensive understanding of the character in terms of the nanostructure of raw and modified graphite. Ion irradiation beam (implantation) may provide an effective way of the structural modification of graphite, where the structural defect could be similar to those induced by neutrons irradiations at varying fluences and temperatures. Moreover, such implantation can introduce a wide range of defects in a controlled manner.

Raman analyses showed an increase of defect bands with fluence in room temperature conditions, resulting in a disorder increase in the graphitic structure, until a complete amorphization for higher fluences characterized by an asymmetric broad single band. Compared to X-ray dif-

fraction, Raman microspectrometry appears as particularly sensitive to both the disorder and the amorphization, and may be achieved on very small volumes of matter (less than $0.1 \mu\text{m}^3$).

A more interesting finding occurred when we implanted the nuclear graphite at various temperatures. At high implantation temperatures (up to 600°C), the defect band in Raman spectrum decreased significantly suggesting that graphite defects recombine as fast as they form.

Analysis from Transmission electron microscopy (TEM) showed particularly interesting findings, in particular the 002 lattice fringe (LF) mode that allowed a direct imaging of the polyaromatic layers profile and consequently the access to the multiscale organization in the nanometer-micrometer range. The observation of the nanostructural changes caused by the ion beam irradiation at the surface or near the surface (implantation depth about $1 \mu\text{m}$) however, was not easily achievable by the conventional techniques such as hand grinding, ultramicrotomy and mechanical abrasion or ion thinning. The process which provided a great advance in the study of the ion-implanted graphite was the use of thin sections prepared by the focused ion beam (FIB) technique. In fact, its very important benefit was the easy and direct control of the choice of the area, the sample orientation according to the beam and the specimen thickness during ion milling (less than 100 nm that making it electrons transparent). By using thin sections prepared by FIB technique, we were able to image directly, for the first time, the structural modification due to implantation at the nanometre scale; this can be considered as a great improvement in the characterization of the ion-implanted graphite.

Our results showed a dramatic change of the polyaromatic layers organization at the surface, where the density of ^{37}Cl implantation was maximal. The graphite structure was strongly damaged without being completely amorphous: only short nanometer sized fringes forming small BSU (stacks of 2-3 layers) were visible and these stacks were strongly disoriented, losing the lamellar nanostructure of the virgin graphite. Geometrically speaking, such cross-linked BSUs form nanopores that could be considered as potential sites for radionuclides trapping.

The decrease of L_a , the coherent domain (BSU) diameter was also confirmed after ion beam irradiation by the measurement of the rotation moirés fringes in the 11DF dark field images, which was in perfect correlation with Raman results.

As we expected, the nanometer scale examination appeared extremely important to explore as it was planned at the beginning within the framework of Carbowaste program, based on our knowledge in carbon materials.

Irradiated graphite studies have recently begun on G2 samples issued from the nuclear reactor of Marcoule, France. The nuclear graphite was irradiated at a temperature close to 300°C . Compared to virgin graphite characterized by a weak defect band, Raman spectrum of irradiated graphite shows a slight increase of this later. This aspect has been confirmed by TEM observations with the 002 LF mode, for which the polyaromatic layers were slightly distorted. We attributed this relatively weak structural degradation of this irradiated graphite (about 4 dpa) to the irradiation temperature.

Presently, our experiments are in progress to study other irradiated graphite depending on their location in the UNGG reactor (which were submitted to other irradiation degrees and/or temperatures), and from other types of reactors. For this, a HRTEM image analysis will be used to acquire more quantitative structural data.

4.4 X-Ray Photoelectron Spectroscopy

FZJ: X-ray photoelectron spectroscopy was made using a 5600 XPS system (Physical Electronics, Inc., USA). Monochromatic Al-K α radiation (13 kV, 300 W) was applied as excitation source. Overview spectra (187 eV pass energy, 1 eV step increment) and core level spectra of C1s and O1s (5.85 eV pass energy, 0.025 eV step increment) were recorded.

4.5 Porosimetry

UoM: Manufactured nuclear graphite has a finite porosity prior to irradiation. Extensive networks of interconnected pores, leading from the surface to the core are also a common feature. These are referred to as ‘open’ pores, isolated pores being referred to as ‘closed’. The graphite structure in terms of open and closed porosity for the main UK graphite is provided in [5]:

In Magnox reactors, two types of graphite were used in core construction:

- Pile Grade A (PGA), primary graphite used for moderators
- Pile Grade B (PGB), mainly used for reflectors

Both materials were manufactured by a similar process, but PGA has a higher density than PGB. During manufacture PGA material was subject to additional heat treatment to reduce porosity and therefore increase its density. The resulting virgin PGA material has a porosity of approximately 20% [6].

A significant proportion of the porosity is open to the coolant circuit in gas-cooled reactors. In consequence, deposition of activated materials can occur both upon the geometrical surfaces of graphite components and on internal pore surfaces, especially where there are permeable gas flows through the graphite blocks due to pressure differentials [1].

Most of the graphite surface area of nuclear graphite is contained within the graphite pores. Therefore, the majority of radiolytic oxidation is likely to take place at the surface of the open pores of the graphite core. During radiolytic oxidation, the graphite that forms the surface of the open pore is eroded by interaction with coolant CO₂. Radiolysis of CO₂ produces an oxidising species (O_x) which can either react with an adjacent graphite surface, or be deactivated by a sequence of reactions involving CO. Attack is most aggressive in small pores where the surface area: volume ratio is high. Grain boundaries are also aggressively eroded, enabling open pore networks to grow by linking together with closed pores. The corrosion rate of graphite can reasonably be expected to be a function of the accessible pore volume.

It has been well documented that radiolytic oxidation leads to graphite weight loss. In Magnox graphite the weight loss originates from the opening up by oxidation of the open-pore structure and, at the higher weight losses, much, if not all, of the closed porosity is also opened up. The dependence of oxidation rate of open pore volume has been demonstrated for PGA graphite in CO₂. It has been shown that up to 40 % of the initially closed-pore volume can become accessible by 2 % weight loss in CO₂ [7].

The study of the pore morphology in nuclear graphite has traditionally been carried out using methods such as:

- Optical microscopy;
- Scanning electron microscope (SEM); and
- Transmission electron microscope (TEM).

Although valuable, these techniques only reveal details of the surface of the structure, and do not give a 3-D image. Such a 3-D image may be provided by X-ray micro-Tomography (XRμT), which may be applied to study the microstructure of nuclear graphite. This technique has been used by Sun *et al.* [8] to provide a non-destructive measure of the porosity of graphite before and after irradiation.

INR: Graphite porosity was investigated using a Quantachrome porosimeter.

Porosity characteristics are important in the assessment of contaminant release from the graphite matrix. The pores volume in virgin samples measured by mercury porosimetry ranges between 0.18 – 0.20 cm³/g. The open porosity available for water flow is therefore varying between 0.28 – 0.32 cm³/g.

The macro-porosity consists in pores having diameters in the range of 4 – 300 μm while the micro-porosity is formed by pores with diameters between 0.007 and 4 μm.

The macro- and micro- pores are grouped in 4 classes, the most significant with more than 75% being the pores with diameters of 2 and 7 μm respectively.

Table 4.5.1: Characteristics of porosity distribution in virgin graphite

Pore size range (μm)	Most probable pore size (μm)	Volumetric fraction (%)
0.008 – 0.04	0.01 and 0.022	1 -10
0.04 – 0.17	0.1	2 - 5
0.17 - 5	2	35
5 - 30	7	40
30 -300	180	10

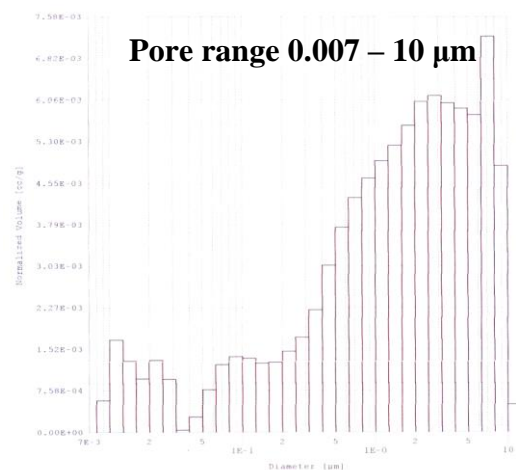
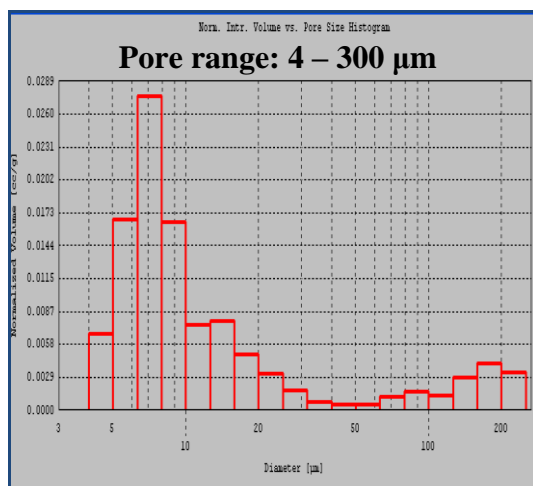


Figure 4.5.1: Macro - porosity (left) and micro-porosity (right) distribution in virgin graphite

4.6 X-Ray Diffraction

INR: X-Ray Diffraction was used in order to investigate the structure of graphite. Samples analysed consisted of small blocks of virgin graphite. The carbon crystallizes predominantly in a hexagonal lattice having a and b equal to 2.47 \AA , and $c = 6.79 \text{ \AA}$, but cubic carbon (C-60) and fullerenes with hexagonal lattice have been also found (Table 4.6.1). Both components identified by XRD (Figure 4.6.1) have been formed during the fabrication process and have larger lattice sizes compared to the hexagonal carbon.

Table 4.6.1: Crystallographic parameters of carbon systems

	Graphite	Carbon	Fullerene
Crystal system:	Hexagonal	Cubic	Hexagonal
Space group:	P63mc	Pa-3	PE
Space group number:	186	205	
$a \text{ (\AA)}$:	2.4700	14.0478	10.0390
$b \text{ (\AA)}$:	2.4700	14.0478	10.0390
$c \text{ (\AA)}$:	6.7900	14.0478	16.4350
Alpha ($^\circ$):	90.0000	90.0000	90.0000
Beta ($^\circ$):	90.0000	90.0000	90.0000
Gamma ($^\circ$):	120.0000	90.0000	120.0000
Volume of cell (10^6 pm^3):	35.88	2772.20	1434.44
Z:	4.00	4.00	2.00
RIR:	2.37	1.67	

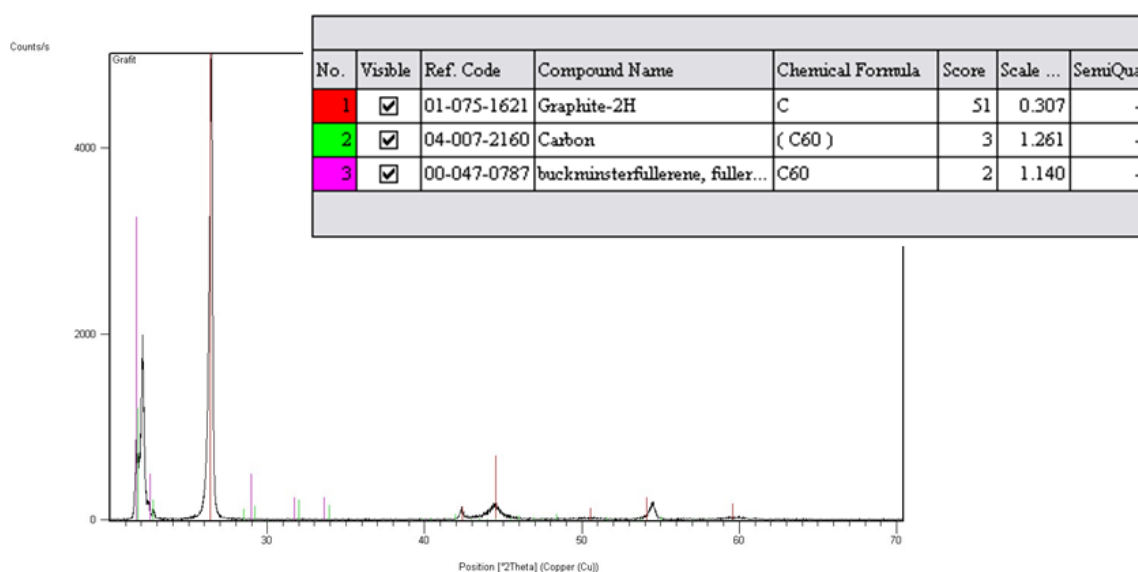


Figure 4.6.1: XRD spectrum of virgin graphite

4.7 X-Ray Fluorescence Spectroscopy

INR: X-Rays Fluorescence Spectroscopy has been used to confirm the presence of the impurities identified by SEM on the same samples. The sensitivity limit of the method is in the order of ppm and does not allow the identification of Co and Eu.

Even if theoretically this technique should cover all range between B to U with a sensitivity limit of 1 ppm, practically it is possible to measure elemental compositions starting from Na. Therefore the concentration of nitrogen (N), important to be known for C-14 estimation in Monte Carlo simulations, cannot be measured.

The impurities concentration obtained by XRF (Table 4.7.1) confirms the presence of Na, Ba, Si, Cl, Ca, S and K identified by EDS, and additionally revealed the presence of new elements as Mg, Th, Dy, Al and P. According to these data, Na, Ba and Si are the impurities with the higher content but they are not responsible for the graphite radioactivity after irradiation.

Two virgin graphite samples were analysed and the impurities detected are presented in Table 4.7.1.

Table 4.7.1: Impurities detected in the two samples investigated

<i>Sample #1</i>		
Element	Mass percent (%)	Standard error
Na	0.0628	0.0033
Ba	0.0229	0.0085
Si	0.0173	0.0010
Mg	0.0070	0.0009
Cl	0.0063	0.0007
Ca	0.0038	0.0005
S	0.0031	0.0003
Th	0.0023	0.0009
Dy	0.0021	0.0008
K	0.0018	0.0005
Al	0.0011	0.0003
P	0.0011	0.0003
<i>Sample #2</i>		
Element	Mass percent (%)	Standard error
Al	0.109	0.005
Na	0.0420	0.0021
Mg	0.0245	0.0012
Sn	0.0232	0.0012
Fe	0.0140	0.0007
Si	0.0127	0.0006
Ca	0.0082	0.0004
Cl	0.0059	0.0007
Mo	0.0025	0.0007
S	0.0020	0.0001
K	0.0012	0.0003
Cr	0.0011	0.0001
Ba	0.0037	0.0033

4.8 Digital Autoradiography

FZJ: Digital autoradiography was made using an Instant Imager A20240 (Canberra Packard Corp.). In principle, this system is a proportional counter tube equipped with a Microchannel Array Detector (MICAD) and a Multi-Wire Proportional Counter (MWPC). In this way, β^- particles, Auger electrons and Compton electrons are detectable with spatial resolution.

4.9 Thermal treatment

FZJ: The experimental set-up for thermal treatment of neutron-irradiated nuclear graphite has been previously described by Fachinger et al. [1]. In this study, the system was modified. Firstly, the number of gas washing bottles was increased from five to eight: two gas washing bottles were installed between the gas analyser and CuO oxidiser in order to capture primarily released $^{14}\text{CO}_2$, and an additional gas washing bottle was installed after the first gas washing bottle in order to fully capture primarily released HTO (see Figure 4.9.1).

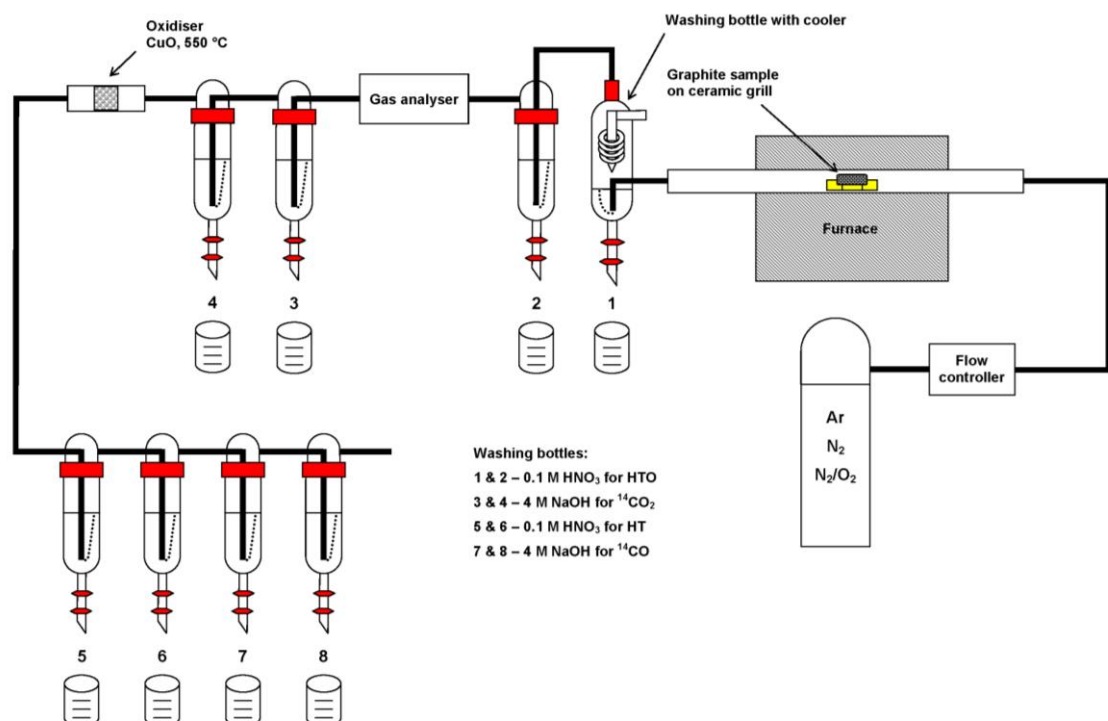


Figure 4.9.1: Experimental set-up for thermal treatment

Secondly, a new sample holder was designed. This was necessary because in the original holder design the gas only flowed around the sides and the top of the graphite samples. The original sample holder was a ceramic boat in which the graphite sample sat. Thus, the lower part of the sample was not treated as intended, as can be seen in Figure 4.9.2. Therefore, a new sample holder was designed. This sample holder consists of a truncated alumina tube with transversely arranged rods like a grill (see Figure 4.9.3). In this way it is guaranteed that the whole graphite sample is accessed by the treatment gas.



Figure 4.9.2: Incompletely treated graphite sample with the original sample holder



Figure 4.9.3: New sample holder

The efficiency of the new sample holder compared to the original design was demonstrated by calculating the flow pattern using the computer code ANSYS [2]. In Figure 4.9.4 can be seen that the original sample holder generates strong turbulences and that large parts of the sample are not or insufficiently accessed by the treatment gas. This problem which could lead to misinterpretations of the treatment results is solved with the new sample holder design.

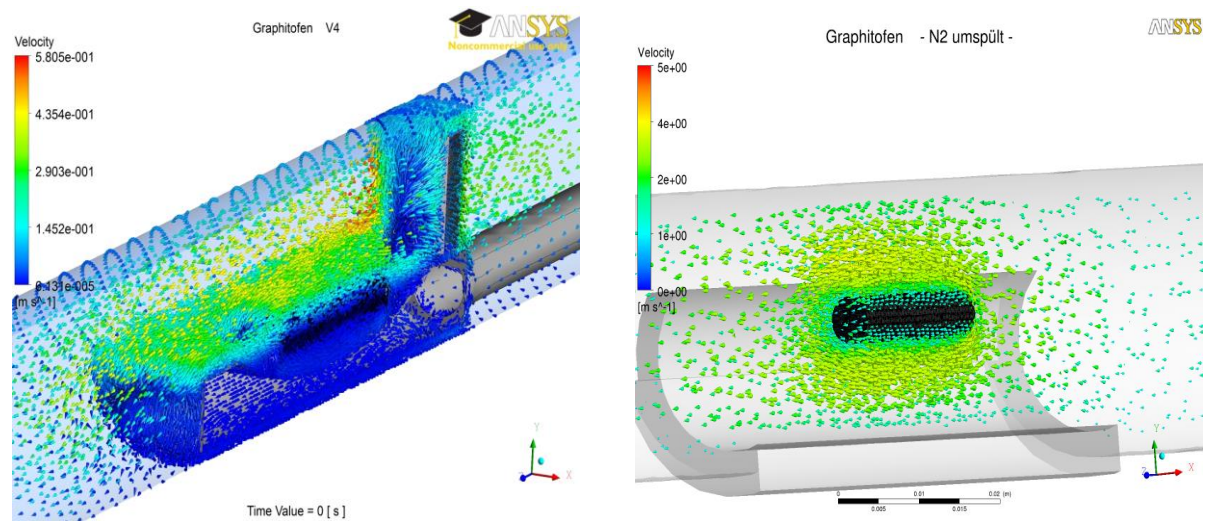


Figure 4.9.4: Flow patterns of the original and the new sample holder design

4.10 Electrolysis

FZJ: The experimental set-up for electrolysis (anodic oxidation) of neutron-irradiated nuclear graphite is shown in Figure 4.10.1. The equipment consists of a beaker with a platinum electrode acting as a cathode and a graphite electrode acting as an anode. The anode is constructed in such a way that graphite samples can be hooked therein. The anodic off-gases are collected in a reversed funnel and discharged via a lateral gas outlet tube. Subsequently, the off-gases were pneumatically collected into a test tube. The analysis of these gases was made by solvent extraction in sodium hydroxide and by following liquid scintillation counting. For the present experiments, 5% nitric acid was used as electrolyte. The electric current was adjusted to 0.5 A. The duration of all experiments was 2 h.

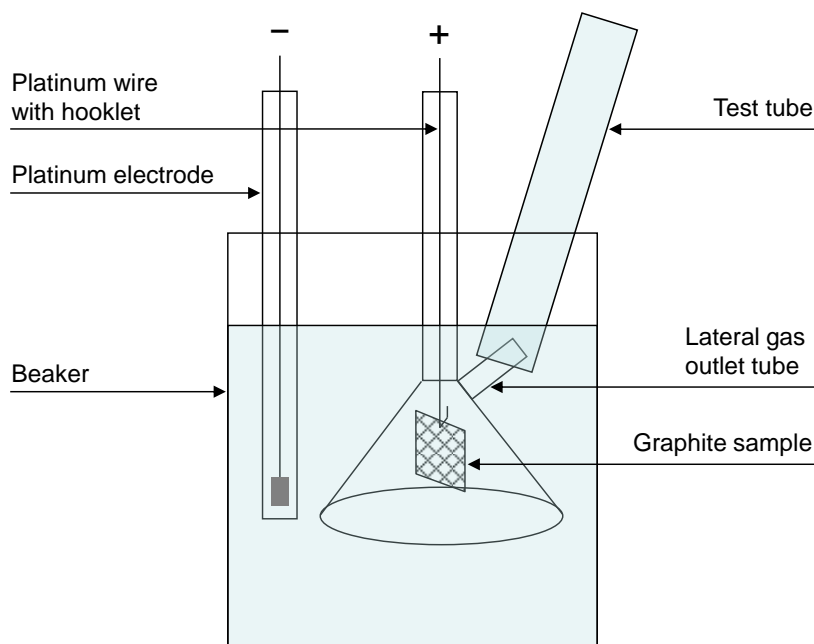


Figure 4.10.1: Experimental rig for anodic oxidation of graphite

4.11 Multichannel γ spectrometry

INR: Cobalt-60 was measured by multi-channel gamma spectrometry directly in the graphite samples, without pre-treatment, using an HPGc detector (35%) associated with a 4096 channels spectrometer.

For spectrometer calibration, in house source prepared from standard solution containing Am-241, Ba-139, Cs-137 and Co-60 was used.

Small quantities of sample (powder) were measured in glass LSC vials. The vials were placed directly on the detector in a fixed coaxial position. The calibration source was prepared by using 1 ml standard solution. Apparently, the source and samples had the same volume. No self-absorption correction was applied.

Results from gamma spectrometry are included in Table 4.11.1:

Table 4.11.1: Measurement of radionuclides by gamma spectrometry

Sample ID		Co-60		Nb-94		Cs-137		Eu-154		Eu-155		Am-241	
		Bq/g	\pm	Bq/g	\pm	Bq/g	\pm	Bq/g	\pm	Bq/g	\pm	Bq/g	\pm
G1	G1_1	1.9060E+04	5.98E+02	67.50	7.5	192.50	12.5	220.00	15.0	50.00	7.5	107.50	12.5
	G1_2	1.8417E+04	5.93E+02	85.37	7.5	197.56	15.0	229.27	17.5	48.78	7.5	95.12	12.5
	G1_3	1.8522E+04	5.95E+02	75.61	5.0	229.27	12.5	209.76	10.0	43.90	5.0	112.20	7.5

G2	G2_1	1.9435E+04	6.08E+02	75.00	2.5	222.50	10.0	220.00	5.0	42.50	2.5	105.00	5.0
	G2_2	1.8558E+04	5.80E+02	62.50	5.0	210.00	12.5	212.50	12.5	52.50	5.0	105.00	10.0
	G2_3	1.8178E+04	5.70E+02	65.00	5.0	205.00	12.5	230.00	10.0	45.00	5.0	102.50	10.0

Note: G1 and G2 are the 2 blind sub-samples received by INR to be used for analysis

Radionuclides distribution in the graphite brick

The samples' activity from central cylindrical piece of the cell is presented in Figure 4.11.1.

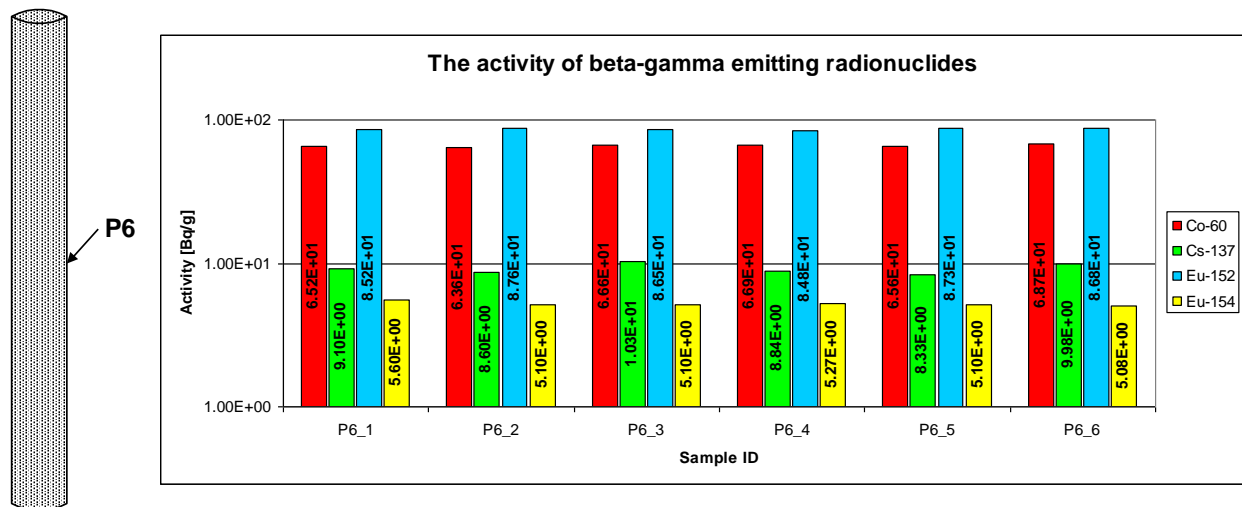


Figure 4.11.1: Activities of samples from central cylindrical piece of the cell

The samples' activity situated on the external surface of the upper part on the pipe piece is presented in Figure 4.11.2.

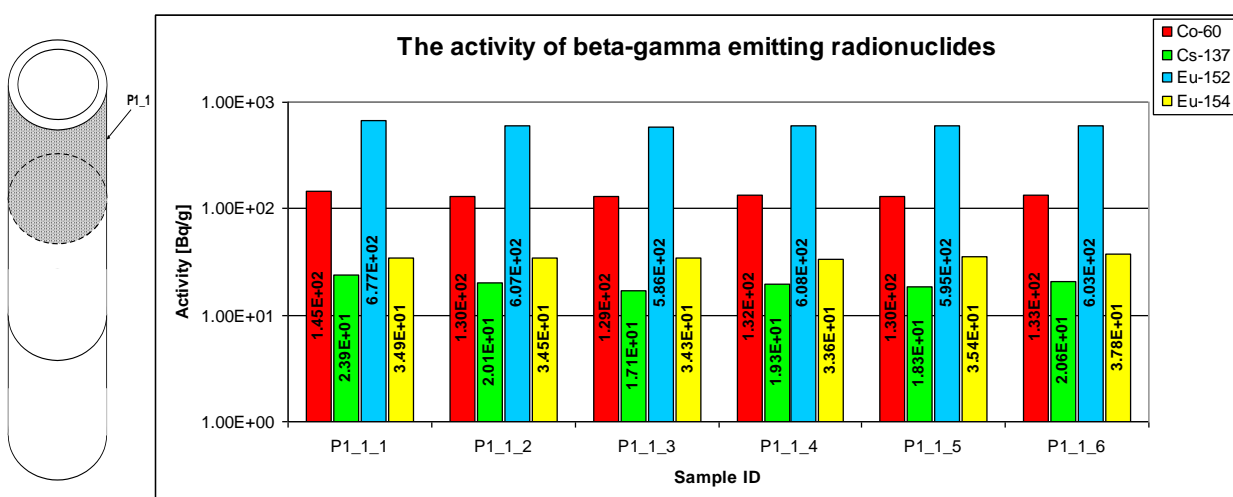


Figure 4.11.2: Activities of samples situated on the external surface of the upper part on the pipe piece

The samples' activity situated on the external surface of the middle part on the pipe piece is presented in Figure 4.11.3.

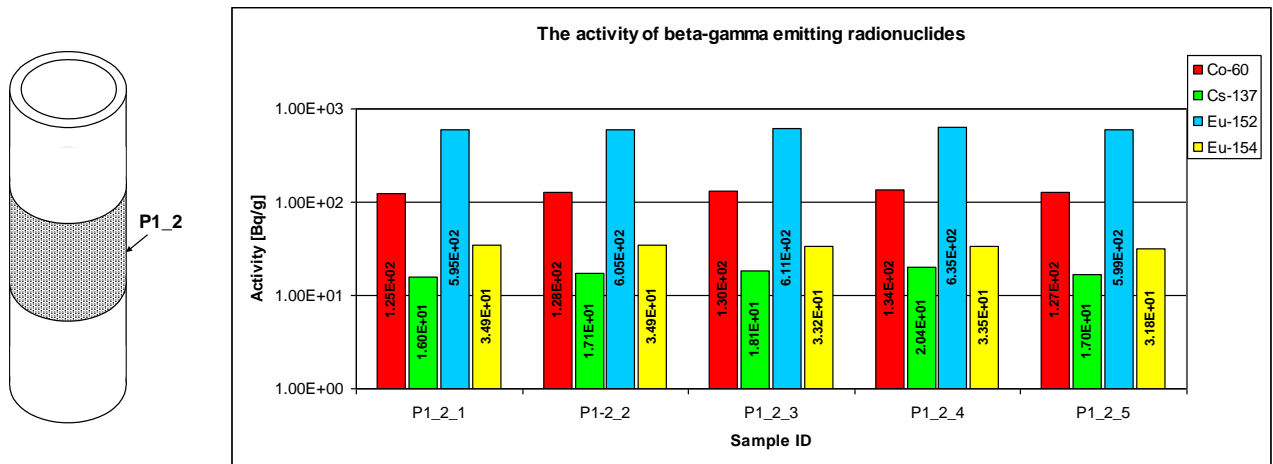


Figure 4.11.3: Activities of samples situated on the external surface of the middle part on the pipe piece

The samples' activity situated on the external surface of the bottom part on the pipe piece is presented in Figure 4.11.4.

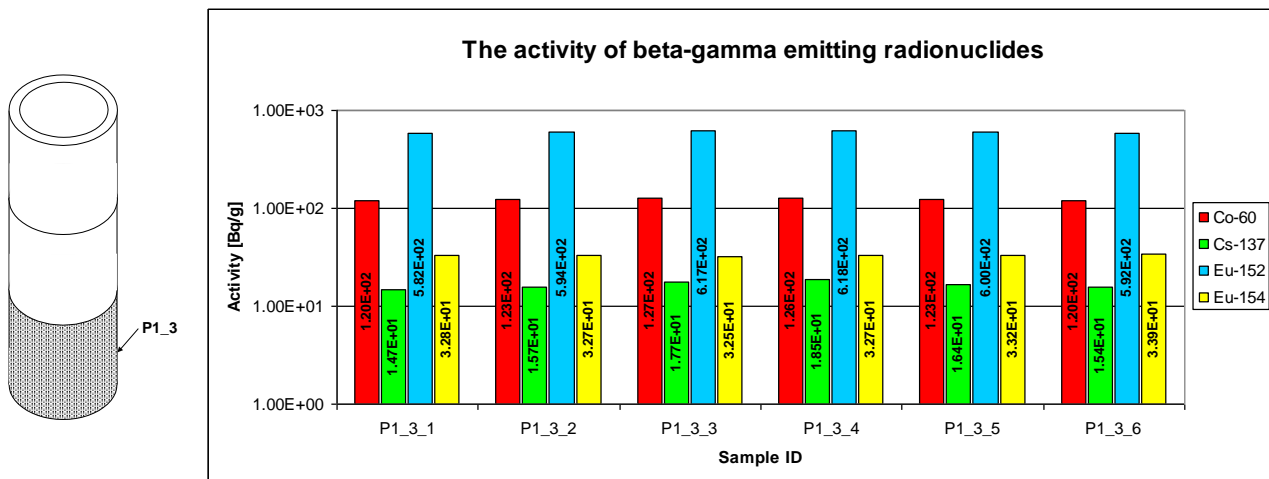


Figure 4.11.4: Activities of samples situated on the external surface of the bottom part on the pipe piece

The samples' activity situated on the cylindrical surface of the middle part of the piece located in one of the cell corners is presented in Figure 4.11.5.

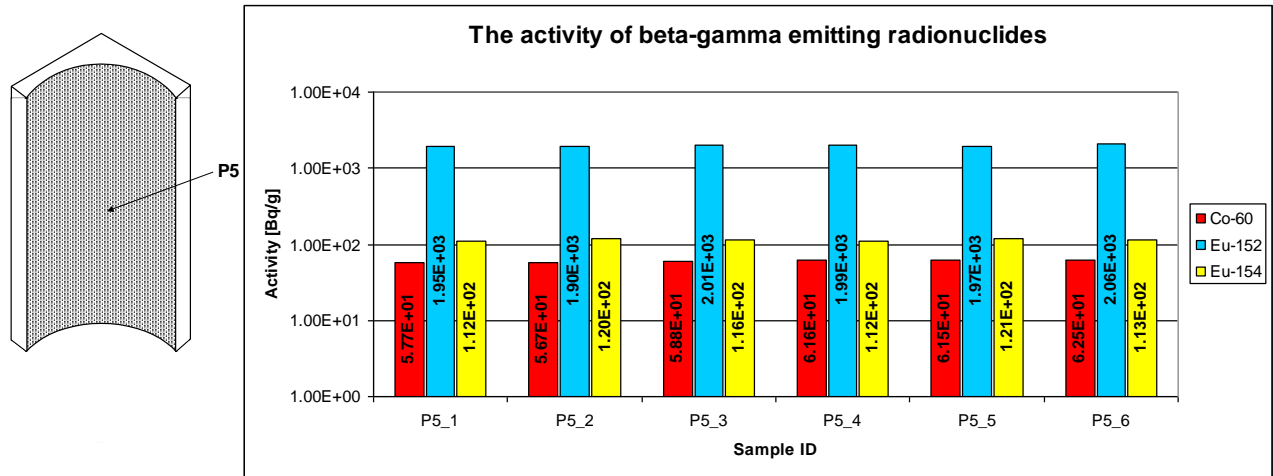


Figure 4.11.5: Activities of samples situated on the cylindrical surface of the middle part of the piece located in one of the cell corners

The samples' activity situated on the external surface of the upper part of the piece located in one of the cell corners is presented in Figure 4.11.6.

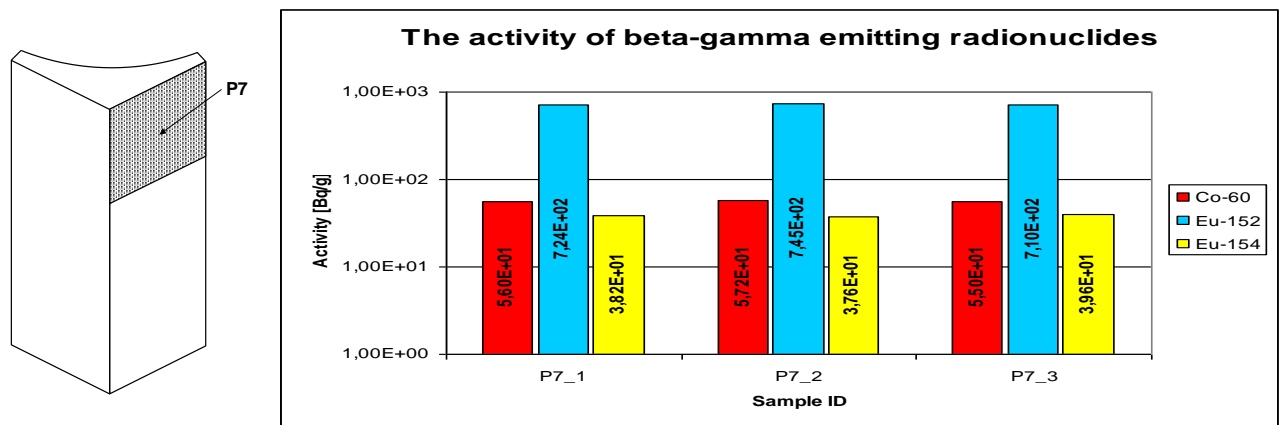


Figure 4.11.6: Activities of samples situated on the external surface of the upper part of the piece located in one of the cell corners

The samples' activity situated on the external surface of the bottom part of the piece located in one of the cell corners is presented in Figure 4.11.7.

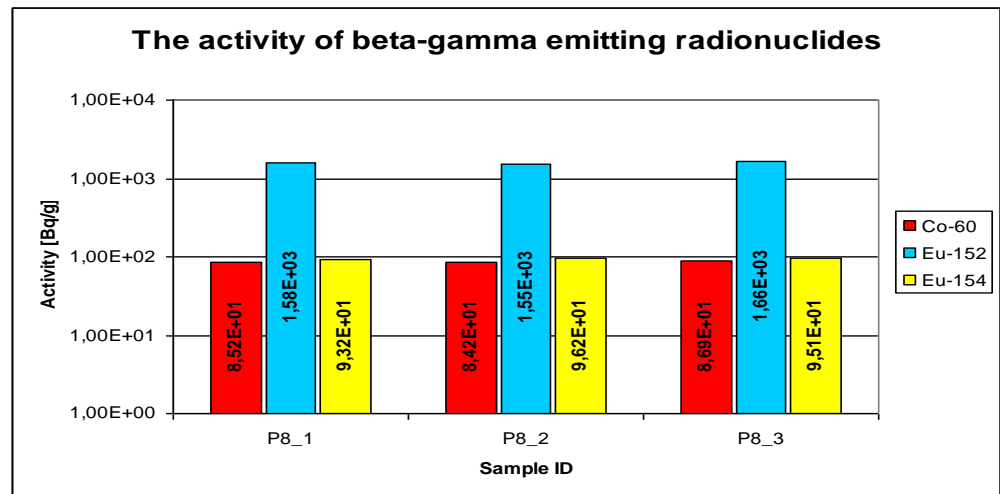
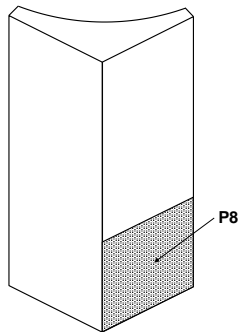


Figure 4.11.7: Activities of samples situated on the on the external surface of the bottom part of the piece located in one of the cell corners

The samples' activity situated on the external surface of the middle part on the piece located in one of the cell corners is presented in Figure 4.11.8.

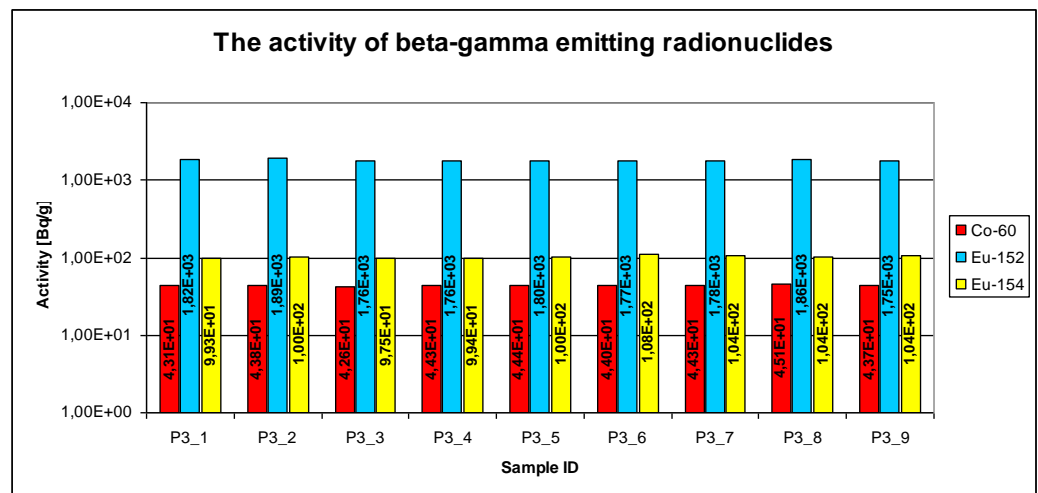
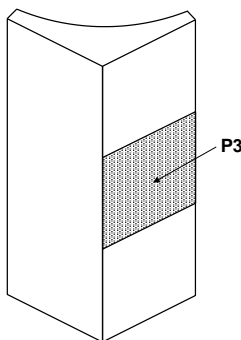


Figure 4.11.8: Activities of samples situated on the external surface of the middle part on the piece located in one of the cell corners

The samples' activity situated on the external surface of the middle part on the piece located in one of the cell corners (another face) is presented in Figure 4.11.9.

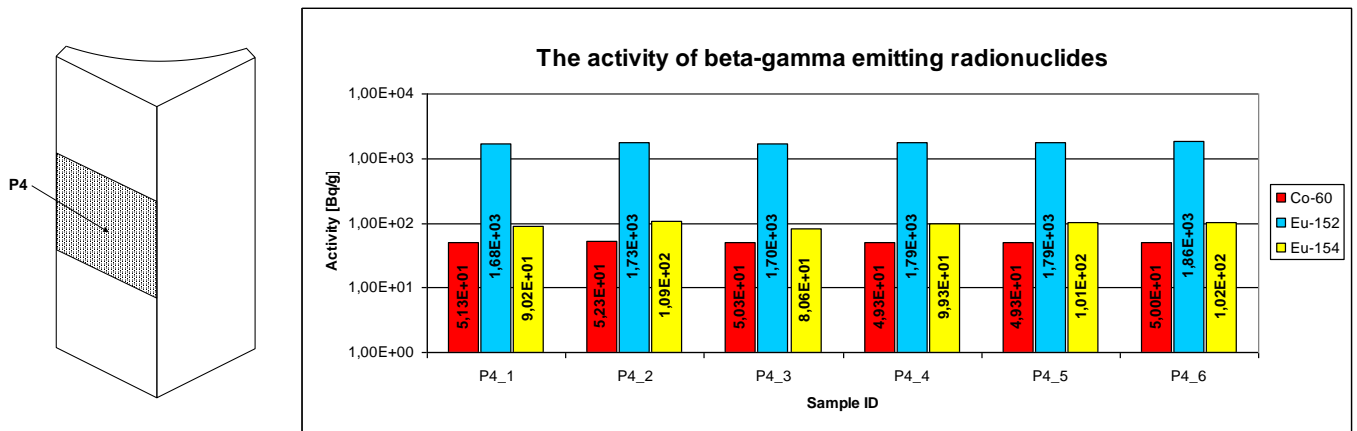


Figure 4.11.9: Activities of samples situated on the external surface of the middle part on the piece located in one of the cell corners (another face)

Variation of activity into the cell (from outside to the inside) is presented in Figure 4.11.10.

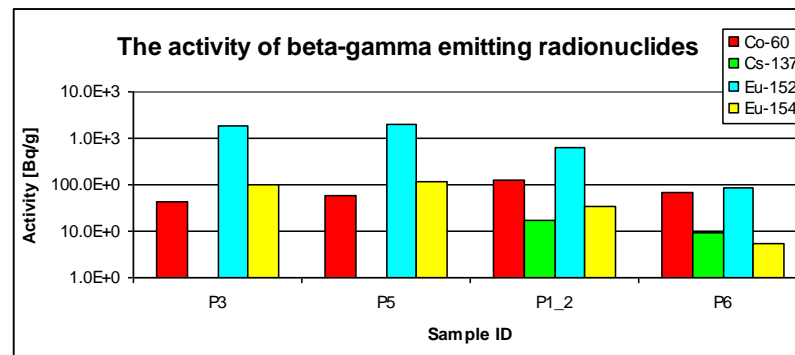


Figure 4.11.10: Variation of activity into the cell (from outside to the inside)

4.12 Liquid scintillation measurement

INR: H-3 and C-14 measurements were performed using the flame oxidation method as samples preparation technique and liquid scintillation for their analysis.

The irradiated graphite analyzed was sampled from 9 different locations of graphite block as shown in Figure 4.12.1.

- 1 from central cylindrical piece - P6;
- 3 from the external surface of pipe piece (upper, middle and bottom surface) - P1_1, P1_2, P1_3;

- 1 from cylindrical (inside) surface of the middle part of the piece located in one of the cell corner - P5
- 4 different locations from external surface of the piece located in one of the cell corner (upper, 2 x middle and bottom surface) - P7, P3, P8, P4.

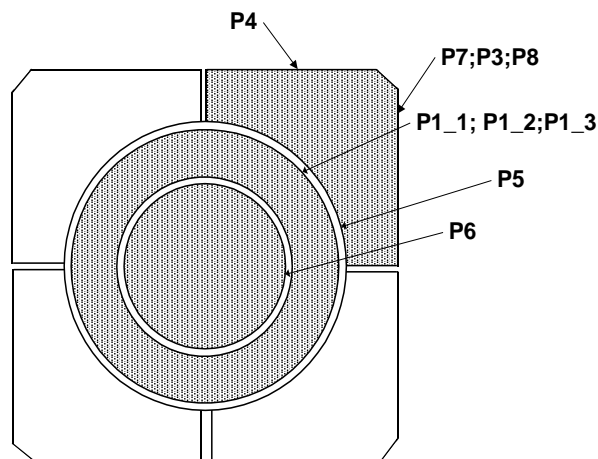


Figure 4.12.1: Sampling locations for radionuclide measurements

The model 307 PerkinElmer™ Sample Oxidizer was used for decomposition of graphite. The combustion system burns the sample in a continuous flow of oxygen. During the combustion process, the radionuclide components are separated as tritiated water (which is flushed down into the tritium counting vial with the tritium scintillator) and radioactive carbon dioxide (which is trapped into an adsorber as carbamate to be flushed into the ^{14}C counting vial using the ^{14}C scintillator, Permafluor E+ as a rinsing media, followed by counting of the vials in a 2100 Tri-Carb Packard model liquid scintillation analyzer using recommended ^{14}C counting conditions).

Prior to combustion of the graphite samples collected from TRIGA reactor, Sample Oxidizer performance specifications ($^3\text{H}/^{14}\text{C}$ recovery degree and $^3\text{H}/^{14}\text{C}$ retention degree in the circuits of combustion system) were evaluated.

Tritium and ^{14}C were determined by liquid scintillation counting using the model 2100 Tri-Carb® Packard Liquid Scintillation Analyzer.

The values measured show activities of H-3 in the range of $0.7\text{--}2 \cdot 10^4$ Bq/g, ten times larger than C-14. Table 4.12.1 summarizes these measurements, including also previous data on C-14 measured in 2009. Differences in C-14 activity arise from the number of samples used in the measurement (average of 3 sub-samples in 2009 compared to the measurement of the whole one sample in 2011).

Table 4.12.1: H-3 and C-14 measurements in different locations of a graphite block

Sample ID	Location in the graphite block	H-3 (Bq/g)	C-14 (Bq/g)	C-14 Measurements 2009 (Bq/g)
3	Corner, outside, upper part	$1.970 \cdot 10^4 \pm 98.5$	$1.084 \cdot 10^3 \pm 5.42$	$0.9928 \cdot 10^3 \pm 4.96$
7	Corner, outside, middle part	$0.813 \cdot 10^4 \pm 40.65$	$0.841 \cdot 10^3 \pm 4.20$	$0.8367 \cdot 10^3 \pm 4.18$
8	Corner, outside, bottom part	$1.470 \cdot 10^4 \pm 73.5$	$1.924 \cdot 10^3 \pm 9.62$	$1.7984 \cdot 10^3 \pm 8.99$
5	Corner, inside	$1.198 \cdot 10^4 \pm 59.9$	$0.962 \cdot 10^3 \pm 4.81$	$0.9127 \cdot 10^3 \pm 4.56$
6	Central cylinder	$0.695 \cdot 10^4 \pm 34.75$	$1.016 \cdot 10^3 \pm 5.08$	$0.9872 \cdot 10^3 \pm 4.94$

5. Locations and Chemical Bounds of Impurities and Radionuclides before Treatment

5.1 Structure of Nuclear Graphite, its Impurities and their Activation Products

Nuclear graphite is an artificially produced product manufactured from filler and binder materials [3]. For the graphite moderator mainly petroleum or pitch coke is used for the filler and, as a binder, mainly coal-tar-pitch. However, in the case of the fuel compact or pebble matrix a mixture of crushed artefacts and natural graphite bound in formaldehyde resin is used. These components retain their principal structures in the fabricated graphite despite been subject to high temperature baking and graphitising processes. The microstructure of carbon brick, which can be considered as an incompletely graphitised nuclear graphite, shows this very well. In Fig. 6, a large filler particle surrounded by semi-graphitised binder material can be seen.

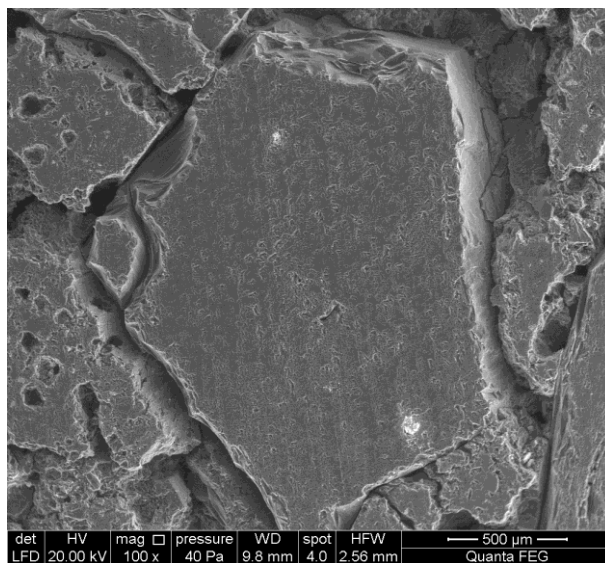


Fig. 6: Scanning electron micrograph of carbon brick

This binder material is where many of the impurities are located as it can be seen in Fig. 7. The white dots are impurities which can be detected by back-scattering electrons. These impurities mainly consist of oxides of aluminium, silicon and iron, but the easily neutron-activated elements such as cobalt and nickel are always affiliated to these main impurities.

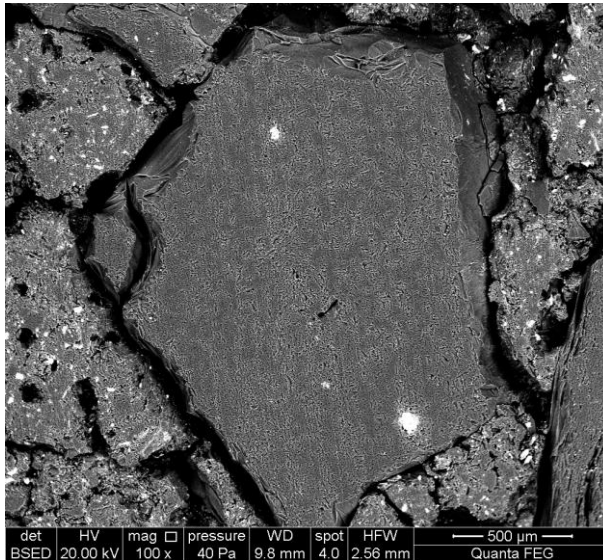


Fig. 7: Scanning electron micrograph of carbon brick in back-scattering electron mode

Another element for neutron activation in nuclear graphite is nitrogen. The isotope ^{14}N reacts with thermal neutrons to form ^{14}C with a cross section of 1.93 barn. Graphite has a high affinity to adsorb nitrogen on its surfaces. These surfaces are not only the outer surfaces, but also the inner surfaces of the pore system. The adsorption profile of nitrogen can be detected by secondary ion mass spectroscopy (SIMS). Fig. 8 shows the depth profiles of ^{14}N (detected as CN^-) in irradiated (a) and virgin (b) reflector graphite from the Jülich experimental high-temperature pebble-bed reactor (AVR). These profiles were recorded after conditioning of the samples in vacuum for 3 days to avoid erroneous signals due to atmospheric nitrogen. Despite of these conditions, the profiles show an increased amount of nitrogen towards the surface of the graphite samples. Quantum mechanical calculations demonstrate that nitrogen should be adsorbed on graphite surfaces not by physisorption but by chemisorption to form covalent bonds [4, 5].

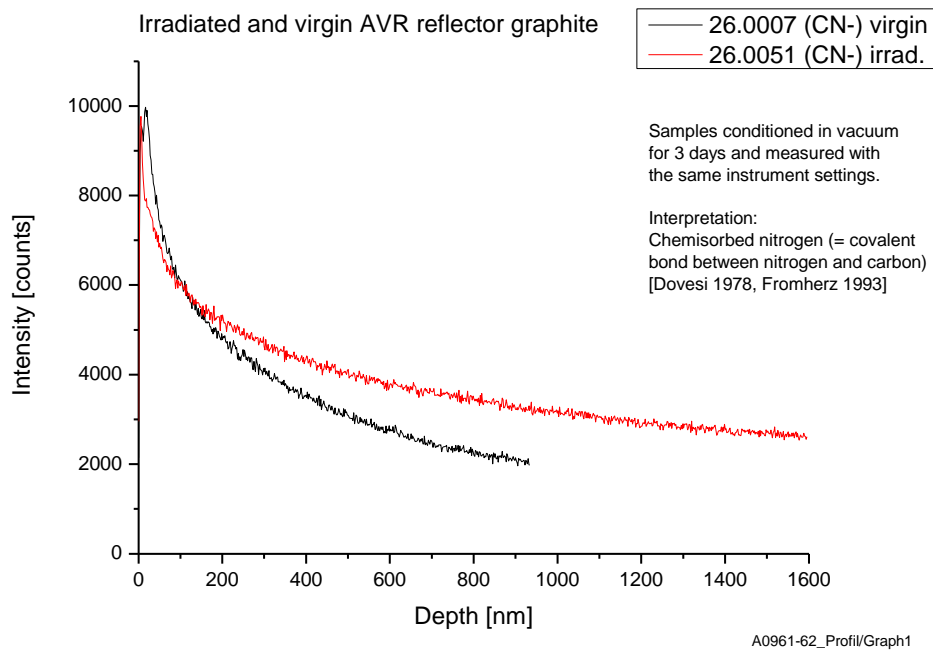


Fig. 8: Depth profiles of ^{14}N (detected as CN^-) in irradiated and virgin AVR reflector graphite

These covalent bonds between nitrogen and graphite are the reason for the relatively high amount of nitrogen in nuclear graphite (approx. 300 ppm). Under neutron irradiation, the nitrogen will be activated to form radiocarbon.

An important question is: Which is the location and the chemical bond of radiocarbon in neutron-irradiated nuclear graphite? The recoil energy of the ^{14}C atoms resulting from the n,p nuclear reaction is 41.4 keV. This energy is high enough to break any chemical bond. However, where are free binding sites for ^{14}C in graphite? Free binding sites are in vacancy structures on the surface of the graphite crystallites and micro-crystallites (see Fig. 9), between the graphite lattice planes (see Fig. 10) and, finally, on any carbon atom with free binding valences in disordered graphite structures or in amorphous carbon parts. Therefore, it can be postulated that ^{14}C is concentrated in neutron-irradiated nuclear graphite on surfaces, in near-surface structures and in disordered or amorphous parts of incompletely graphitised binder or filler materials.

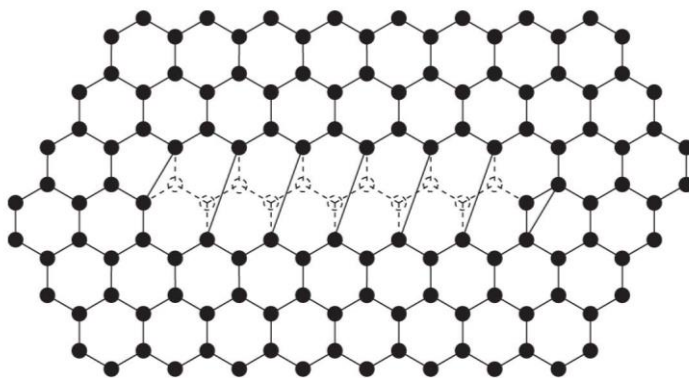


Fig. 9: Possible vacancy structures on graphite surfaces [6]

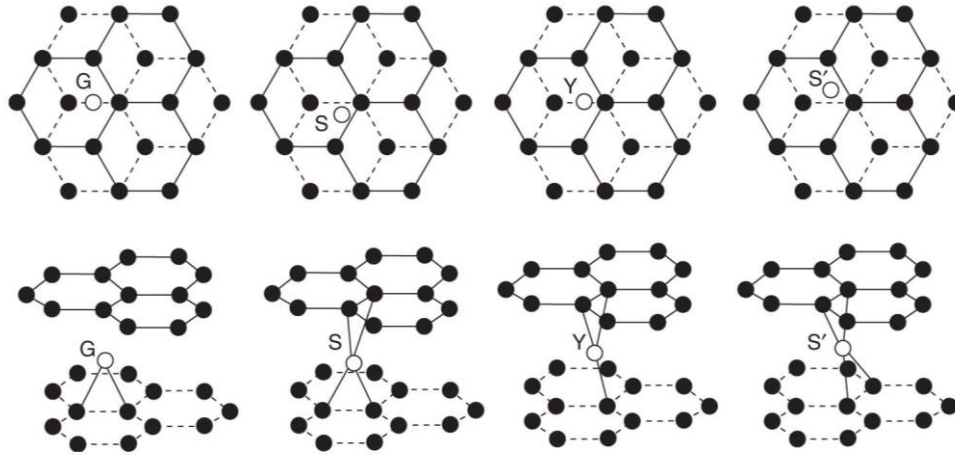


Fig. 10: Possible places of carbon atoms between the graphite lattice planes [6]

An important experimental finding is that the distribution of radionuclides in neutron-irradiated nuclear graphite is inhomogeneous. The starting point of the evolution to this knowledge is the observation that there are not two graphite samples of the same reactor and from the same position of this reactor which have exactly the same amount of a given radionuclide.

The inhomogeneous distribution of radionuclides in neutron-irradiated nuclear graphite is also proved by secondary ion mass spectrometry (SIMS): We measured a graphite sample from the reflector of the AVR high-temperature reactor with an averaged ^{14}C inventory of $3.3\text{E}+05 \text{ Bq/g}$ and we found a ^{14}C signal at 14.0039 u (see Fig. 11). Then we re-measured this graphite sample and we did not find this signal anymore (see Fig. 12). To validate our measurements, we measured a ^{14}C reference material (chemical form: graphite) with an activity of $3.7\text{E}+08 \text{ Bq/g}$ and we found a considerable signal at 14.0036 u (exact mass number of $^{14}\text{C} = 14.00324 \text{ u}$). With this signal, we calculated the related ^{14}C inventory of the AVR signal and obtained a value of $2.0\text{E}+07 \text{ Bq/g}$ which is 60 times higher than the averaged ^{14}C inventory! From this result we concluded that ^{14}C must be present in irradiated graphite (at least partly) as “hotspots”.

Another assumption may be drawn from the SIMS measurements. SIMS was the only method by which ^{14}C was “chemically” detected. In the mass spectra, ^{14}C appeared only as single carbon ion. Other ^{14}C fragments were not found. A direct conclusion from the SIMS measurements to the speciation of ^{14}C is not possible because SIMS shows only molecular fragments; but it could be postulated by analogy that ^{14}C could be bound in irradiated graphite in the same way like the $^{12/13}\text{C}$ atoms in any graphite because the main $^{12/13}\text{C}$ -containing fragment of any graphite obtained using SIMS is the single $^{12/13}\text{C}$ ion.

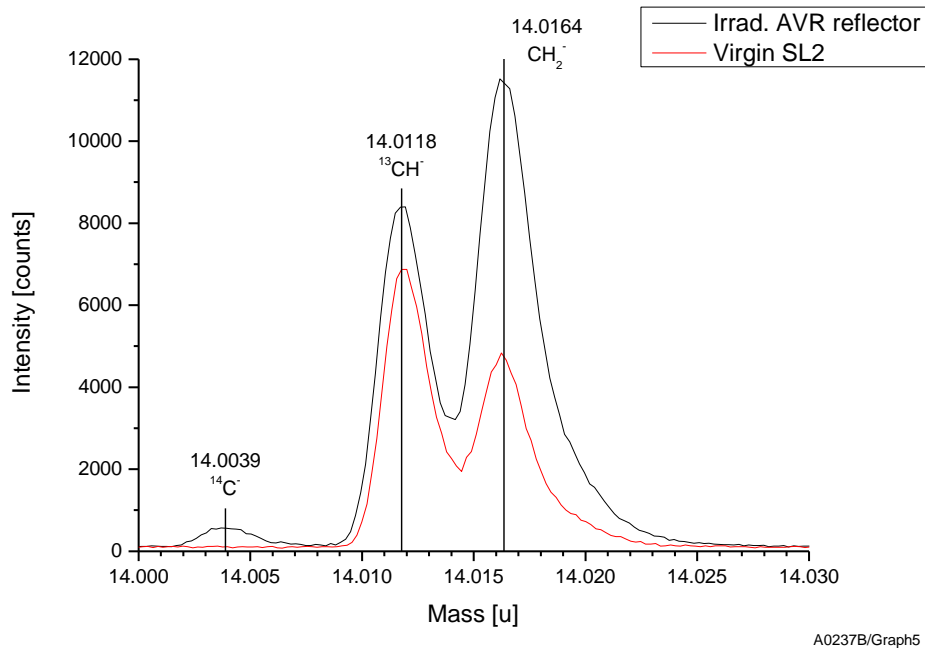


Fig. 11: Secondary ion mass spectra of irradiated AVR reflector graphite in comparison to virgin Saint-Laurent A2 graphite in the region of ^{14}C

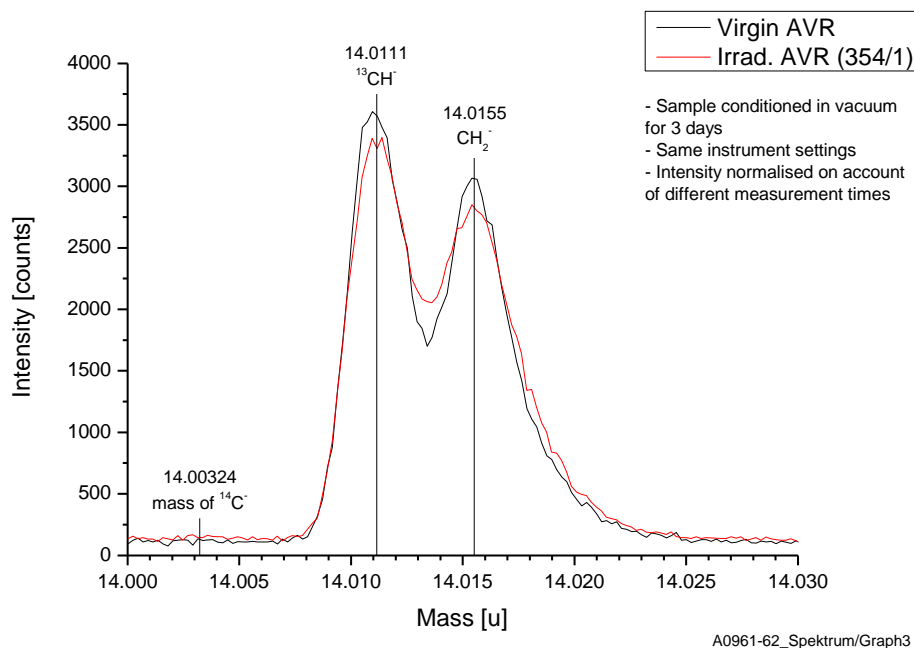


Fig. 12: Repeat secondary ion mass spectra of irradiated AVR reflector graphite (same sample as in Fig. 11) in comparison to virgin AVR reflector graphite in the region of ^{14}C

The mass spectrometric detection of other radionuclides than ^{14}C is difficult because their concentrations are much less than that of ^{14}C . By evaluation of the spectra of Fig. 11, it was found

a weak peak at the exact mass number of ^3H , 3.01605 u (see Fig. 13). Other ^3H peaks were not found. An assignment of this peak to defined structural elements is also difficult because this peak may come from several structural elements such as adsorbed HTO or C–T and C–OT groups. Nevertheless, the following assumption may be made: If ^3H is detectable at all, then it must come from a hotspot similar to ^{14}C . An important indication is the inhomogeneous distribution of inactive hydrogen fragments in the mass spectrum of all types of graphite (virgin and irradiated) as shown in Fig. 14. Also ^6Li , one of the precursors of ^3H , is inhomogeneously distributed. Therefore, it can be assumed that at least one part of ^3H in neutron-irradiated graphite is located in the vicinity of ^6Li . It is probable that this ^3H has formed compounds with the surrounding carbon atoms so that it is now present as C–T compound.

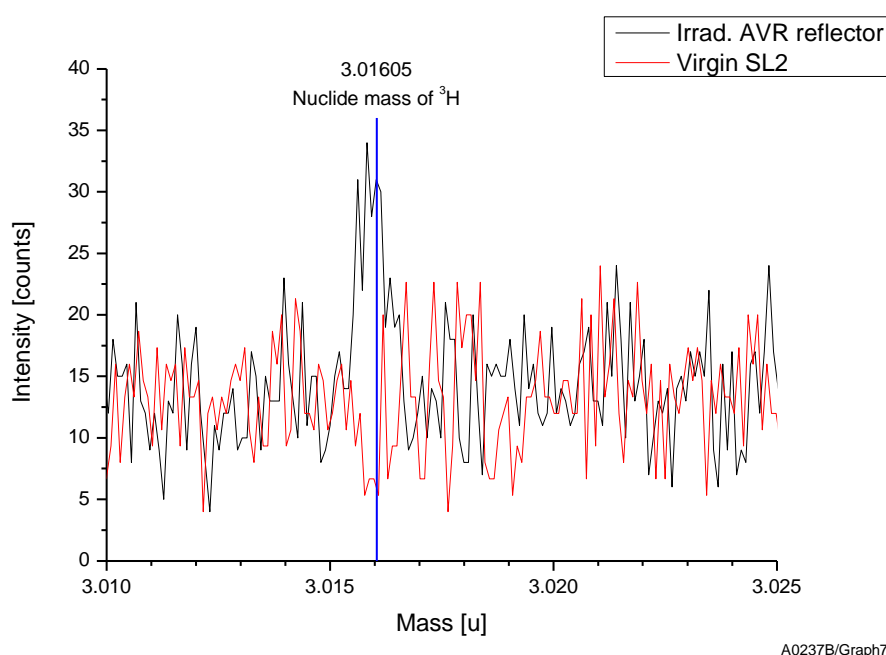


Fig. 13: Secondary ion mass spectra of irradiated AVR reflector graphite in comparison to virgin Saint-Laurent A2 graphite in the region of ^3H (same spectra as in Fig. 11)

As already indicated, SIMS offers the possibility to determine the spatial distribution of ions. Interesting ions in the negatively charged ion spectrum are H^- , CH^- , O^- , OH^- , CN^- and Cl^- . All these ions are distributed in a very inhomogeneous way and in part very clearly as hotspots, as it can be seen in Fig. 14.

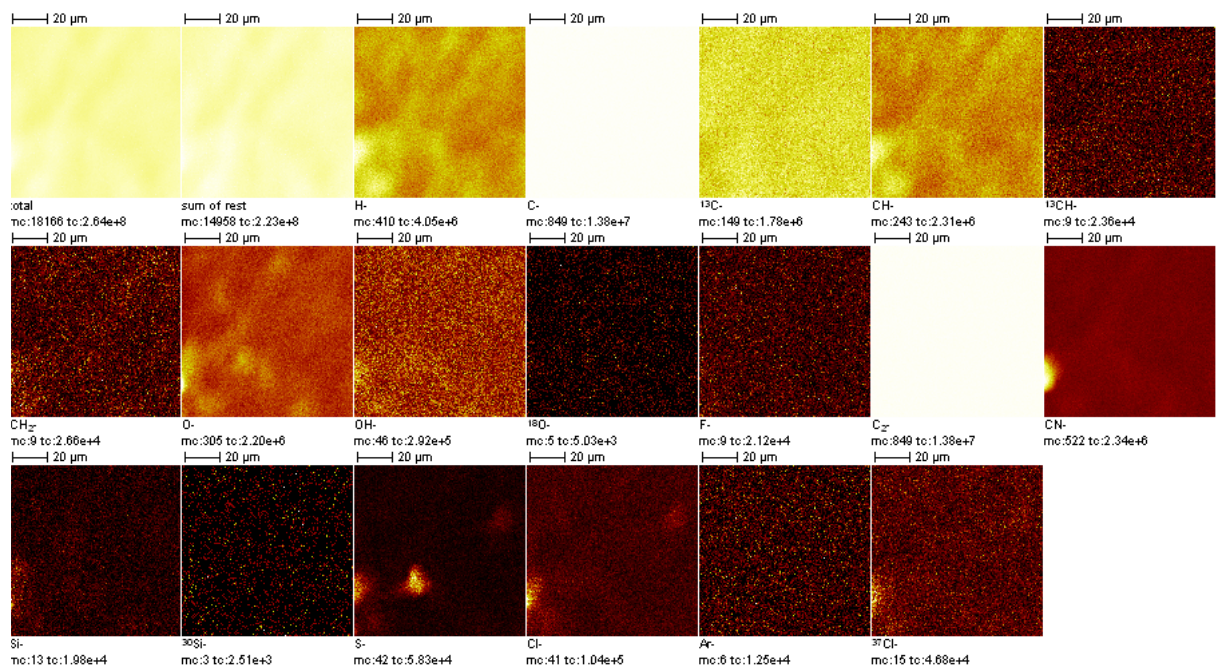


Fig. 14: Spatial distribution of negatively charged ions (sample: irradiated Saint-Laurent A2 graphite from the position 5120)

This finding is mainly important for the CN^- fragment because ^{14}N (natural amount: 99.64%) is activated to ^{14}C by neutron irradiation in a nuclear reactor. In spite of the relatively high recoil energy of 41.4 keV, ^{14}C will remain in the vicinity of its precursor. This is shown by molecular dynamic simulations of the transport behaviour of ^{14}C in irradiated nuclear graphite [7]. As can be seen in Fig. 15, the ^{14}C atom loses its kinetic energy in a perfect graphite lattice structure after a displacement distance of nearly 600 Ångström (60 nm). Therefore, ^{14}C will be concentrated in this region. After the detection of ^{14}N on graphite surfaces (see Fig. 8) and the corresponding conclusion for the presence of ^{14}C , the present detection of ^{14}N as hotspot is the second mode of existence of ^{14}C in neutron-irradiated graphite.

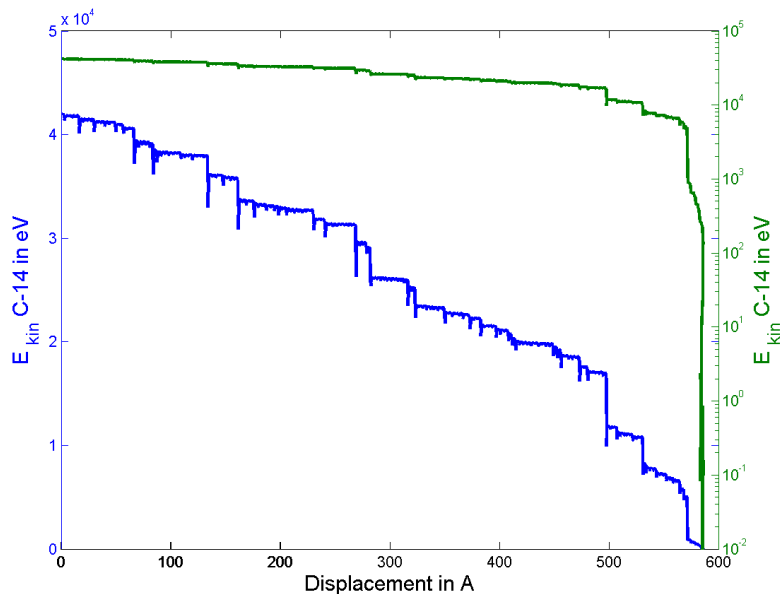


Fig. 15: Displacement and energy loss of a ^{14}C atom in a perfect graphite lattice structure [7]

Also metal ions like Na^+ , Mg^+ , K^+ , Ca^+ , Fe^+ etc. appear very clearly in the positively charged ion spectrum as hotspots, as can be seen in Fig. 16. Similarly, the easily neutron-activated isotopes $^6\text{Li}^+$, $^{10}\text{B}^+$ and $^{59}\text{Co}^+$ appear also in regions of higher concentration, although very weak due to their low total concentrations. It can be concluded that radionuclides formed from these isotopes (e.g. ^3H , ^{41}Ca , ^{55}Fe , ^{60}Co) will also remain in their local environment. This means that these radionuclides appear as hotspots or regions of higher concentration. A proof of this is given by digital autoradiography. In Fig. 17 the autoradiography image of the same sample is shown which has been used already for the SIMS measurements. The black dots which are caused by accumulation of beta-emitters are clearly visible. A surface contamination can be excluded because the measured surface was artificially generated by sawing the specimen from a larger sample.

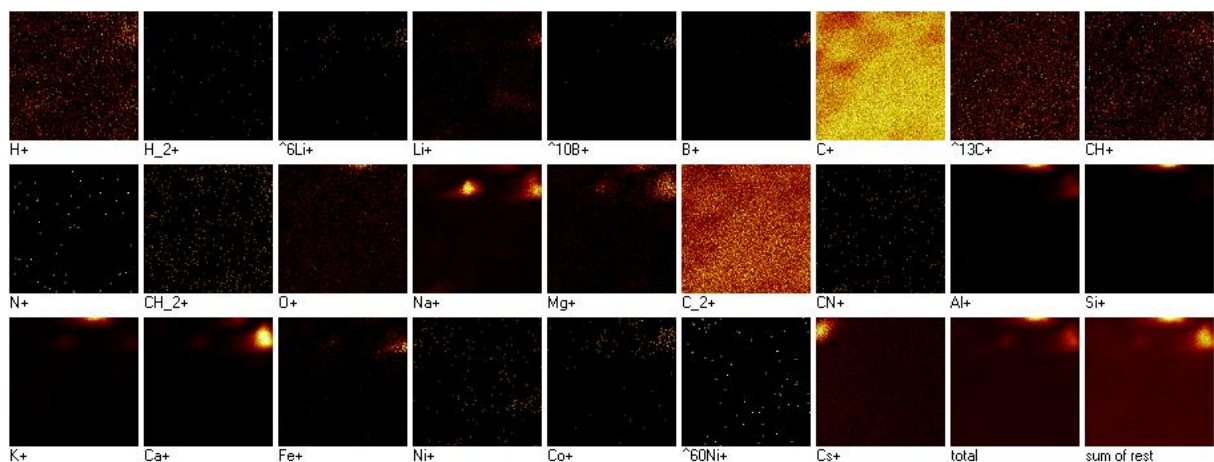


Fig. 16: Spatial distribution of positively charged ions (sample: irradiated Saint-Laurent A2 graphite from the position 5120)

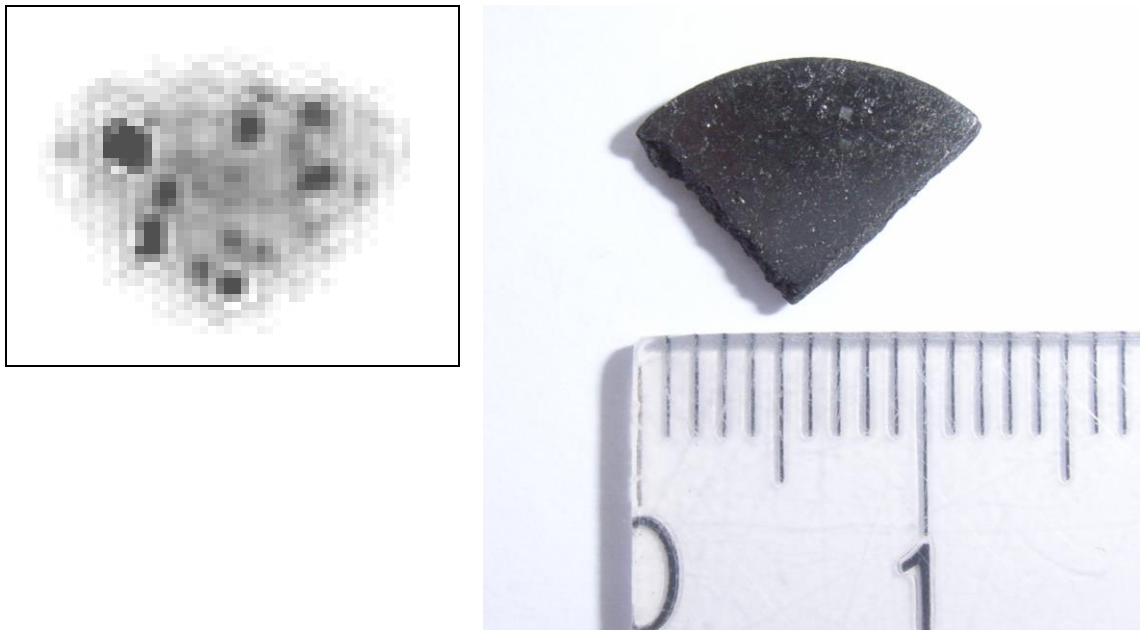


Fig. 17: Spatial distribution of beta-emitters determined by digital autoradiography (sample: irradiated Saint-Laurent A2 graphite from the position 5120; specimen diameter: 12 mm, thickness: 3 mm, mass: 0.2196 g)

5.2 Thermal Treatment

Another possibility to study the binding relations of radionuclides in neutron-irradiated nuclear graphite is thermal treatment in inert gases. The use of inert gases inhibits the oxidation of the graphite matrix. Only pyrolysis processes or reactions of adsorbed gases can occur. In Fig. 18 the release of tritium in inert gases at different temperatures is shown. Massive graphite samples from the thermal column of the Jülich Material Test Reactor “Merlin” were used (trepanned plug specimens; diameter: 8 mm, length: 37...50 mm, mass: 3...4 g). One can see that the release of tritium depends on the temperature. At 1300 °C, 93.6% of the tritium inventory of the graphite sample is removed within 10 hours, whereas the mass loss of the graphite matrix was negligible (< 1%).

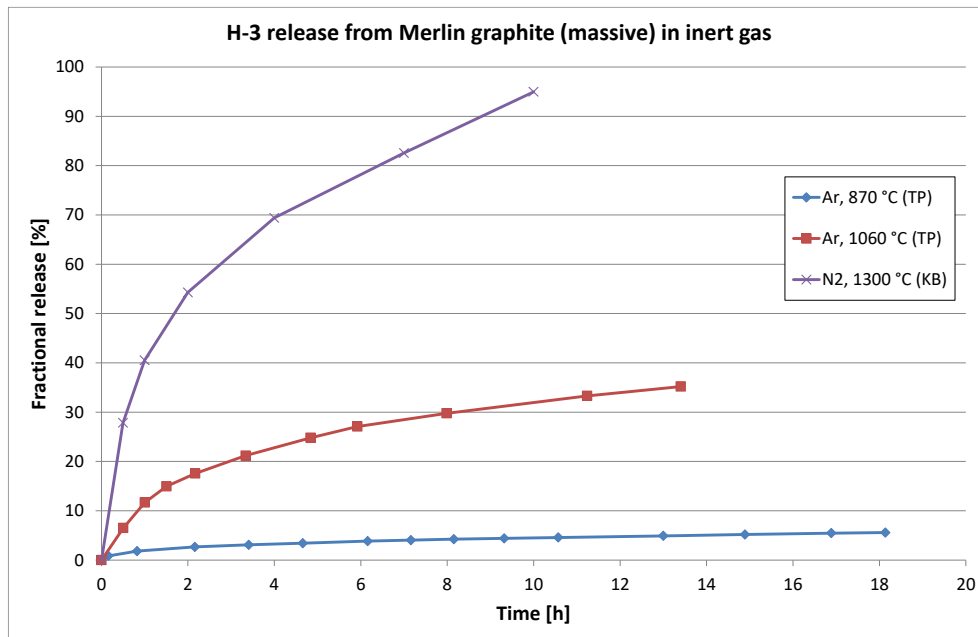


Fig. 18: Release of tritium in inert gases at different temperatures

The mechanism of the release of tritium from graphite does not seem to be simple. The release kinetics corresponds best to a diffusion reaction. A first order or a second order reaction is not applicable. But also the graph for a diffusion reaction (fractional release vs. square root time) is not linear, as can be seen in Fig. 19 and 20. It is reasonable that diffusion is not the only reaction which leads to a tritium release. As tritium must be bound within the graphite matrix in a certain mode, additional energy is necessary to remove it from its binding places. Such additional reactions could be: desorption of tritiated water (HTO) and pyrolysis of tritiated hydrocarbons (C—T or C—OT). An indication that there are two different reactions is given by the observed inversion of the release ratios of HT and HTO: at 866 °C the release of HTO is predominant whereas at 1063 °C the release of HT is predominant. This behaviour is comprehensible by consideration that at lower temperatures more HTO is released because desorption requires less energy and that at higher temperatures more HT is released because pyrolysis requires more energy.

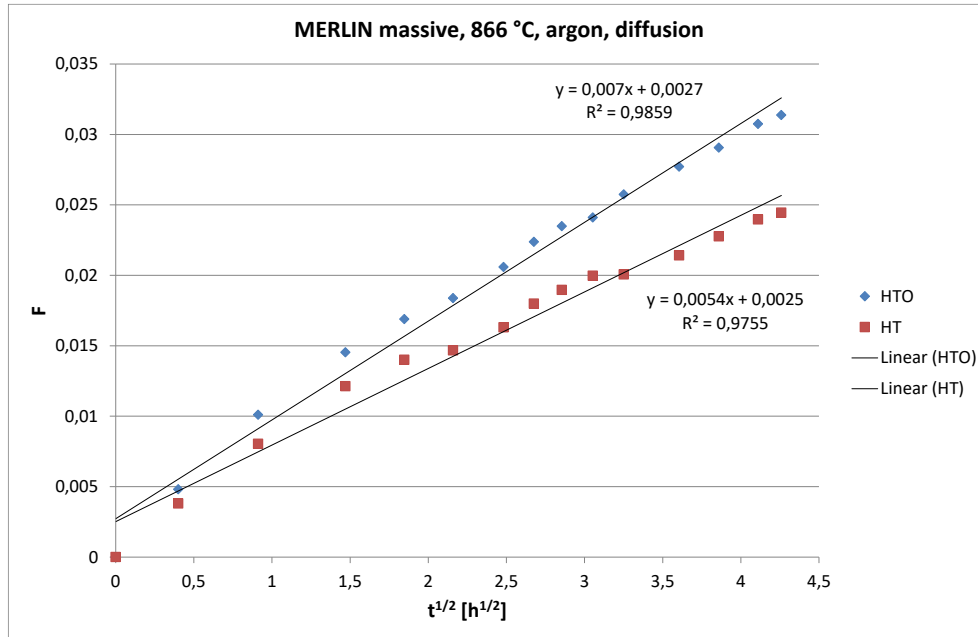


Fig. 19: Release of tritium in argon at 866 °C plotted as diffusion reaction

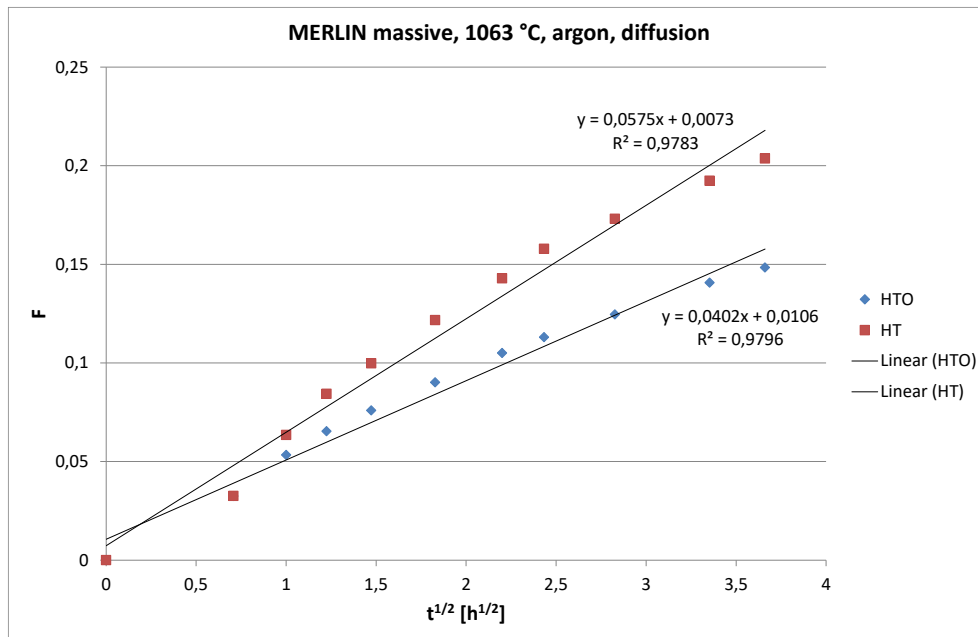


Fig. 20: Release of tritium in argon at 1063 °C plotted as diffusion reaction

The data from Fig. 19 and 20 can be used to estimate the activation energy for the apparent diffusion reaction (diffusion plus desorption or pyrolysis). Diffusion is described by the following equation:

$$\frac{\partial c}{\partial t} = D \Delta c \quad (1)$$

where D is the diffusion coefficient. The solution of the differential equation presuming spherical pore geometry results in

$$F = \sqrt{\frac{36D't}{\pi}} \quad (2)$$

where F is the fractional release of the diffusing material and D' the reduced diffusion coefficient ($D' = D/R^2$, R = diffusion radius). The reduced diffusion coefficient is controlled by temperature according to

$$D' = D'_0 \cdot e^{-\frac{E_D}{k_B T}} \quad (3)$$

where E_D is the activation energy for diffusion and k_B the Boltzmann constant. Determining the reduced diffusion coefficient for two temperatures, the activation energy can be calculated by

$$E_D = k_B \cdot \frac{T_1 \cdot T_2}{T_2 - T_1} \cdot \ln\left(\frac{D'_2}{D'_1}\right) \quad (4)$$

The tritium releases in Fig. 19 and 20 are divided in the chemical forms HT and HTO. Therefore, activation energies can be calculated for the release of HT and HTO. The apparent activation energy for the release of tritium as HT amounts to 3.15 eV and as HTO to 2.33 eV. The average amounts to 2.74 eV. This value is in good agreement with Fischer et al. [8] which have found 2.78 eV. The difference between HT and HTO can be explained by different desorption/formation energies of these diffusing species: HTO is maybe only adsorbed on the surface of the graphite particles whereas HT must be formed by pyrolysis. Desorption energies are less than pyrolysis energies.

The release of radiocarbon in inert gas (without ingress of air) seems to be also a temperature-dependent diffusion process in which radiocarbon is released as ^{14}CO and $^{14}\text{CO}_2$ formed by oxidation of radiocarbon in the pore system (see Fig. 21). This process is often overlain by a radiocarbon release caused by simple corrosion of the outer layers of the graphite matrix. This happens if the inert gas contains traces of oxidising gases (e.g. oxygen) due to small leakages of the used furnace (e.g. thermal permeability of the oven tube).

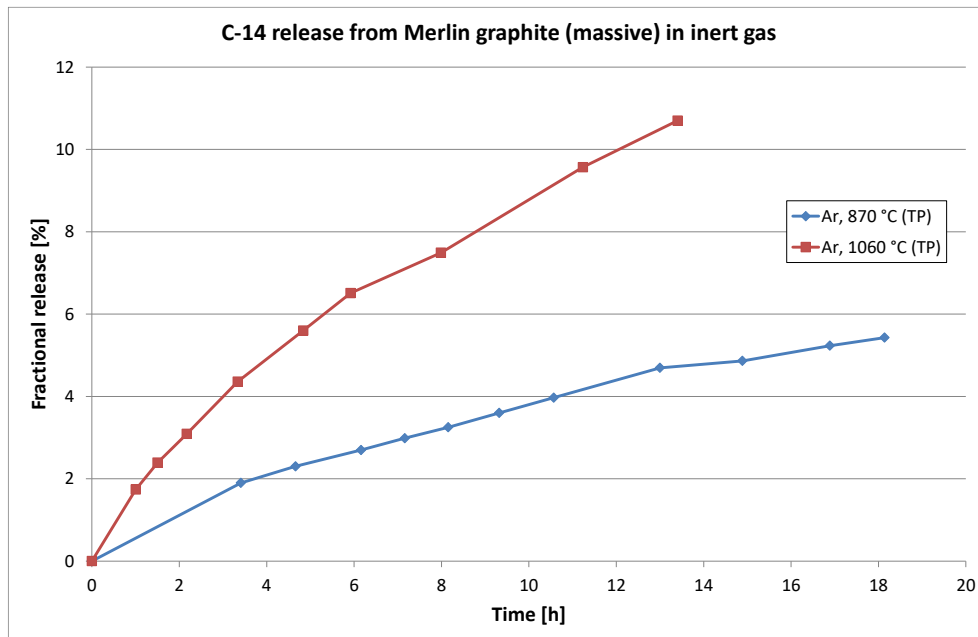


Fig. 21: Release of radiocarbon in inert gas at different temperatures

The release of radiocarbon in inert gas is also dependent on the amount of adsorbed oxidising gases. Simple addition of oxidising gases increases the release of radiocarbon but increases also the corrosion of the graphite matrix. An interesting modification of this experiment is a step-by-step process performed by reloading of the graphite sample surface with atmospheric oxygen and repeated thermal treatment, as can be seen in Fig. 22 [9]. The experiment shows the influence of adsorbed oxygen on the release of radiocarbon.

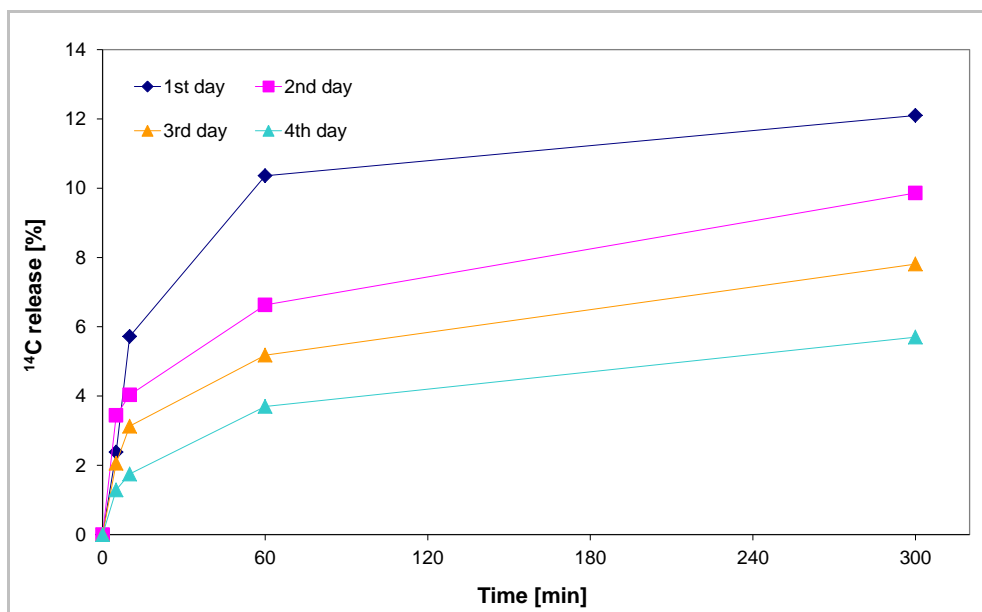


Fig. 22: Repeated thermal treatment at 900 °C under nitrogen atmosphere after intermediate exposure of the sample to air at room temperature for 20 hours (accumulated ^{14}C release: 35.5%, accumulated release of total carbon: 2.7%, ^{14}C enrichment in the gas phase: 13:1) [9]

The kinetic description of the thermal release of radiocarbon from graphite is derived from two kinds of experiments:

- “Real” inert gas experiments (as shown in Fig. 21) and
- Experiments in which the treatment gas contained a defined (small) amount of oxygen.

Real inert gas experiments give the chance to study the diffusion of radiocarbon through the graphite matrix. The graphical test for a diffusion reaction is a plot of the fractional release of radiocarbon vs. the square root of time. This is shown in Fig. 23. Application of Eq. 1–4 results in an apparent activation energy of 1.17 eV.

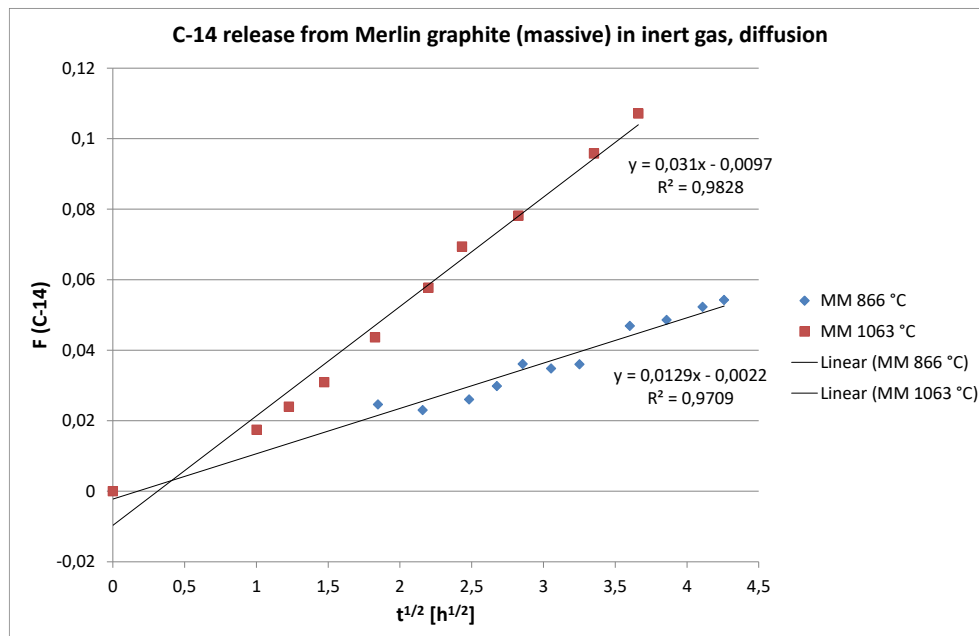


Fig. 23: Release of radiocarbon in inert gas at different temperatures from Fig. 21 plotted as diffusion reaction

The results of the experiments in which the treatment gas contained a defined amount of oxygen are given in Fig. 24. MERLIN graphite was treated with nitrogen which contained 1% oxygen. Two different temperatures were applied: 700 °C and 900 °C.

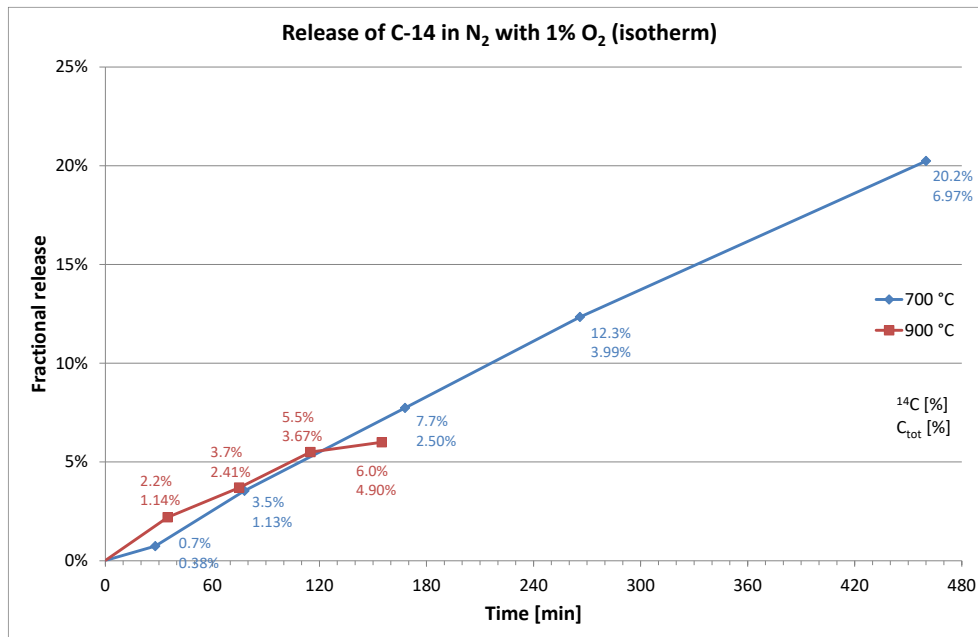


Fig. 24: Release of radiocarbon in nitrogen with 1% oxygen at different temperatures (the upper number gives the % ¹⁴C released and the lower number the % carbon consumed)

One can see that the release isotherms are quite linear up to a certain point at which the removable part of radiocarbon is consumed, and that they lie upon each other. This means in kinetic terms that the reaction between radiocarbon and oxygen is of zero order (independent on the concentration of radiocarbon and oxygen) and that the reaction rate is independent on the temperature.

The thermal release of radiocarbon is always coupled with an oxidation of the graphite matrix. To obtain more information about the release mechanism and the release kinetics of radiocarbon, it is necessary to study the oxidation behaviour of the graphite matrix. In Fig. 25 the release of total carbon (all carbon isotopes of graphite) for the above-mentioned experiments with MERLIN graphite is shown. One can see that the reaction mechanism is of zero order again, but there is also – as expected – a temperature dependence of the reaction rate: the higher the temperature the higher the reaction rate.

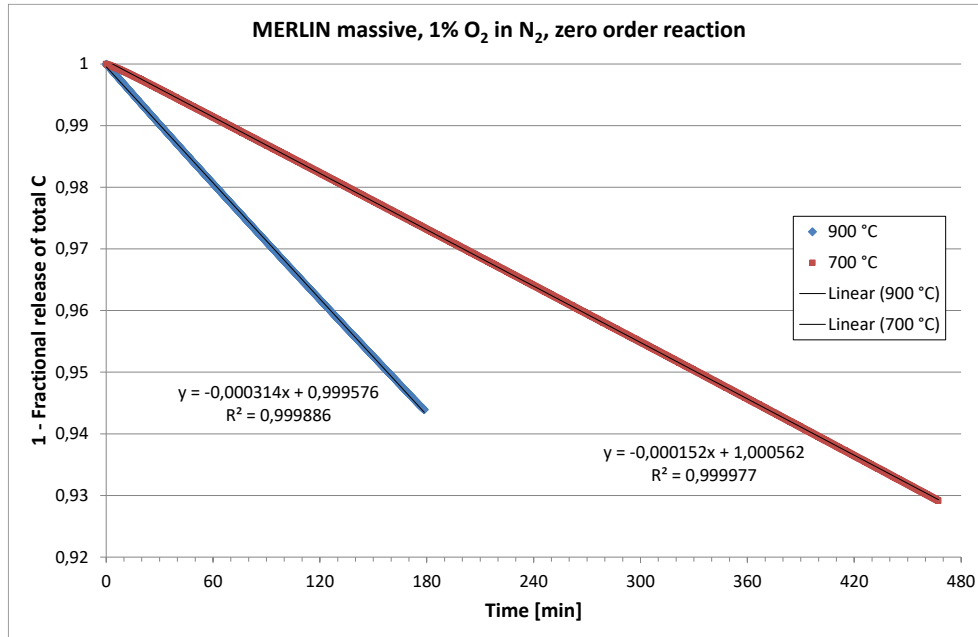


Fig. 25: Release of total carbon in nitrogen with 1% oxygen at different temperatures

With the temperature dependence, the activation energy for the oxidation of the graphite matrix can be calculated. The reaction rate of a zero order reaction is defined by

$$c(A) = -k \cdot t + c_0(A) \quad (5)$$

A plot of the concentration of the starting material (= 1 – fractional release of total carbon) vs. time should give a straight line with a slope of $-k$ (= reaction rate constant). From the known dependence of the reaction rate constant on the temperature (Arrhenius equation), the activation energy E_A can be calculated:

$$E_A = R \cdot \frac{T_1 \cdot T_2}{T_2 - T_1} \cdot \ln\left(\frac{k_2}{k_1}\right) \quad (6)$$

With Eq. 6, we obtain an activation energy of 34.4 kJ/mol (= 0.36 eV). With this result we can obtain the true activation energy for the diffusion of radiocarbon through the graphite matrix which is a simple subtraction of the activation energy for the oxidation of the graphite matrix from the apparent diffusion activation energy:

$$1.17 \text{ eV} - 0.36 \text{ eV} = 0.81 \text{ eV} \quad (7)$$

How we can interpret these kinetic results? First of all, we have to remind that the oxidation of nuclear graphite is not a simple process where oxygen reacts with homogeneous carbon. Due to the porous structure of nuclear graphite, there are three oxidation mechanisms [10]:

- Uniform oxidation inside the porous material (chemical regime, $< 500\text{ }^{\circ}\text{C}$)
- Location-dependent oxidation inside the porous material (in-pore diffusion controlled regime, $500\text{...}900\text{ }^{\circ}\text{C}$)
- Surface oxidation (boundary layer controlled regime, $> 900\text{ }^{\circ}\text{C}$)

That means: At low temperatures, the oxidation occurs on the surfaces of the whole pore system (inner surfaces), but it is very slow. At high temperatures, the oxidation occurs on the outer surfaces of the graphite sample, and it is very fast. Between both temperature ranges, there is a transitional range ($500\text{...}900\text{ }^{\circ}\text{C}$). The selective thermal release of radiocarbon from nuclear graphite (without complete incineration of the graphite matrix) occurs in this transitional range. This means that the release of radiocarbon occurs from the surfaces of the pore system. If there is an enrichment of radiocarbon in the off-gas, it can be assumed that radiocarbon is enriched on the surfaces of the pore system. Therefore, the selective thermal release of radiocarbon from nuclear graphite is a local effect and not a kinetic effect. This is why a temperature increase does not increase the amount of released radiocarbon without increasing incineration of the graphite matrix.

To visualise this process, it is advantageous to plot the fractional release of radiocarbon vs. the fractional release of total carbon for each temperature. This is shown for MERLIN graphite in Fig. 26. It can be seen that the enrichment factor of radiocarbon in the off-gas is higher at $700\text{ }^{\circ}\text{C}$ than at $900\text{ }^{\circ}\text{C}$. At $900\text{ }^{\circ}\text{C}$, the enrichment factor is nearly 1 which indicates that the release of radiocarbon occurs by simple incineration of the graphite matrix.

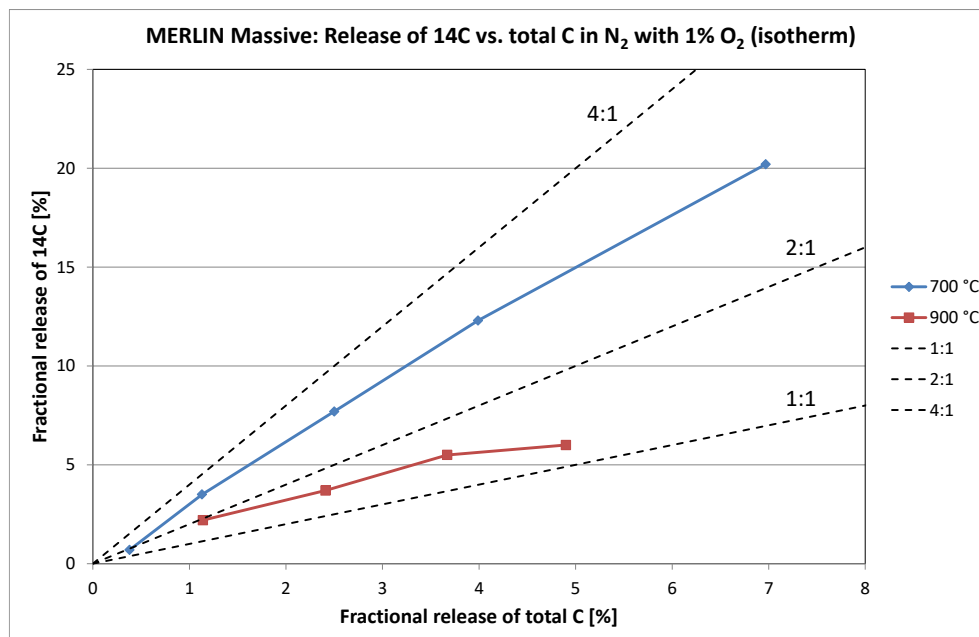


Fig. 26: Fractional release of radiocarbon vs. fractional release of total carbon in nitrogen with 1% oxygen at different temperatures

How we can interpret the present results regarding the chemical bond (and chemical form) of radionuclides in irradiated nuclear graphite? For tritium, three binding possibilities can be considered:

- As strongly adsorbed tritiated water (HTO),
- In oxygen-containing functional groups (e.g. C—OT),
- As hydrocarbons (C—T).

The main release mechanisms for tritium are desorption of HTO, pyrolysis of functional groups and hydrocarbons, and following diffusion of HT and HTO.

For radiocarbon, the interpretation is relatively simple on account of its release characteristics: Radiocarbon is covalently bound with the graphite structure. There is a homogeneously distributed part probably coming from the activation of ^{13}C and a heterogeneously distributed part (enriched on surfaces or in hotspots) probably coming from the activation of ^{14}N . The chemical form of radiocarbon is elemental (association of atoms with the same proton number). Therefore, radiocarbon can be removed from graphite only by oxidation methods. This means that radiocarbon has to be transformed into volatile chemical forms, e.g. ^{14}CO or $^{14}\text{CO}_2$. This does not mean that ^{14}C could not be bound to heteroatoms to a very small part ($< 1\%$) and dependent on the irradiation conditions in the nuclear reactor. It has been demonstrated that, for example, methane can be formed in a high-temperature reactor by radiolytic corrosion [11]. This methane could contain ^{14}C -methane which could be adsorbed in the pore system of the graphitic components of the reactor. A direct proof of this assumption is not possible due to the low amount of ^{14}C -methane involved.

All agents to initiate oxidation reactions or isotopic exchange reactions [12, 13] are already present in nuclear graphite. The presence of the fragments H, CH, O and OH – as well after conditioning of the graphite sample in vacuum – is verified by SIMS, as it can be seen in Fig. 27.

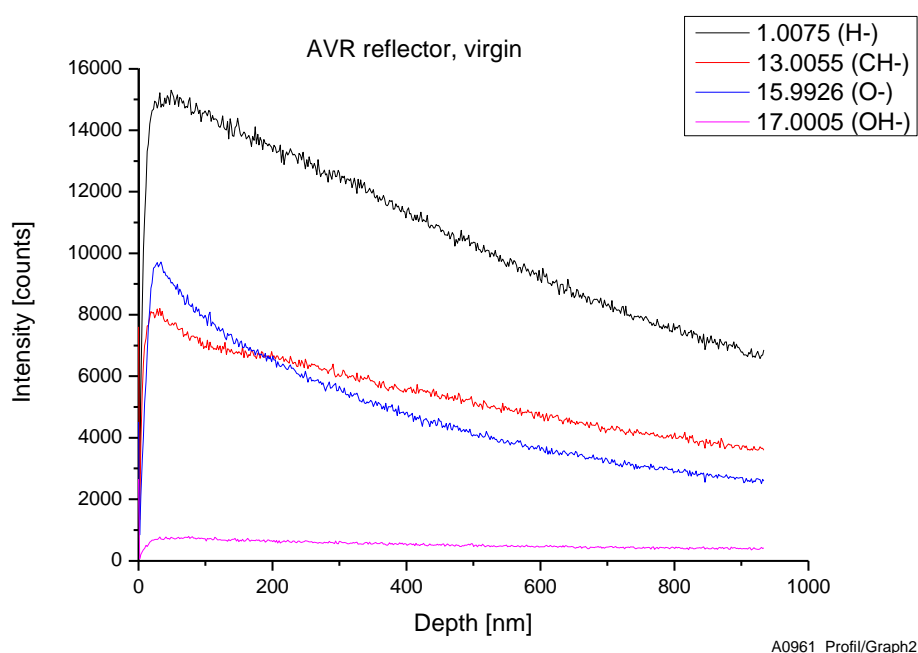
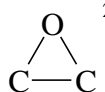
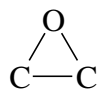


Fig. 27: Depth profiles of the fragments H, CH, O and OH in virgin AVR reflector graphite

X-ray photoelectron spectroscopy (XPS) indicates ether and epoxy structures on the surface of graphite. The binding energies and the assigned structure elements [14] are given in Table 1.

Table 1: Assignment for the C1s and O1s components of the XPS spectra of AVR fuel pebble graphite

Comp.	Assignment	Virgin graphite		Irradiated graphite	
		Energy [eV]	Amount	Energy [eV]	Amount
C1	C–C sp ²	284.2	77.8%	284.2	70.7%
C2	C–C sp ³	285.0	14.9%	285.1	13.6%
C3	C–O–C ¹⁾ ,  ²⁾	286.1	4.6%	286.1	4.1%
O1	no assignment	–	–	530.5	0.8%
O2		531.9	1.3%	531.9	6.4%
O3	C–O–C	533.2	1.4%	–	–

¹⁾ Ether structure

²⁾ Epoxy structure

The formation of graphite-oxygen surface complexes when graphite is exposed to oxygen or oxygen-containing gases like air is also discussed by El-Genk [15]. A variety of surface complexes has been identified, as it is shown in Fig. 28.

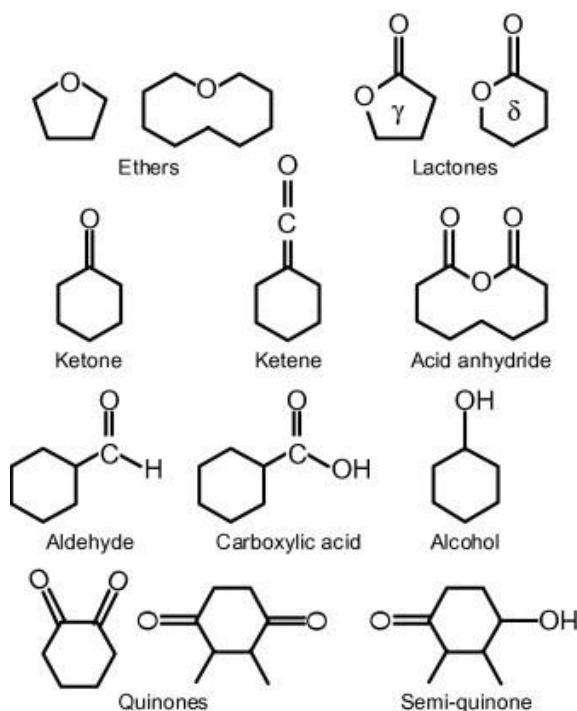


Fig. 28: Plausible organic compounds forming on graphite surface due to oxygen adsorption [15]

The realisation of the covalent bond of oxygen on graphite surfaces leads to an advanced structural model. We observed that by thermal treatment of graphite in pure inert gas at temperatures higher than 1000 °C ^3H and ^{14}C are mainly released as HT (or T_2) and ^{14}CO , respectively. This release takes place up to a certain amount and then stops. The assumption is that HT and ^{14}CO are already preformed on graphite surfaces as functional groups. These functional groups pyrolyse by thermal treatment to HT and ^{14}CO . Fig. 29 shows a model how such a graphite surface might be chemically composed. In this model ^{14}C is bound in form of quinones, ketones and ketenes and ^3H as C-T and C-O-T groups, wherein the C-O-T group is also capable of dissociating single tritium atoms.

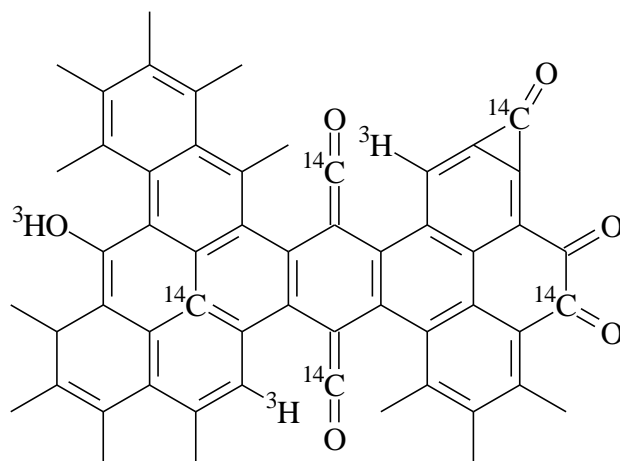


Fig. 29: Model of a graphite surface with ^3H and ^{14}C as functional groups

Another interesting result of XPS is the detection of sp^3 hybridized carbon in graphite. Normally, all carbon atoms in an ideal graphite crystal are sp^2 hybridized. The presence of sp^3 hybridized carbon atoms indicates defects in the graphite crystal. According to Ref. 4 (see Fig. 10), such defects can also be interstitial atoms. It is known from “hot chemistry” experiments of ^{14}C or ^{11}C that a hot carbon atom coming from a nuclear reaction reacts with carbon double bonds to form an excited cyclic intermediate [16]. This intermediate can be stabilised between the graphite lattice planes forming a spiro-pentane structure with the opposite graphene ring. All carbon atoms of this structure should be sp^3 hybridized. Fig. 30 shows a simplified model of this structure.

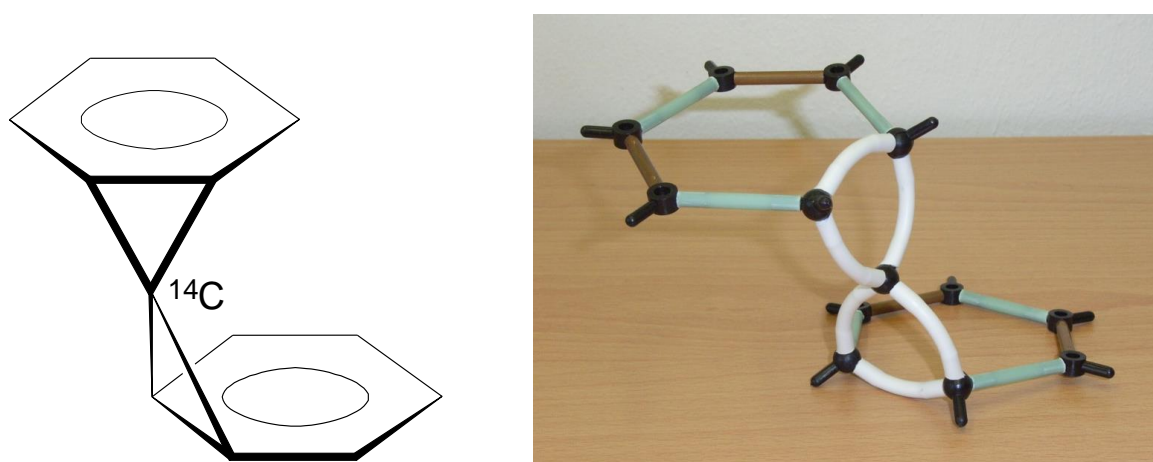


Fig. 30: Simplified model of a ^{14}C interstitial atom in graphite

5.3 Electrolysis

A special form of chemical treatment of irradiated nuclear graphite is electrolysis. By action of the electric current it is possible to study the electro-migration of charged particles. In this way conclusions on ionic radionuclides in neutron-irradiated graphite can be drawn.

The release of radionuclides from graphite by electrolysis passes in two steps:

1. Disintegration of graphite by intercalation (and/or formation of graphite oxide) [17],
2. Anodic oxidation of radiocarbon (to $^{14}CO_2$ which is accumulated in the anodic off-gas) and leaching of the other radionuclides by isotopic exchange (tritium) or electro-migration (metal ions).

The decontamination results of an electrolysis experiment with AVR fuel pebble matrix graphite are summarised in Table 2.

Table 2: Radiochemical analysis of the electrolysis products

Nuclide	Graphite sample	Electrolyte	Electrode (stub end)	Graphite oxide
---------	-----------------	-------------	----------------------	----------------

	A [Bq/g]	Accumulation	(40% of graphite mass)		(60% of graphite mass)	
			Release	Residual	Release	Residual
H-3	3.2E+05	36%	76%	24%	86%	14%
C-14	5.7E+03	0%	87%	13%	79%	21%
Co-60	1.9E+02	48%	30%	70%	60%	40%
Sr-90	9.5E+03	87%	96%	4%	80%	20%
Cs-137	1.2E+04	83%	76%	24%	87%	13%
Ba-133	4.9E+01	48%	26%	74%	61%	39%
Eu-152	2.0E+02	43%	0%	115% ¹⁾	80%	20%
Eu-154	1.7E+02	56%	36%	64%	69%	31%

¹⁾ Enrichment

The high release rates of almost all radionuclides, esp. tritium and radiocarbon, are remarkable. This effect occurs mainly by opening of the closed graphite pores and by exfoliation of the graphite particles, as it can be seen in Fig. 31.

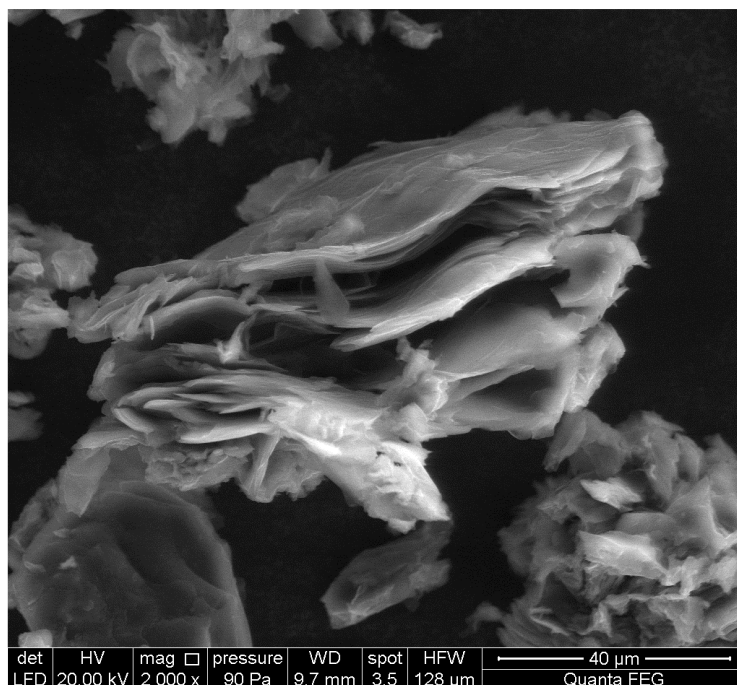


Fig. 31: Scanning electron micrograph of a graphite oxide particle

The formation of graphite oxide is accompanied by a mass gain (measured range from 17 to 23%), but there is also a release of carbon of about 1.5% [18]. Considering the total carbon

release, a radiocarbon release of 79% (see Table 2) results in an enrichment factor of 53 in the off-gas!

Another important observation appears in Table 2: The release factors of all radionuclides are different from each other. In the present case, the highest release factor has Sr-90 with 96%. This is due to a surface contamination of this AVR fuel pebble matrix graphite which is easily removable. Other radionuclides like Co-60 are removable only up to a certain part. This implies that under defined conditions there is a removable part and a non-removable part of these radionuclides. An explication could be that one part of these radionuclides is in ionic form whereas the other part forms very stable carbides with graphite. The ionic part can be removed easily by dissolution in aquatic media whereas the other part is nearly insoluble in water (and in most of the acids). The formation of very stable metal-carbon compounds is verified by SIMS (see Fig. 32). Co-59 was implanted into graphite and subsequently analysed. The mass spectrum shows a significant amount of cobalt-carbon species. This means that cobalt and carbon are able to form very stable compounds with covalent bonds.

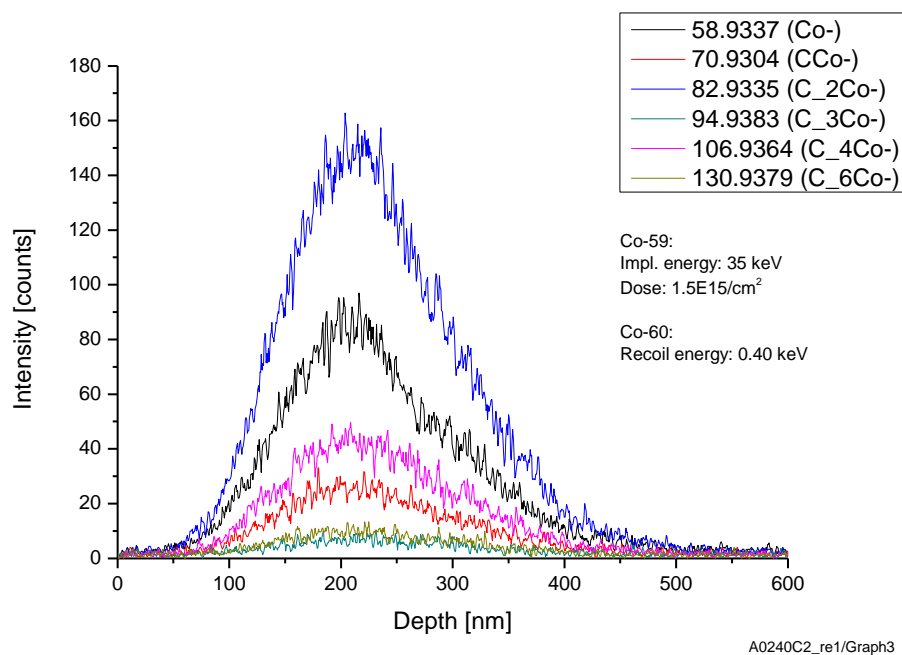


Fig. 32: Depth profile of implanted Co-59 (35 keV) in SLA2 graphite

6. Special Effects on Isotope Sites after Treatment

6.1 SIMS Analyses before and after Thermal Treatment

Two AVR virgin graphite samples were investigated by SIMS (Secondary Ion Mass Spectrometry), cut from the inner part of a massive cylinder of graphite. The sample "AVR square 0" was not treated; the sample "AVR square 1" was treated in a TGA (Thermo Gravimetric Analyzer) under Argon, at 1300 °C for 6 hours. Here are reported some sample's parameters.

Sample "AVR square 0"

Weight	ca. 1.4 g
Treatment:	none

Sample "AVR square 1"

Weight Initial	1.3376 g \pm 0.1 mg
Weight Final	1.3362 g \pm 0.1 mg
Mass Loss	1.4 mg \pm 0.1 mg (0.105% \pm 0.008%)

Parameters:

Argon flow	3.6 l/h
Relative Pressure	1 bar
Treatment	Thermal treatment under argon at 1300 °C
Heating rate	5 °C/min
Holding time at High Temp.	6 hours
Equipment used:	TGA (without weighing)

SIMS parameters

Investigated area	ca. 100x100 μm^2
Primary Ion	Cs+
Energy	2 keV
Sputtered area	ca. 300x300 μm^2

In this special case the TGA was implied only because of its air tightness and not for the on-line weighing: indeed, the shape of the sample did not allow obtaining a proper signal without

a baseline ad hoc.¹ After 4 hours from the thermal treatment a very first SIMS analysis was performed for each sample, revealing some interesting results. A second series of SIMS measurements have been performed about one month later in order to check the results, during which time the sample was stored in ambient air. Taking into account that graphite is not homogeneous, some SEM images were taken to have a closer look at the investigated area (300x300 μm). Before every experiment, vacuum was established for many hours in order to get an inert environment for measuring.

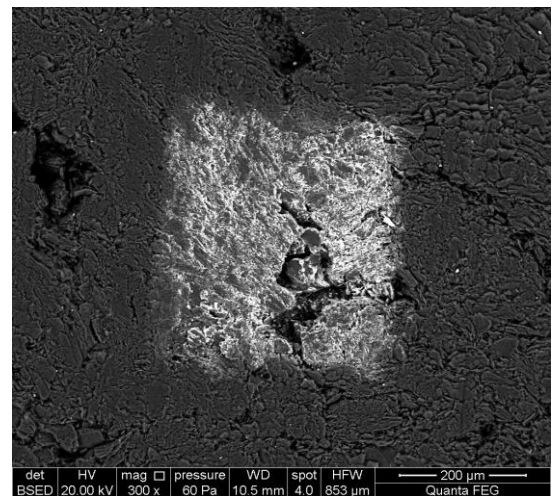
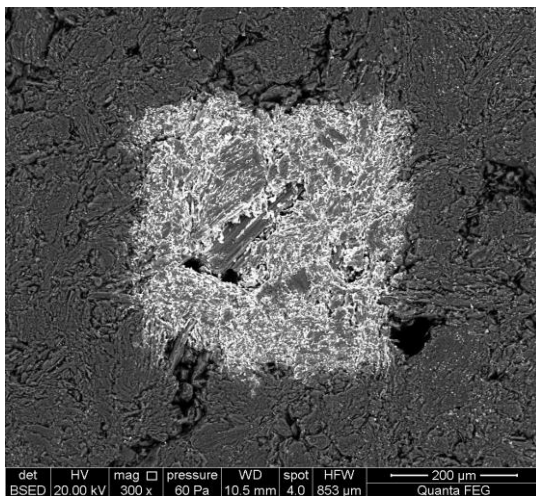


Figure 6.1.1: SIMS area of AVR virgin square 1 treated **Figure 6.1.2: SIMS area of AVR virgin square 0 untreated**

The real area interested by the measurement was about 100x100 μm , in the middle of the crater, to avoid edge effects. Looking at fig. 6.1.1 it can be deduced that the measurement interested partially a filler particle and partially the binder phase; fig. 6.1.2 shows a less clear structure because of the presence of some holes. In the present study no sufficient information are available to separate the measured values by considering the filler or the binder phase, so the obtained data will be compared without doing such distinction.

Considering the background's fluctuations of the mass spectrometer used for the SIMS analyses, a direct comparison among different measurement was not advisable. Then it has been assumed, hypothesis confirmed also from the analysis, a homogeneous distribution of ^{13}C with the depth; actually the very first layers showed to be less enriched of ^{13}C , probably due to an artifact during the manufacture of the sample, so it has been considered only its mean counts value in order to "normalize" with it all the measurements and to do in such a way a more real-

¹ The TGA measures the relative weight during the thermal treatment: a „zero experiment“ is necessary to build a baseline with a non-reactive dummy that, in this case, was not available

istic comparison. The first 50 measured points have been omitted in order to analyze reliable values. Results obtained from one of the analyses showed high fluctuations, so it has been decided to omit them.

The elements of interest are: Sulfur, Chlorine, Nitrogen, Oxygen, Calcium, Lithium and Hydrogen. These elements have been measured as ions in the mass spectrometer, respectively as CN⁻, S⁻, Cl⁻, O⁻, Ca⁻², LiO⁻³, H⁻. In the following, all the results are presented divided by element of interest, in order to have a clearer comparison between the profiles before and after the thermal treatment. Some results are very clear some others need further investigations.

The results are shown in two ways: the one is an integral profile, the other is a three dimensional profile.

Considering as first the integral profile, it represents the measured ion counts versus time. To obtain a depth profile from that a proper calibration time-to-depth would be necessary, since the speed of excavation of the Caesium ion-beam depends strongly on the nature of the specimen. Graphite is a strongly inhomogeneous material and a calibration is not simple. However, it was assumed a total depth at the end of the experiment of about $7 \pm 3 \mu\text{m}$, with the further assumption that the variation of the crater depth is a linear function of the time.⁴ The integral profiles are plotted versus measurement time here, since the uncertainties on the real depth are considerable. The above-cited depth value is used only to give a raw estimation of the real depth.

It was chosen to build also 3D profiles due to uncertainties in the interpretation of some results. In fact, assuming a non-homogeneous distribution of a certain element, i.e. hot spots, the integral profile could lead to wrong interpretations, since the total amount is not representative of the effective structure of that particular element. In particular, a general 3D profile is built by stacking the different 2D distributions obtained for every measurement over the time. In that way a similar-cube shape is obtained, with dimensions of about $100 \times 100 \times 100 \mu\text{m}$. Actually, the depth is only apparent, but necessary to have a clear view of the distribution of a certain element: the real depth is about 15 times smaller.

² The polarity and primary source for this ion is a Cs⁺ ion beam, which will result in very low yield of Calcium ions

³ Same consideration as above

⁴ It is mainly true, except for the first seconds of the measurement.

6.1.1 Sulfur before and after thermal treatment

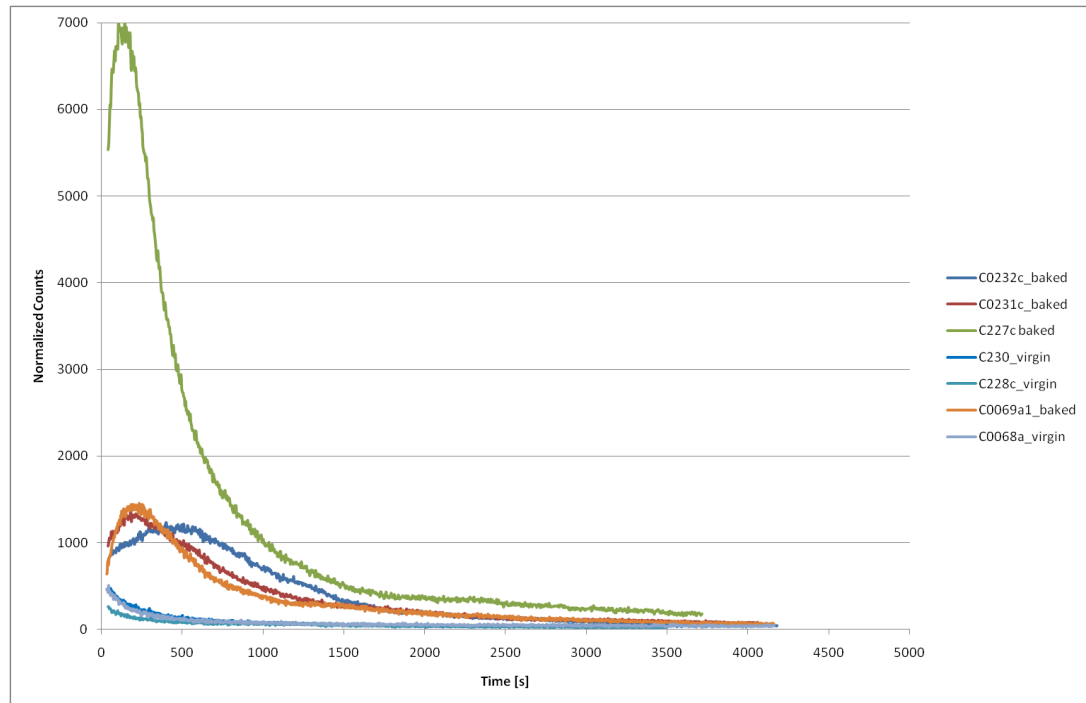


Figure 6.1.3: Comparison among normalized SIMS depth profiles of sulfur as S-, linear plot

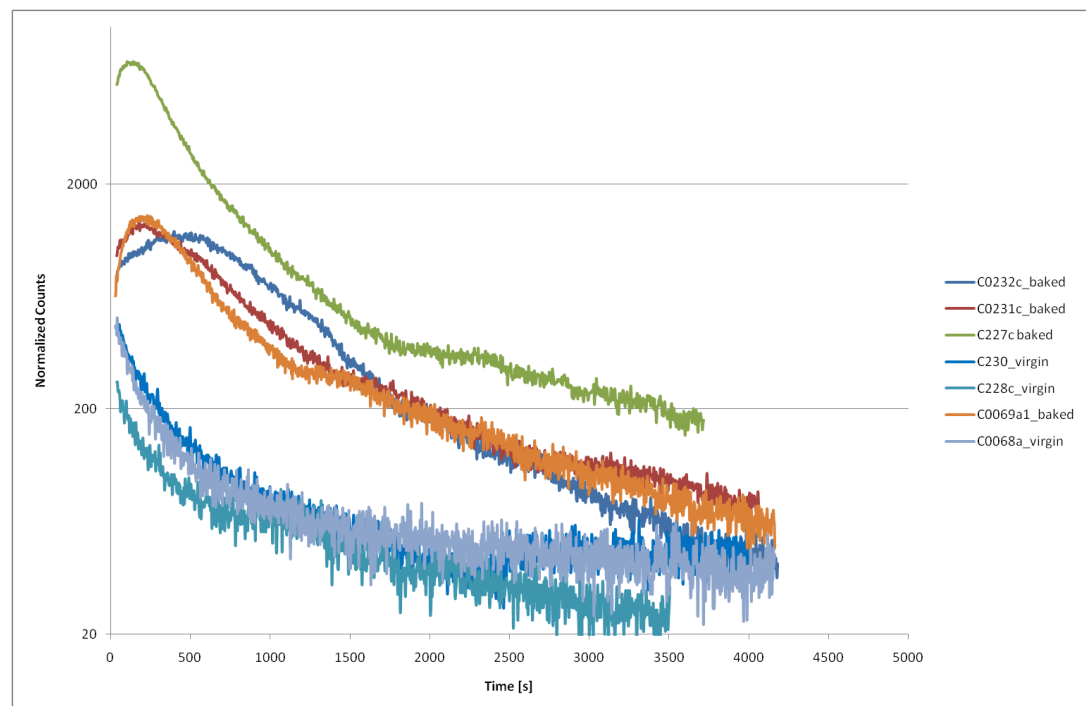


Figure 6.1.4: Comparison among normalized SIMS depth profiles of sulfur as S-, semilog plot

Sulfur was measured for the first time during thermal treatments with on-line gas measurements through a mass spectrometer. Following that, SIMS analyses have been performed to check the hypothesized removal mechanism: the first step of it is the migration of sulfur from the bulk to the sample's surface by thermal treatment. In fact, referring to figs. 6.1.3-4, it can be noticed a consistent increase in the superficial concentration of sulfur after the thermal treatment. The results are reproducible, despite the inhomogeneous nature of graphite. A clearer vision of it can be performed looking at the 3D depth profiles reported in fig 6.1.5: it can be noticed that sulfur is present mainly as hot spots near the untreated sample's surface; during the treatment a migration occurred from the bulk of the graphite, resulting in a high superficial concentration. However, the distribution of the migrated Sulfur seems to be a superimposition of hot spots and a spread distribution.

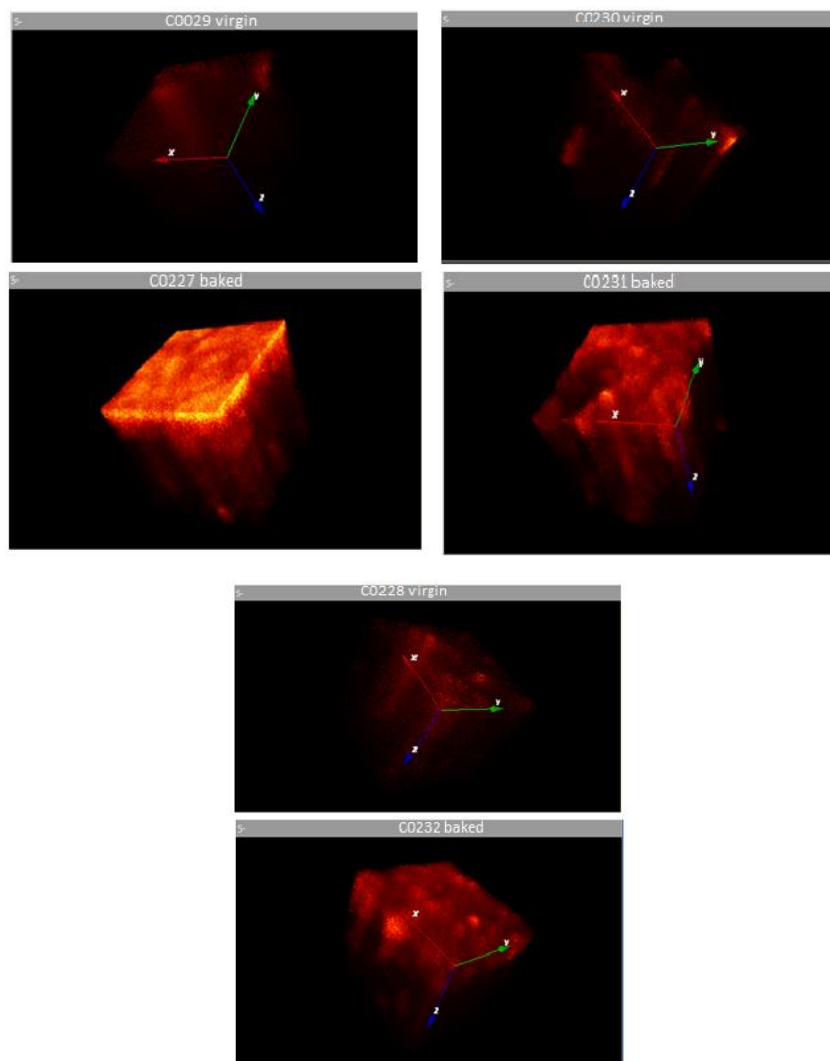


Figure 6.1.5: SIMS 3D depth profiles of Sulfur (S-), before (upper images) and after (lower images)

These results have been confirmed by two other observations:

- A consistent amount of sulfur and especially calcium was found on the Al_2O_3 thermal shield's inner surface, exposed directly to the sample, in an induction oven;
- Some tens of ppm of SO_2 were measured in the gaseous emissions from a massive sample (ca.200g), during a similar thermal treatment in an induction oven;
- Small amounts of sulfur were measured on the surface of the graphite sample, thermally treated in similar experiments, by SEM;

Considering that part of the sulfur (S-34) is a precursor of Cl-36, its removal before using the graphite in a reactor will result in lower amounts of activated product and, consequently, in an easier handling and storage. However, the contribution of the precursor S-34 is only secondary. In conclusion, other experiments should confirm these findings.

6.1.2 Chlorine before and after thermal treatment

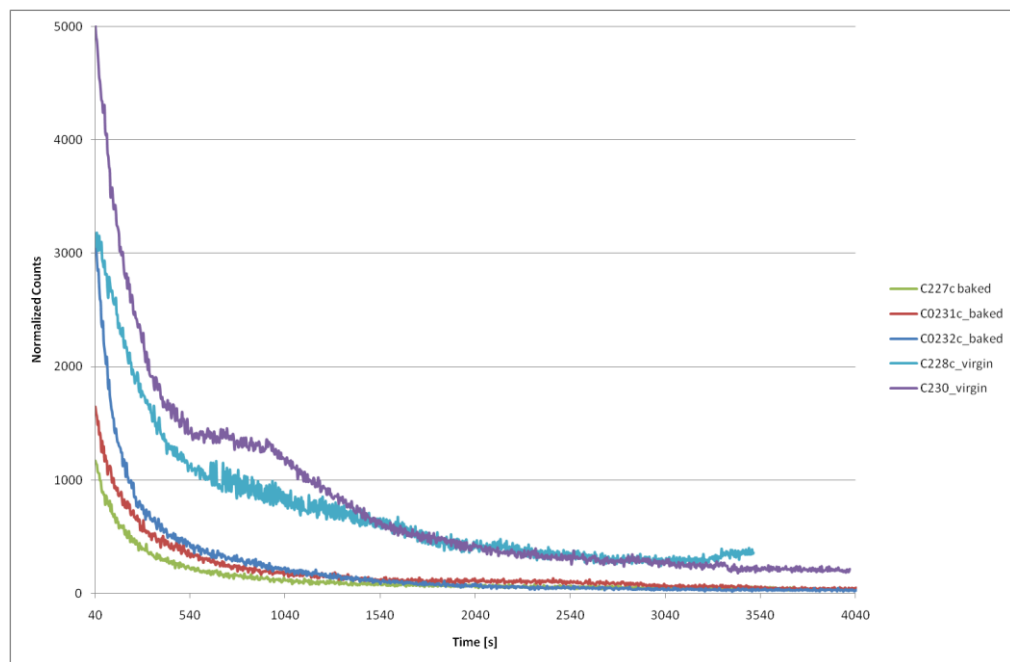


Figure 6.1.6: Comparison among normalized SIMS depth profiles of chlorine as Cl-, linear plot

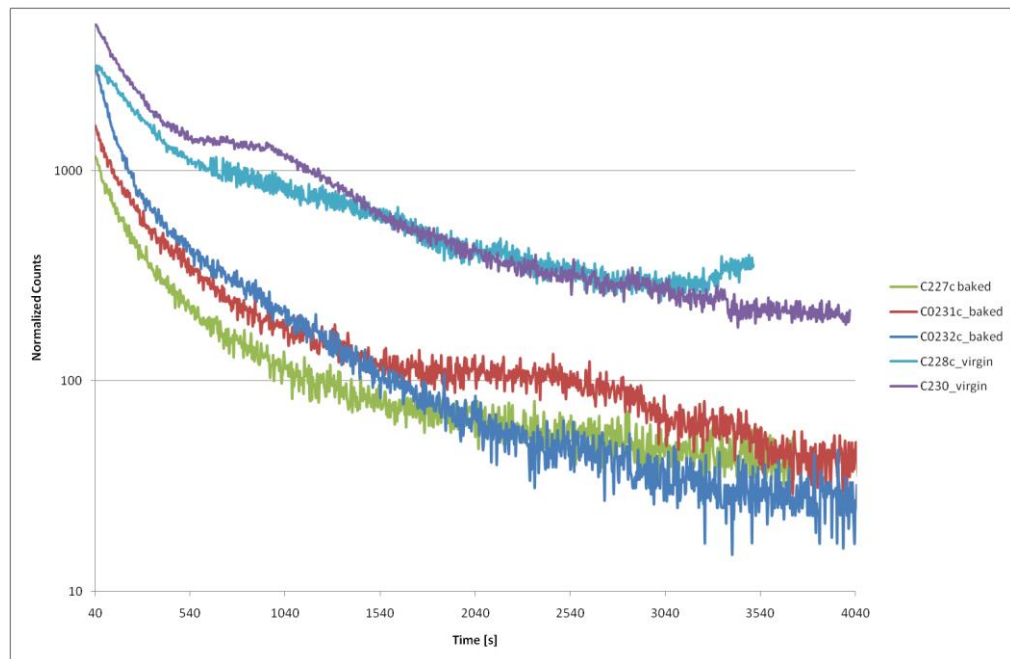


Figure 6.1.7: Comparison among normalized SIMS depth profiles of chlorine as Cl-, semilog plot

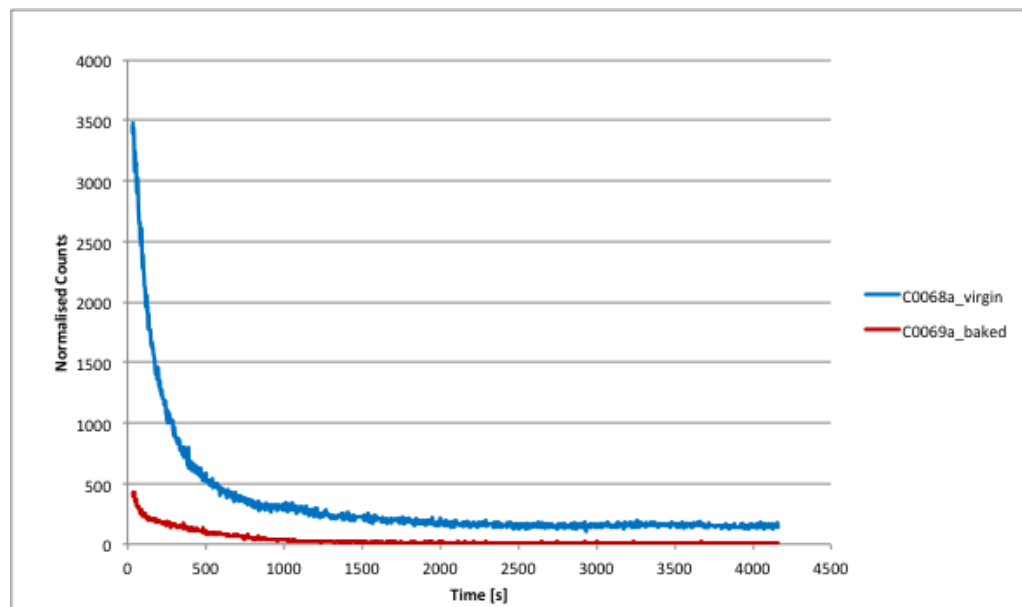


Figure 6.1.8: Comparison among normalized SIMS depth profiles of chlorine as Cl-, linear plot

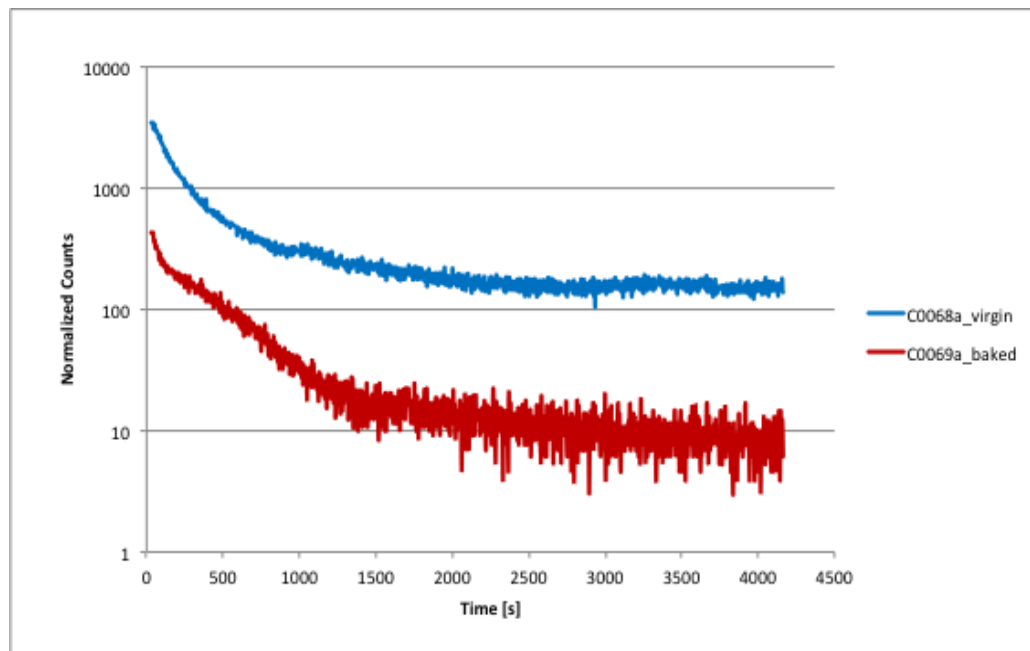


Figure 6.1.9: Comparison among normalized SIMS depth profiles of chlorine as Cl-, semilog plot

Because of a strong variation in the background of the mass spectrometer, it has been chosen to show the results obtained by the different measurements separately: figs. 6.1.6-7 show the values of the most recent analyses; figs. 6.1.8-9 show the results of the first analysis.

Looking at figs. 6.1.6-9 an important integral decrease of the chlorine concentration, mostly at the surface, can be noticed after the baking process. It is confirmed by all the measurements. This result was partially unexpected because Chlorine is present normally as hot spots and the investigated surfaces were artificial ones. One reason of that could have been the presence of a contamination by NaCl, but Sodium was investigated too and it was present in all measurement in negligible amounts compared to Chlorine. On the other hand, however, considering the working principle of SIMS and considering the primary ion beam used in the present case, the presence of NaCl cannot be excluded.⁵ The AVR graphite was not chemically purified during its manufacture, then the other possible origin stands on the raw materials. Further investigations are needed to understand the source of the measured Chlorine. Considering the present analysis it is not possible to determine the chemical form, so further analyses are necessary.

⁵ Indeed the usage of Cs⁺ as primary ion beam is resulting in very low yields for Na and high yields for Cl, which could explain the different values among the two measured elements.

Previous experiments of Vaudrey et al.⁶ showed that chlorine is mainly present as hot spots: looking at the 3D depth profiles (fig. 6.1.10) such observation is confirmed also for the AVR graphite but, differently from the literature results, the typical hot spot dimension is meanly 10 μm in diameter.⁷ Moreover, Vaudrey found that chlorine is present mainly in organic form with a relative fraction of about 70% (by XPS, related to the first nanometers of the sample) or even more (by XANES, related to the first tens of micrometers of the sample); the other fraction was hypothesized to be bound with oxygen. Thermal treatments at temperatures up to 1000 °C showed that the inorganic part was completely removed, at least from the sample's surface (first few nanometers). In the present case, considering the integral profile, it resulted a total mean removal of about 64%. For a better comparison with values obtained in literature⁸, by considering the very first values connected with the first superficial layers it resulted a mean removal efficiency of 71% (see tab. 6.1.1).

Sample	Mean value on surface [counts]	Mean integral value [counts]
Not treated	3627	677140
Treated	1053	242202
Removed fraction	71%	64%

Table 6.1.1: Fractional removal of chlorine, superficial and integral

The obtained results are not in accordance with the ones found in literature. However it can be explained through the presence of many variables: the graphite grade investigated by Vaudrey was a different grade (SLA2) and, in addition, the treatments of Vaudrey experienced maximum temperatures of about 1000 °C, while here 1300 °C were used for 6 hours. Moreover, it is possible that, in the AVR graphite, chlorine is present in different organic/inorganic fractions. More investigations in the future should clarify this point.

A clearer vision of different surface concentrations can be performed looking at the 3D depth profiles of Chlorine from SIMS analysis (fig 6.1.10): the high fractional removal is visually notable. It has to be underlined, however, that the high removal is related to the first microme-

⁶ C.E. Vaudrey, C. Gaillard, N. Toulhoat, N. Moncoffre, M.L. Schlegel, L. Raimbault, "Chlorine speciation in nuclear graphite studied by X-Ray Absorption Near Edge Structure", J. Nucl. Mat. 418 (2011)

⁷ Vaudrey observed spots with a mean diameter of 5 μm

⁸ Vaudrey used XPS analyses to check the effective removal of Chlorine, analyses focused on the first nanometers of the sample's surface

ters in depth from the sample surface. More investigations are necessary to evaluate the release efficiencies from the bulk graphite.

When future investigations will confirm the results here obtained also for i-graphite, a high temperature thermal treatment could represent a good solution for chlorine removal in an efficient way. For what concerns modern graphite, chlorine is present normally in much lower amounts than the ones in AVR graphite, also due to the fact that the purification processes, performed during the manufacture, are normally implying fluorinates. From this point of view, an efficient method for chlorine removal will find most of the applications in the old-grade graphite.

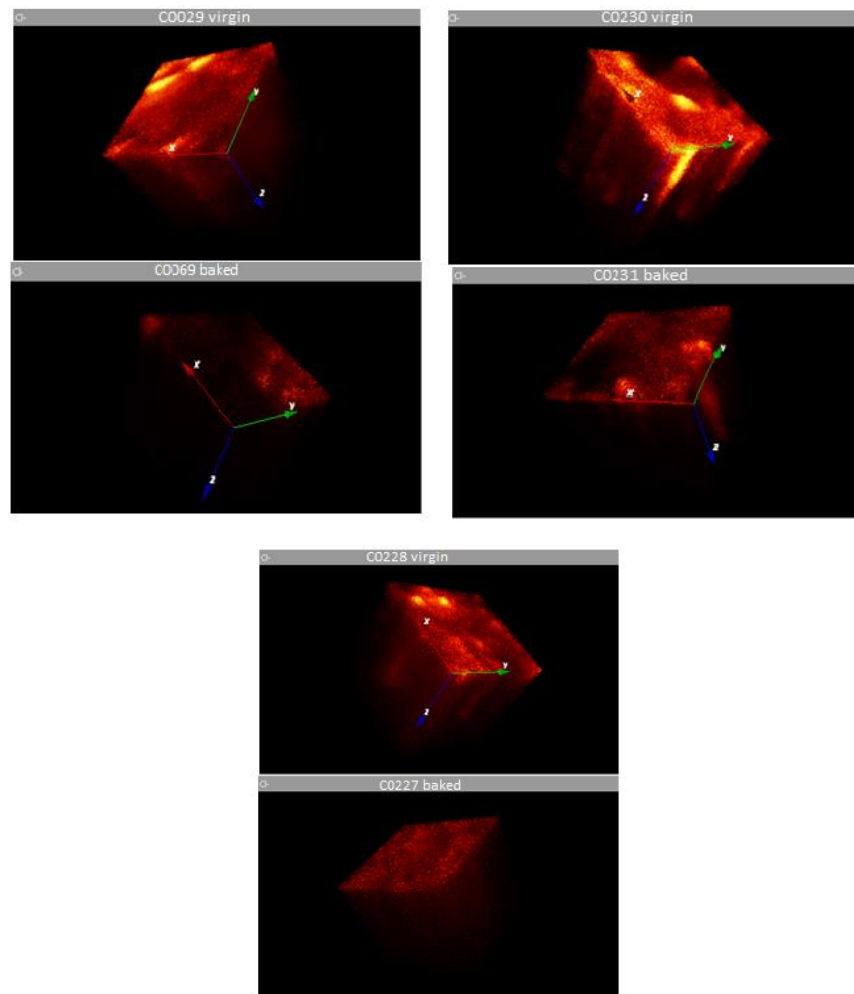


Figure 6.1.10: Comparison among SIMS 3D depth profiles of chlorine as Cl⁻, untreated (upper pictures) and treated (lower pictures)

6.1.3 Nitrogen before and after thermal treatment

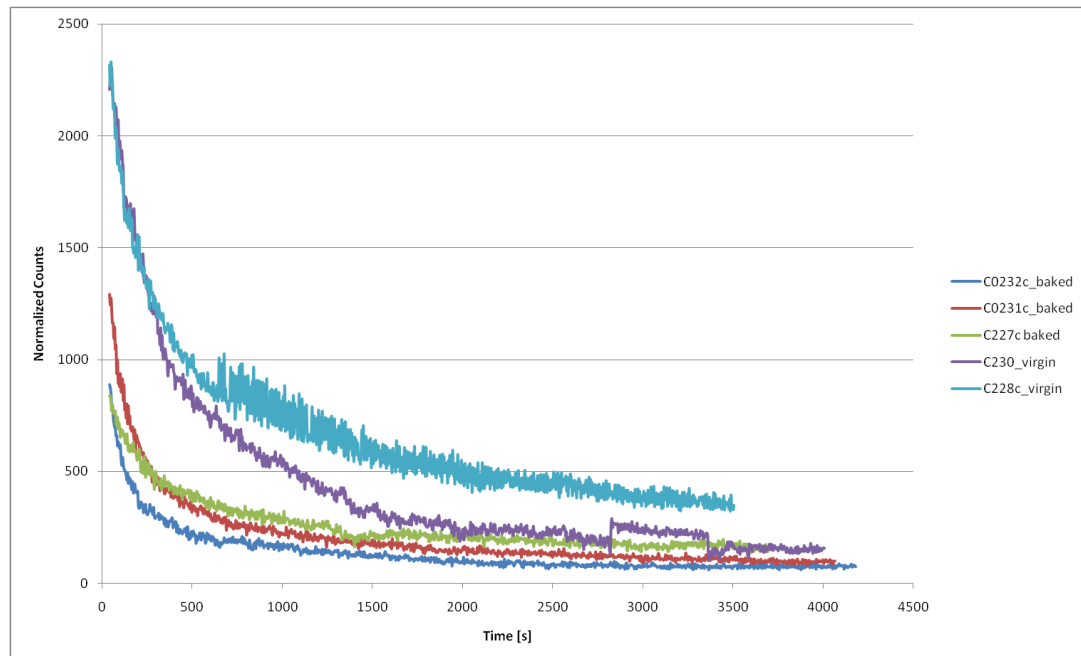


Figure 6.1.11: Comparison among normalized SIMS depth profiles of nitrogen as CN-, linear plot

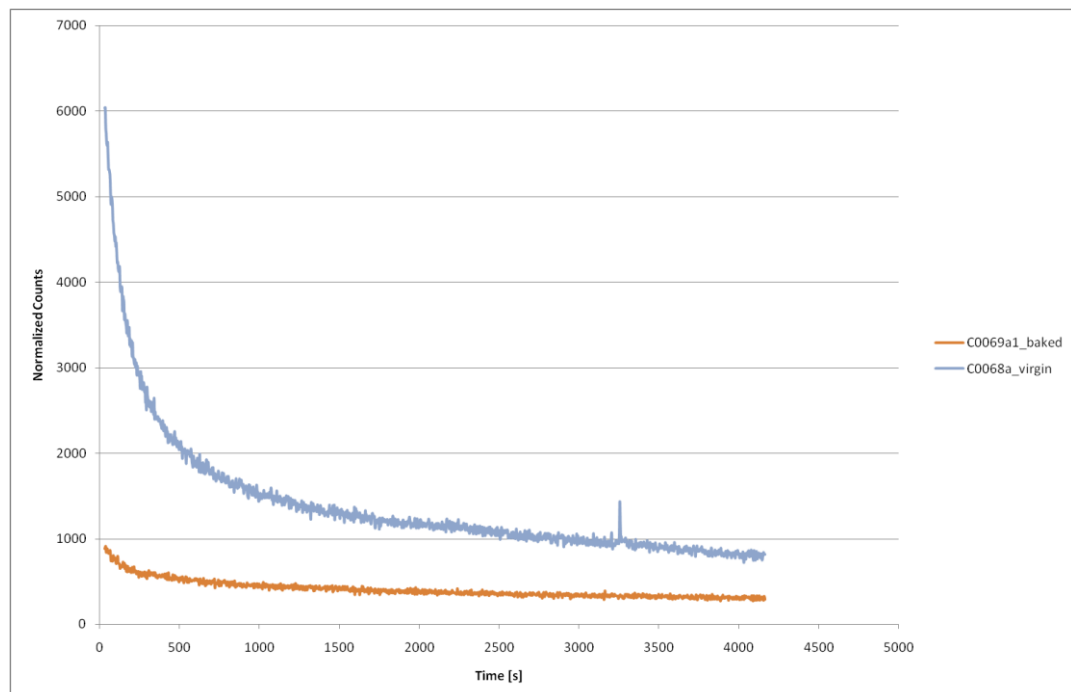


Figure 6.1.12: Comparison among normalized SIMS depth profiles of nitrogen as CN-, linear plot

Due to a strong variation in the background of the mass spectrometer, it was chosen to analyze separately the results obtained by the different measurements: figs. 6.1.11 shows the values obtained by the most recent analyses; fig. 6.1.12 shows the results of the first analysis.

By observing figs. 6.1.11-12 it can be noticed that all the performed measurements are showing a removal of nitrogen, more marked near the surface, after the thermal treatment. Nitrogen can originate from the raw materials, the manufacture process and the long exposure of the sample to ambient air.

Linking to previous experiments of Takahashi,⁹ the results here presented are similar, but the lacking of a precise depth calibration cannot lead to precise results. However, to give a range of values, the high concentration of nitrogen near the sample surface is estimated to extend in depth between 300 nm and 1 μm . Since nitrogen is mainly concentrated on the surface of virgin AVR graphite it is believed that, after its neutron activation, the C-14 distribution will be similar: considering that the range of a recoiled C-14 after its generation is at maximum in the order of the micrometer, the above mentioned hypothesis seems to be validated. A first experimental confirmation of that has been obtained by some experiments of Dr. Vulpus,¹⁰ shown in fig. 8.

If C-14 shows a similar depth profile as N-14, considering that the thermal treatment has removed part of the superficial nitrogen, it is possible to have found an effective removal method. Considering previous works with thermal treatments,^{11,12} it was hypothesized that C-14 was mainly concentrated on the sample's surfaces and released by slight oxidation: this hypothesis seems to be confirmed by the present work. Indeed, some on-line gaseous emissions showed a very marked CO₂ peak during treatments in inert gases of AVR graphite, likely correspondent to the first mobile part removed by slight oxidation of the surfaces: that peak will be presumably one of the most important carriers of C-14 since it is released as first, so it is probable to come from the nitrogen (and successively C-14) enriched surfaces.

Another interesting result stands on the validation of a reasonable hypothesis, i.e. the C-13 distribution is homogeneous: it revealed to be true for all specimens, with the exception of the first superficial layers (see fig. 6.1.13). The superficial decrease of C-13 is probably an artifact due to the sample manufacture.

⁹ R. Takahashi, M. Toyahara, S. Maruki, H. Hueda, T. Yamamoto, "*Investigation of morphology and impurity of nuclear grade graphite, and leaching mechanism of carbon-14*", p.7

¹⁰ Dr. Vulpus, Forschungszentrum Juelich

¹¹ T. Podrzhina, "*Graphite as radioactive waste: corrosion behaviour under final repository conditions and thermal treatment*", Juel 4166, 2004

¹² M. Florjan, "*Dekontamination von Nucleargraphit durch thermische Behandlung*", Juel-4322, 2009

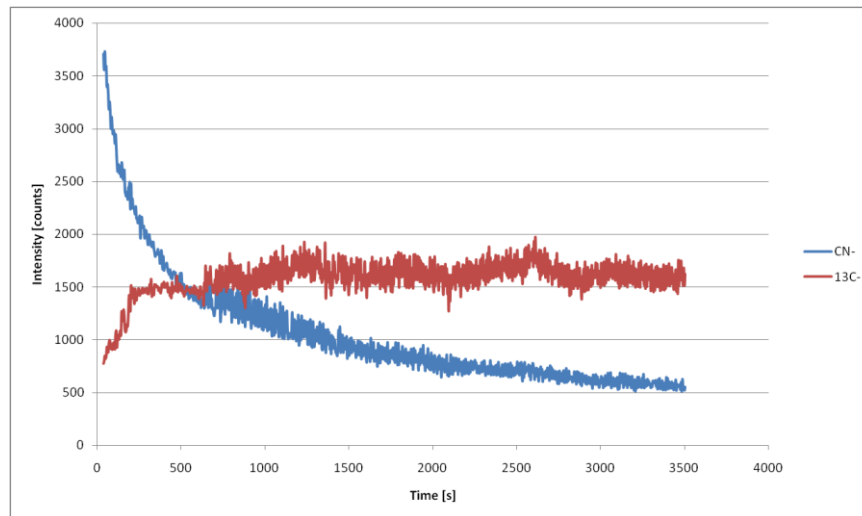


Figure 6.1.13: Comparison among SIMS depth profiles of CN- and ¹³C- of virgin AVR graphite

In the following, the fractional removal factors will be calculated. Two different calculations are performed: the first one is related to the superficial removal, i.e. the first SIMS measurements are considered; the second one is related to the integral removal of nitrogen, considering the entire integral depth profile of every measurement. Indicative values are listed in table 6.1.2.

Sample	Mean value on surface [counts]	Mean integral value [counts]
Not treated	2300 (900)	1122704
Treated	1033 (250)	451356
Removed fraction	55%-72%	60%

Table 6.1.2: Fractional removal of nitrogen, superficial and integral, indicative values

However, in this case some values are really scattered, so it was decided to build a Gaussian curve from the data of all the experiments (see figs. 6.1.14-15). By considering only the second experiment, it results a mean integral fractional removal of 58%; taking into account also the first one, it results a mean of 60%. For what concerns the superficial values, strong differences were observed between the two SIMS experiments, so the relative values had been kept separately, resulting in 72% and 55% respectively for the first and the second experiment. More experiments would be necessary to have a confirmation of such values.

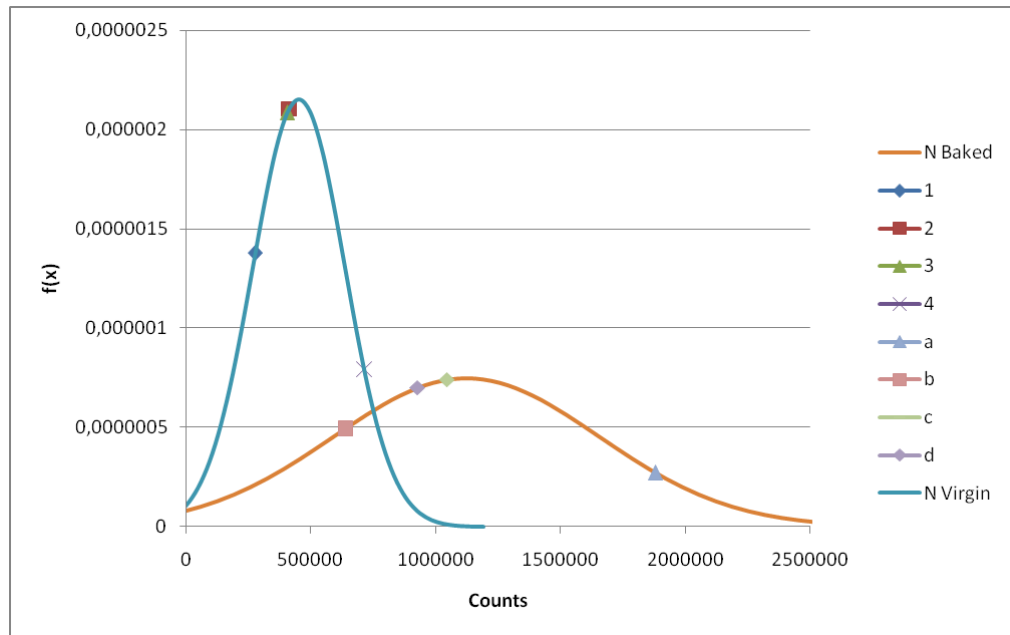


Figure 6.1.14: Gaussians distribution of the (nitrogen) available data from the two SIMS experiments

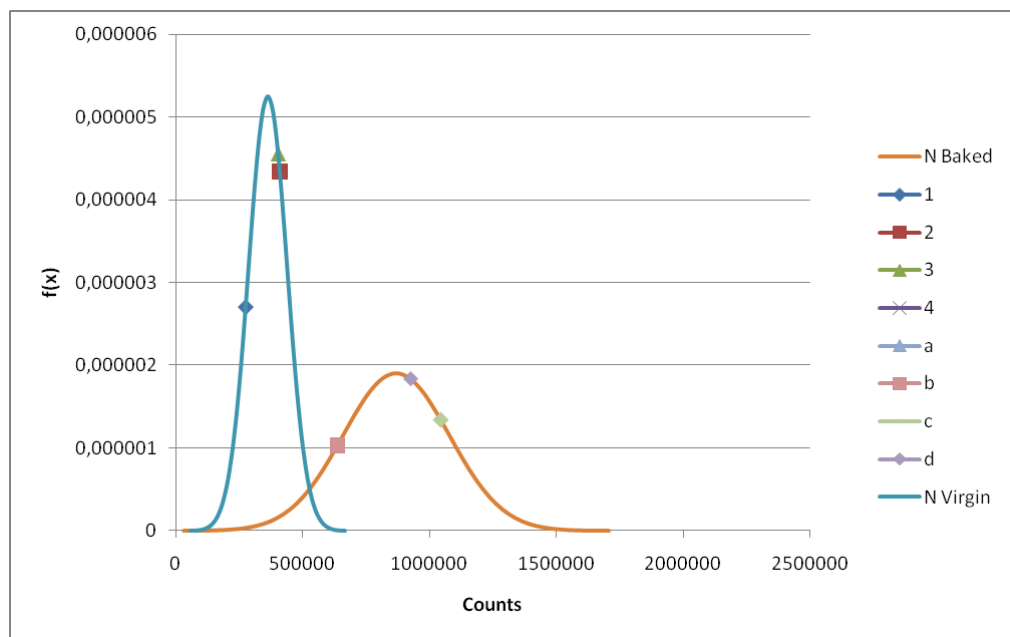


Figure 6.1.15: Gaussian distributions of the (nitrogen) results from the second SIMS experiment

A better comprehension of thermal treatment's effects can be evinced from the 3D profiles of nitrogen (figs. 6.1.16). In the virgin material, nitrogen is present both as hot spots, with a mean diameter of 10 μ m, and as a spread distribution over the surface, with an evident inhomogeneous character. Comparing the profiles before and after thermal treatment (fig. 6.1.16), the removal effect is not very marked but, excluding the results from sample c0321, it can be noticed

a trend in the direction of a partial nitrogen removal, with lower removal efficiencies than the ones for Chlorine.

In conclusion, a general removal of nitrogen from the superficial layers occurs during the thermal treatment, with a removal factor in the order of 50%. Considering that the radiocarbon is concentrated the more on the surfaces, it can be stated that the treatment is efficient only for that fraction: a high temperature thermal treatment under argon atmosphere can be used to improve the leaching behaviour by depleting the most mobile part of radiocarbon with a fractional removal up to some tens of percent, as observed in previous experiments by Florjan.¹³

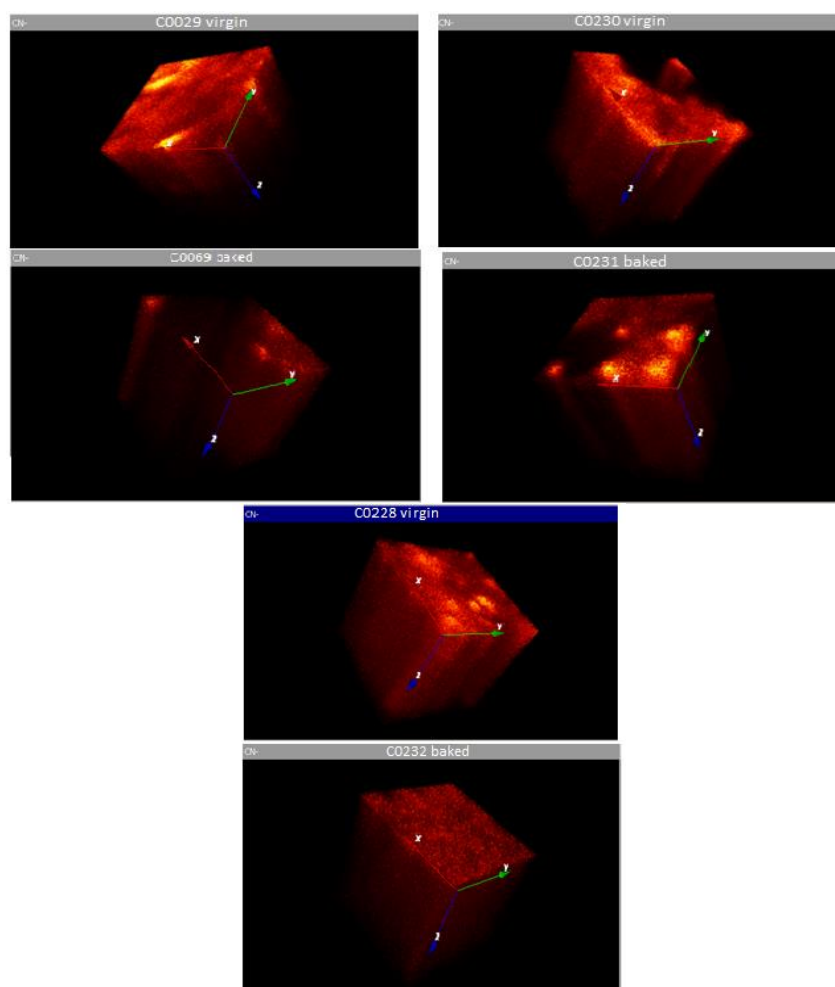


Figure 6.1.16: Comparison among SIMS 3D depth profiles of nitrogen as CN-, untreated (upper pictures) and treated (lower pictures)

¹³ M. Florjan, "Dekontamination von Nucleargraphit durch thermische Behandlung", Juel-4322, 2009

6.1.4 Oxygen before and after thermal treatment

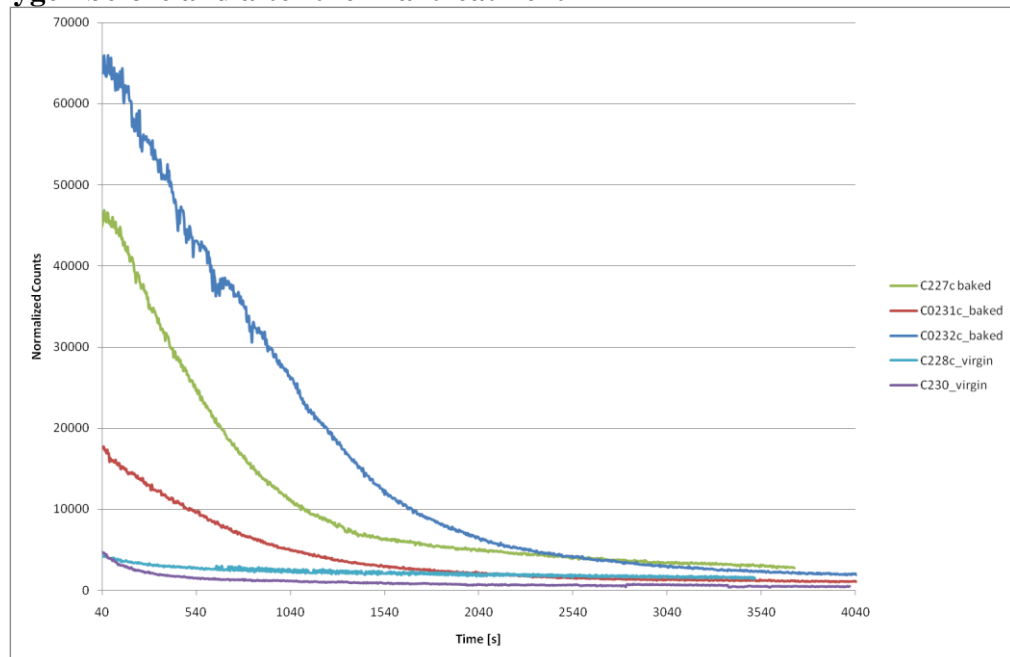


Figure 6.1.17: Comparison among normalized SIMS depth profiles of oxygen as O-, linear plot

All measurements showed a high increase of the oxygen concentration after thermal treatment, in particular on the outer layers of the specimen (see fig. 6.1.17).

A hypothesis to explain that consists on a higher surface area after the treatment: the higher the available surface, the more the adsorbed (chemisorbed) oxygen. Indeed, considering SEM images (fig. 6.1.18) taken before and after thermal treatment, one can observe real structure changes, with partial exfoliation of the graphite layers or even disappearance of some graphitic structures.

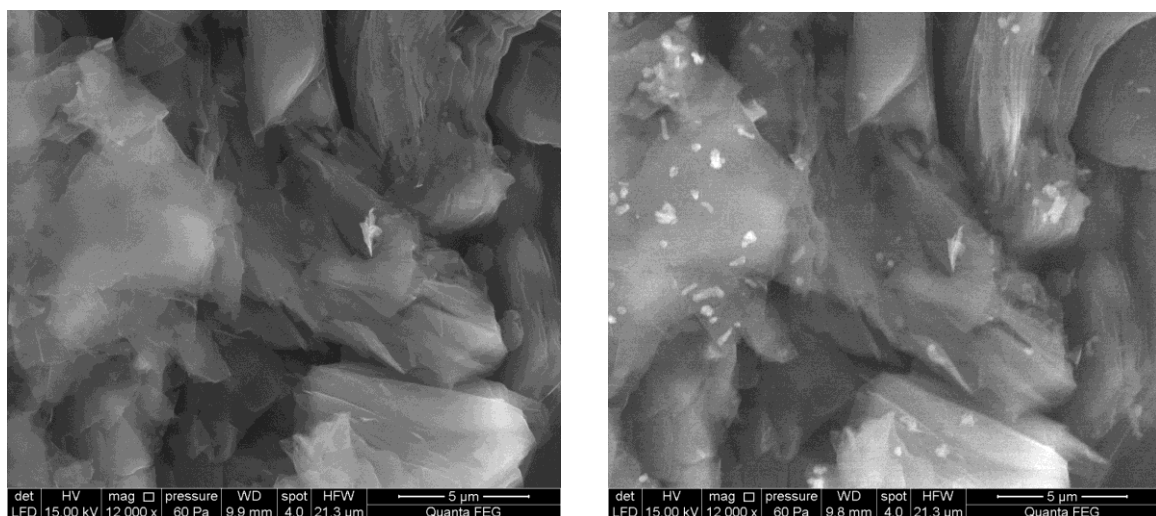


Figure 6.1.18: Comparison among SEM images before (left) and after (right) thermal treatment in argon

If this were the case, one should expect, in line of principle, an increase in the amount of the adsorbed nitrogen, coming from air; this is not the case. It is necessary to investigate the more on the oxygen and nitrogen bonds and adsorption/desorption mechanism to come to a conclusion. Another hypothesis, linked to the origin of such increase of oxygen, could be related with the boundary conditions during thermal treatment: the usage of a mass spectrometer allowed to discover a considerable amount of water from an external source, during the treatment; at high temperatures (1300 °C), the established regime is the "mass transfer" one, so all the reactions are taking place at the sample's surface. Following these considerations, it is reasonable to expect higher amounts of oxygen after thermal treatment, since a fraction of the oxidized graphite is likely to be not removed from its structure at the end of the treatment: considering a Langmuir-Hinshelwood reaction scheme, before being released to the gas phase the chemical species react on the surface, but a decrease in the temperature could freeze the release, resulting in higher amounts of graphite oxide found on the surface. So the water-presence explanation seems to be the most reasonable.

An analysis of the 3D profiles (fig. 6.1.19) reveals again a very marked increase of oxygen, mainly near the surface.

Considering virgin graphite, oxygen was found to be present as a superimposition of hot spots (identified as impurities) and a spread distribution over the surface (most probably chemisorbed oxygen, present in slightly higher amounts on the surface). This leads to the conclusion that oxygen is already present inside the graphite, and even though its amount is limited, it is likely to be one of the responsible for graphite oxidation and species removal under treatments in inert atmosphere. In particular, it is believed that the embedded oxygen (both sorbed on the micro or macro structure) is causing a slight oxidation of the inner and outer graphite surfaces, leading to a depletion of the surface-enriched radiocarbon. These conclusions are in accordance with all the experiments, performed in the past by Podruhzina and Florjan, showing a steep initial release of radiocarbon during thermal treatment under inert atmosphere. More in detail, a particular experiment of Florjan (see fig. 21) consisted in several treatments on the same sample, under inert gas, with intermediate exposure to air: it was observed a steep release of radiocarbon during the first treatment steps, in decreasing values in every treatment but with similar emissions. It is possible that after the first treatment the small amount of chemisorbed oxygen on the surfaces were the responsible of the steep release. The conclusion that the release of

radiocarbon is not temperature dependent, but it is correlated with superficial oxidation of graphite surfaces, seems to be validated.

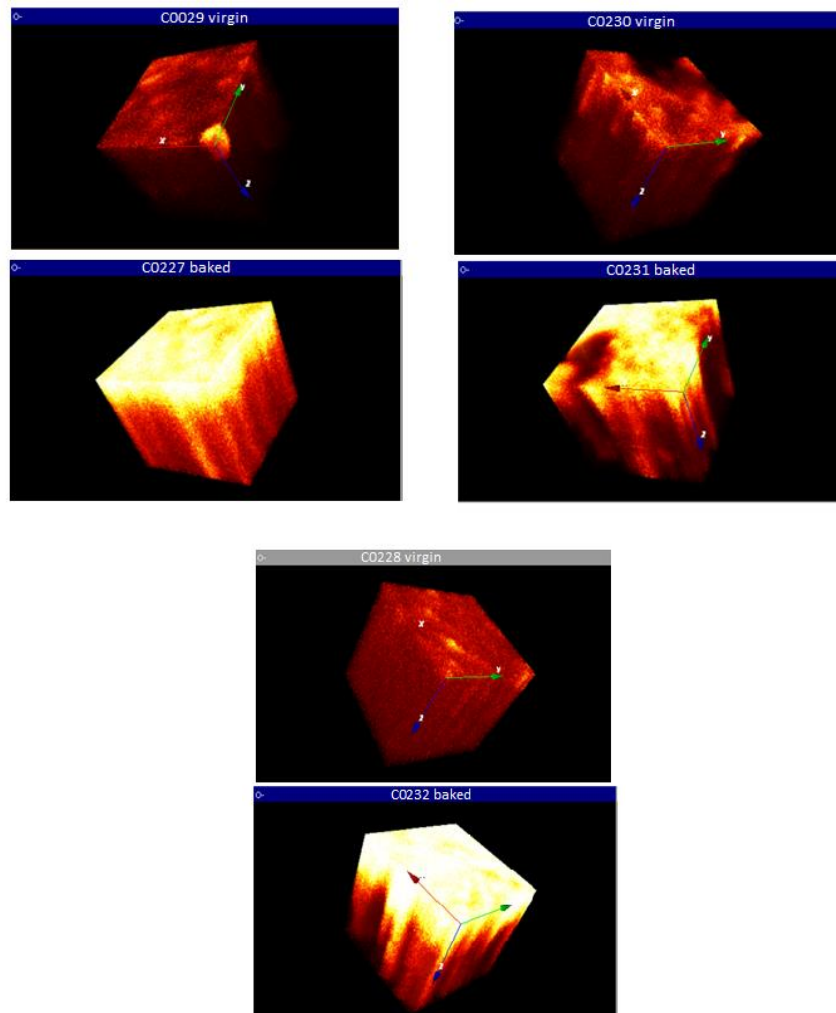


Figure 6.1.19: Comparison among 3D SIMS depth profiles of oxygen as O-, untreated (upper pictures) and treated (lower pictures)

6.1.5 Hydrogen before and after thermal treatment

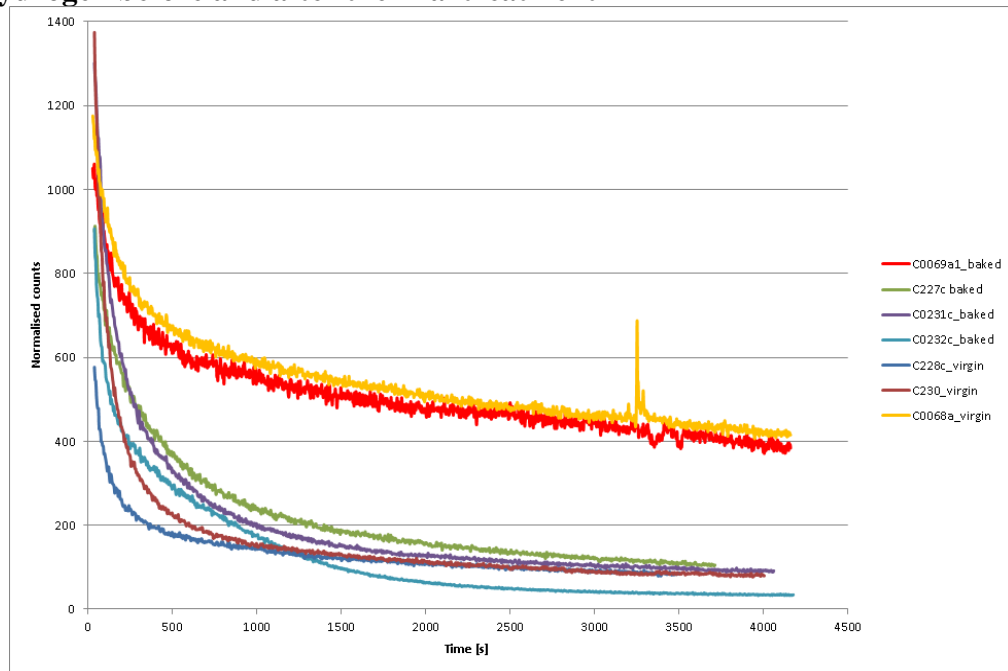


Figure 6.1.20: Comparison among normalized SIMS depth profiles of hydrogen as H-, linear plot

Because of the different background of the mass spectrometer between the first experiment and the second one, the profiles comparison is kept separated. In particular, considering fig. 6.1.20, the first measurement provided the yellow and red line while the second provided all the others: there is no significant difference among the profiles, considering the ones taken during the same experiment. This finding supports the reaction of graphite with water, since the generated hydrogen is released into the gas phase while the oxygen bounds the available carbon atoms. However, it is believed that small amounts of hydrogen are present as H- or OH- functional groups, but different analyses are necessary to measure them. As an example, a PGNA (Prompt Gamma Neutron Activation Analysis) showed 74 ppm_w of hydrogen present inside the graphite specimen.¹⁴

¹⁴ Zsolt Révay, PGNA, December 2010, Nuclear Research Department, Institute of Isotopes, HAS, Budapest, Konkoly-Thege Miklosutca 29-33. 1121 Hungary

6.1.6 Lithium Oxide before and after thermal treatment

Lithium oxide has been investigated too. However, the yield of LiO^- is very low due to the usage of Cs^+ as a primary ion beam in the SIMS analyses. Some information are anyway obtainable from the 3D depth profiles (fig 6.1.21). It can be noticed a nearly homogeneous distribution of LiO^- in form of hot-spots. It seems that after the baking process the concentration is increased, but it is most likely due to the higher oxygen content, as showed before.

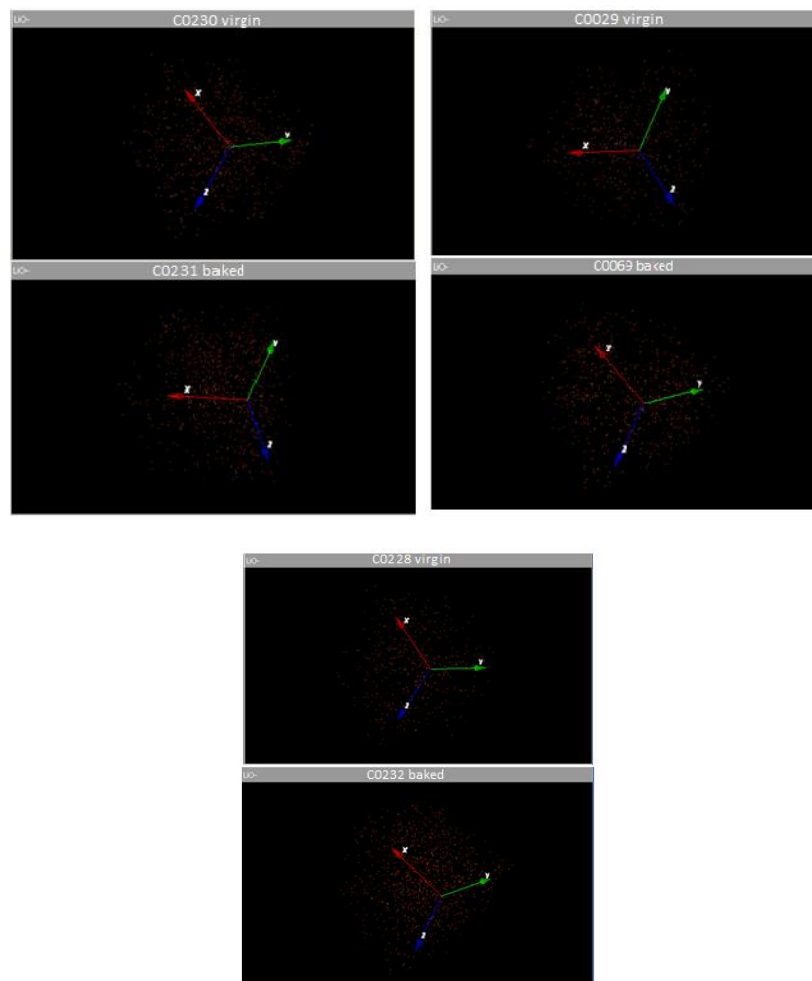


Figure 6.1.21: Comparison among 3D SIMS depth profiles of LiO^- , untreated (upper pictures) and treated (lower pictures)

6.1.7 Calcium as CaO- and CaC- before and after thermal treatment

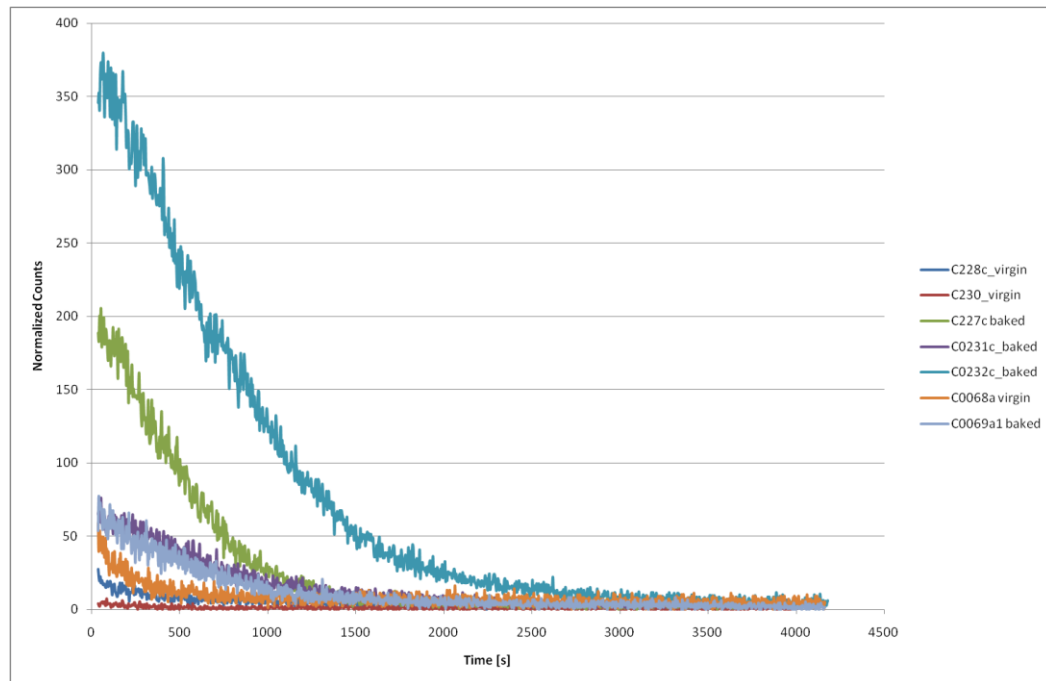


Figure 6.1.22: Comparison among normalized SIMS depth profiles of calcium as CaO-, linear plot

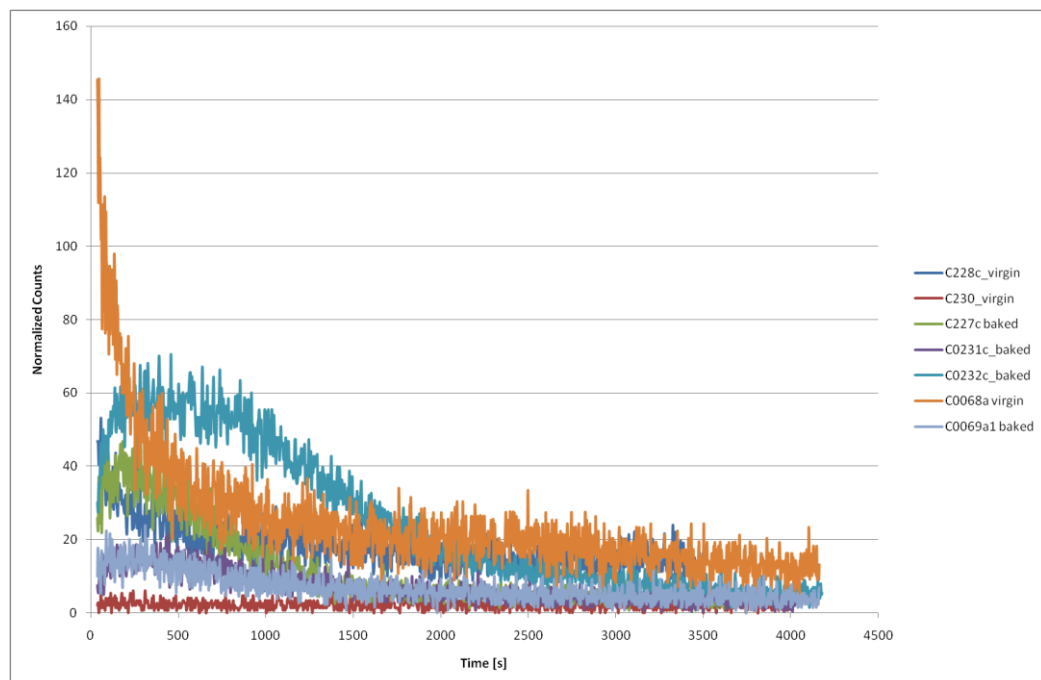


Figure 6.1.23: Comparison among normalized SIMS depth profiles of calcium as CaC-, linear plot

Some SEM + XRF investigations showed high concentration of Calcium, not homogeneously distributed, on the thermally treated sample's surface (see fig. 6.1.18). Some crystallized calcium sulfate has been observed by SEM + XRF analysis also in the Al_2O_3 thermal shield, placed around the sample during the thermal treatment. Starting from that it was expected a similar result from SIMS analysis. Indeed, looking at fig. 6.1.22, it is clear that the concentration of CaO^- on the sample surface increased due to the thermal treatment. Such increase shows different magnitudes because of the not homogeneousness of Calcium, but a general trend can be noticed. Differently, looking the CaC^- profiles in fig. 6.1.23, the treatment effect is not very clear, since the differences are not significant as for CaO^- . The reasons of that could be:

- Small differences are due to the not homogeneousness of the sample, so measured profiles are normally different in graphite: there is not a real thermal treatment effect for CaC^- .
- As underlined by the SEM images of SIMS-interested areas, choosing the “white area”¹⁵ for the baked sample was not possible because of the raw pointing equipment provided with SIMS, so even though there were net effect on CaC^- due to the thermal treatment it was not measured because of the chosen SIMS-interested areas.

Elemental Calcium was observed in negligible amounts, most probably due to the fact that Cs^+ was used as primary beam, which generally gives low yields of Calcium ions.

Looking at the 3D profiles, the thermally treated graphite shows a general increase in the superficial concentration. Less clear are the results for CaC^- . (see figs. 6.1.24-25).

In conclusion Calcium revealed to have migrated to the sample surface during the thermal treatment, as confirmed also by SEM and XPS (see section 6.2) analyses. The removal of calcium was never measured before, so further analyses are necessary to confirm what has been observed here. Linking the discovery to the AVR i-graphite, it has to be reminded that Ca-41 is present in significant quantities, even though much lower than C-14 or H-3. The present results could represent a step in the removal of radioactive calcium, for example by mechanically removal of the sample's surfaces, enriched of calcium after the thermal treatment.

¹⁵ Calcium was found to be spread over many inhomogeneous areas on the sample surface.

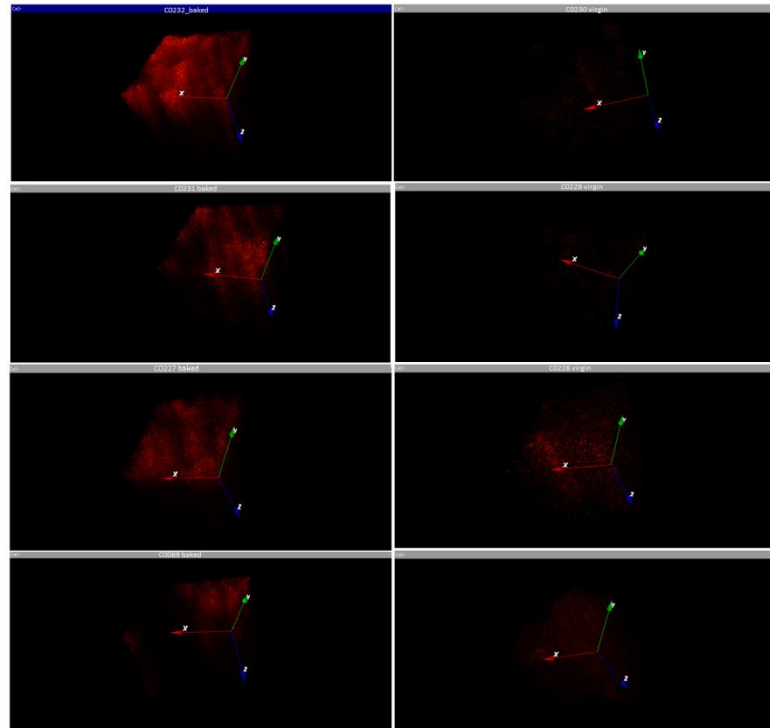


Figure 6.1.24: Comparison among 3D SIMS depth profiles of calcium as CaO-, after (left) and before (right) thermal treatment

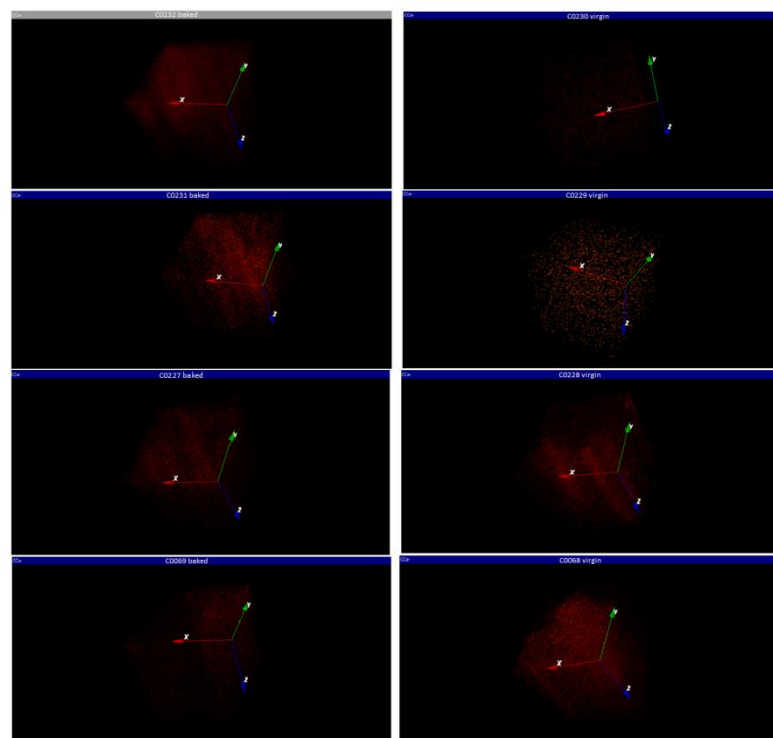


Figure 6.1.25: Comparison among 3D SIMS depth profiles of calcium as CaC- after (left) and before (right) thermal treatment

In conclusions, for what concerns SIMS analyses, high temperature thermal treatments have shown a real influence on many impurities, evident for sulfur, chlorine, calcium and in a lower extent on nitrogen. Lithium Oxide was measured inside the graphite matrix in a nearly homogeneous distribution of hot spots. Sulfur and calcium diffused to the outside graphite surfaces because of the thermal treatment, while chlorine and nitrogen were removed, even though in different ratios. The reason for the very high oxygen concentration originates in the presence of the water-gas reaction at high temperatures. The finding here exposed are in agreement with what was hypothesized in the past, in particular the C-14 distribution showed to be similar to the nitrogen one and its removal by slight oxidation of the porous structure of graphite can reasonably be correlated with the nitrogen removal.

6.2 XPS Analyses before and after Thermal Treatment

The investigated samples are the same ones used in the SIMS analyses (section 6.1): one was untreated while the other went through a high temperature thermal treatment (1300 °C in Argon for 6 hours). The XPS analyses have been chosen to have an ulterior confirmation of the results obtained by SIMS¹⁶ and to look for the bindings of some elements in the superficial layers of the graphite sample, before and after the thermal treatment.

Two measurements for each sample were performed to compare repeatability and to take into account the non-homogeneous nature of the specimen: even by naked eyes it was possible to distinguish different zones on the sample's surface, so the first measurement was taken in a “light spot”, while the second one in a “dark spot”. Indeed, many more measurements would be necessary to do statistical considerations: the reported values have to be considered only for a first approach. However, the results hereby presented could confirm or not some inferred observations resulting from previous experiments.

The investigated components in the XPS spectra were: C1s, N1s, S2p, Ca2p3, Na1s, O1s and Li1s.

¹⁶ It has to be reminded that XPS is related only to the very first nanometers of the sample, while SIMS interested the first micrometers;

The following elements have been excluded after the interpretation of the electronic spectra: CaO, CaCO₃, Na₂CO₃, Na₂C₂O₄, NaN₃, CN₂, Na₂O, Cl, S, Li. Moreover adsorbed H₂O was detected.

The obtained spectra were interpreted and the possible chemical bondings and relative bonding energies were identified via software through a deconvolution of the individual peaks into Gaussian fits. All the percentages were calculated at FWHM, taking as a reference the peak C1s. It was necessary, however, to shift the spectra of about 0.28 eV in order to fit with reference values. Despite that, the uncertainties of the XPS did not allow a clear and unique identification of single bonds, but a series of possible bonding with binding energy close to the measured one.

Analyzing the C1s spectra of the two measurements (untreated sample, Figs. 6.2.1a-b) it results that each one consists of one major peak centered near 284.7 eV, with an asymmetry on the high binding energy side, indicating the presence of carbon atoms with three different binding energies. Due to the availability of dedicated software it was possible to decompose the spectra, obtaining two well-defined peaks (centered respectively near 284.7 eV and 285 eV) and a very small/broaden one (not considered), see figs. 6.2.1a-b.

The most abundant element is of course carbon, mainly present as C-C (sp² hybridized) and in a minor part as C-C (sp³ hybridized) with different values between the two measured spots: this underlines the not-homogeneous nature of the graphite sample, especially on the surface; an influence from the sample preparation is not excluded. However, the close bonding energies of the electrons do not allow a clear identification of the peaks, taking into account also the uncertainty of the measuring equipment, so at the energy of 285 eV can correspond: C-C sp³, C-H and C-N. The broadening of the sp² peak is presumably related to the not perfect lattice, possibly distorted by vacancies or deformations also due to the presence of interstitials atoms: it has to be kept in mind that XPS analyses cover only the first nanometers of the sample surface, so a perfect structure is difficult to achieve during the sample preparation. Concerning the O1s spectra of the untreated sample ("AVR square 0" in figs. 6.2.1.c-d): it was possible to identify a peak around 532.9 eV, after having slightly shifted the spectra. The assigned bonding resulted in an ether structure C-O-C, confirmed also by the C1s spectra.

A summary of the calculated values and assigned bonding are reported in table 6.2.1.

AVR#0 light spot

Peakname	E _B /eV	Fläche/cps-eV	Empf.-Fakt.	Korr. Fläche	Konz./At.-%	
C-C sp ²	284.5	7099.4216	0.314	22609.623	71.99	97.74
C-H, C-N, C-C sp ³	285.02	1997.7357	0.314	6362.2157	20.26	
C-OH, C-O-C	286.25	541.66051	0.314	1725.0334	5.49	
C-O-C, (ads. H ₂ O)	532.74	519.26310	0.733	708.40805	2.26	2.26

AVR#0 dark spot

Peakname	E _B /eV	Fläche/cps-eV	Empf.-Fakt.	Korr. Fläche	Konz./At.-%	
C-C sp ²	284.5	5844.1164	0.314	18611.835	66.95	97.58
C-H, C-N, C-C sp ³	284.95	2150.2592	0.314	6847.9593	24.63	
C-OH, C-O-C	286.15	524.04590	0.314	1668.9360	6	
C-O-C, (ads. H ₂ O)	532.82	491.13287	0.733	670.03120	2.41	2.41

Table 6.2.1: Results from XPS analysis of untreated AVR graphite sample

Concerning the treated sample, the results are reported in table 6.2.2.

AVR#1 light spot

Peakname	E _B /eV	Fläche/cps-eV	Empf.-Fakt.	Korr. Fläche	Konz./At.-%	
C-C sp ²	284.5	5800.2487	0.314	18472.129	68.54	97.09
C-H, C-N, C-C sp ³	285.02	2014.0401	0.314	6414.1405	23.8	
C-OH, C-O-C	286.26	401.57064	0.314	1278.8873	4.75	
-OH-, C-O-C	532.23	233.53462	0.733	318.60111	1.18	2.92
ads. H ₂ O	533.54	181.21487	0.733	247.22356	0.92	
organics?	535.28	71.629444	0.733	97.720934	0.36	
organics?	537.58	89.901802	0.733	122.64911	0.46	

AVR#1 dark spot

Peakname	E _B /eV	Fläche/cps-eV	Empf.-Fakt.	Korr. Fläche	Konz./At.-%	
C-C sp ²	284.5	5008.9744	0.314	15952.148	64.92	94.53
C-H, C-N, C-C sp ³	285.03	1870.8390	0.314	5958.0861	24.25	
C-OH, C-O-C	286.27	413.38790	0.314	1316.5219	5.36	
-OH-, C-O-C	532.35	323.62978	0.733	441.51403	1.8	5.48
ads. H ₂ O	533.58	397.15764	0.733	541.82488	2.21	
organics?	536.08	88.369362	0.733	120.55847	0.49	
organics?	538.18	176.80299	0.733	241.20462	0.98	

Table 6.2.2: Results from XPS analysis of a thermal-treated AVR graphite sample

Without going too deep in detail in the description of the calculated values for the treated sample, a comparison with the former analysis is performed (spectra reported in figs. 6.2.2.a-e). The results obtained before and after the treatment (tabs. 6.2.1-2) show marked variations in the relative concentrations. In particular, for what concerns the C-C sp²-bond it was measured a

decrease of 1-3 %, leading to the conclusion that a less pure superficial composition has been created after thermal treatment¹⁷. An important difference can be seen also in the C-O-C values, slightly decreased, together with the appearance of some unidentified organics in the order of 0.5-1%. The total oxygen concentration increased up to 5.5% (it was maximum 2.4 % in the virgin untreated sample).

An element was also detected but left out of the Tables 6.2.1-2: Chlorine. The reason behind its exclusion stands on the high uncertainty of the measurements. By observing Figs. 6.2.2f-g it can be noticed that Cl2p has been measured in a relative concentration close to the detection limit of the instrument. It follows that a numerical approach for that element is not possible, but a qualitative evaluation can be performed nevertheless. In fact, after thermal treatment, the Cl2p peak disappeared completely (see Figs. 6.2.2h-i): a removal of Chlorine occurred, but it was not quantifiable.

An important observable peak after thermal treatment (see Figs. 6.2.2e-h-i) reveals the presence of calcium, but it was not possible assigning it to a specific bonding. The fact that calcium has been measured in both spots with different concentrations can lead to think that it is not homogeneous on the surface: some SEM measurements confirmed this observation (fig. 6.1.18).

The interpretation of the results did not allow identifying the bonding of nitrogen, chlorine and calcium. This is due to the fact that electron binding energies are very close to each other. In addition, the small amounts have increased the difficulties in the interpretation.

It can be found, anyway, a parallelism with the results obtained with other analysis, for example with SIMS (section 6.1). For what concerns the untreated specimens, the presence of bonded oxygen is confirmed (as C-O and C-O-C), at least for the first nanometers of the sample. This fact could be explained in three ways:

- Oxygen and nitrogen are already embedded in graphite, due to the manufacture process;
- Oxygen and nitrogen are coming from the sample's preparation procedure: the examined specimens were prepared by dry cutting, experiencing so high local temperatures, especially on the surface; being such preparation a sort of treatment in air, it is possible

¹⁷ The sentence is referred, however, to the very first layers of the graphite structure.

that the specimen has been influenced, revealing during the analysis higher concentrations of oxygen and nitrogen than the ones originally present in the graphite;

- Oxygen and nitrogen come from the prolonged exposure of the sample to the ambient air;

Considering some PGNAA analyses, the nitrogen content in graphite is about 120 ppm,¹⁸ but that measurement was referred to the total specimen without considering an eventual inhomogeneous distribution in the porous matrix. Takahashi [19] reported that nitrogen is concentrated the more on the superficial layers, confirmed here also by SIMS analyses (section 6.1).

Regarding the results of thermal treatment at high temperatures in argon (with very low amounts of water), it was noticed with SIMS (section 6.1) a strong increase in the superficial concentration of oxygen and, on the other side, a partial removal of nitrogen and chlorine from the surface, results confirmed also from the presented XPS results, even though in a less precise way. In conclusion, further studies are necessary to better understand the nitrogen bonding with graphite.

Concerning oxygen, after thermal treatment it was measured an increase on the surface concentration. In particular the already present C-O-C ether structure did not increase but, on the other side, some unidentified organics appeared. An overall increase of oxygen on the surface is confirmed by SIMS analysis (section 6.1) and by the thermal treatment's boundary conditions: in particular, the reaction of graphite with water is believed to be the responsible of what has been observed.

In conclusion, XPS analyses have confirmed the effective removal of chlorine after the thermal treatment, even though the uncertainties were high; the presence of bonded oxygen on the surface has been proven, with an increase as a consequence of the treatment's boundary conditions; some impurities as calcium were detected after thermal treatment, supporting the findings of SIMS analyses.

More investigations are necessary, however, to better understand the bonding of some elements as calcium, nitrogen and chlorine.

¹⁸ Mole fractions from Zsolt Révay, PGNAA December 2010, Nuclear Research Department, Institute of Isotopes, HAS, Budapest, Konkoly-Thege Miklosutca 29-33. 1121 Hungary

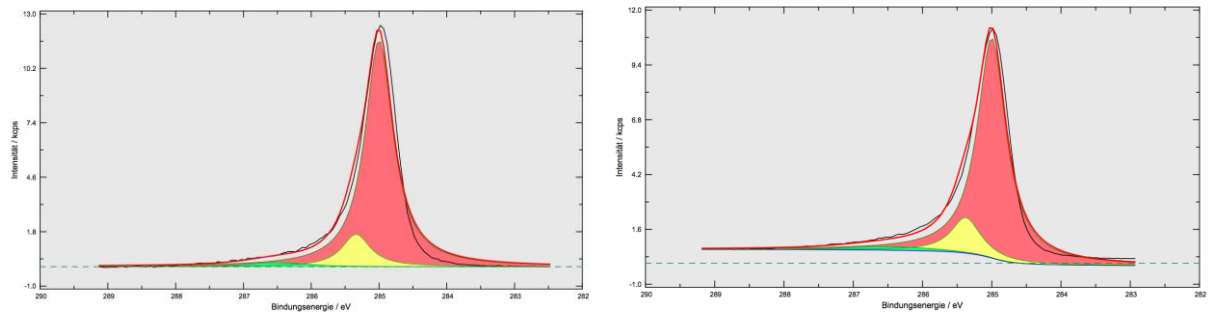


Figure 6.2.1.a-b: C1s Spectra of virgin AVR graphite sample, "light spot" (left) "dark spot" (right)

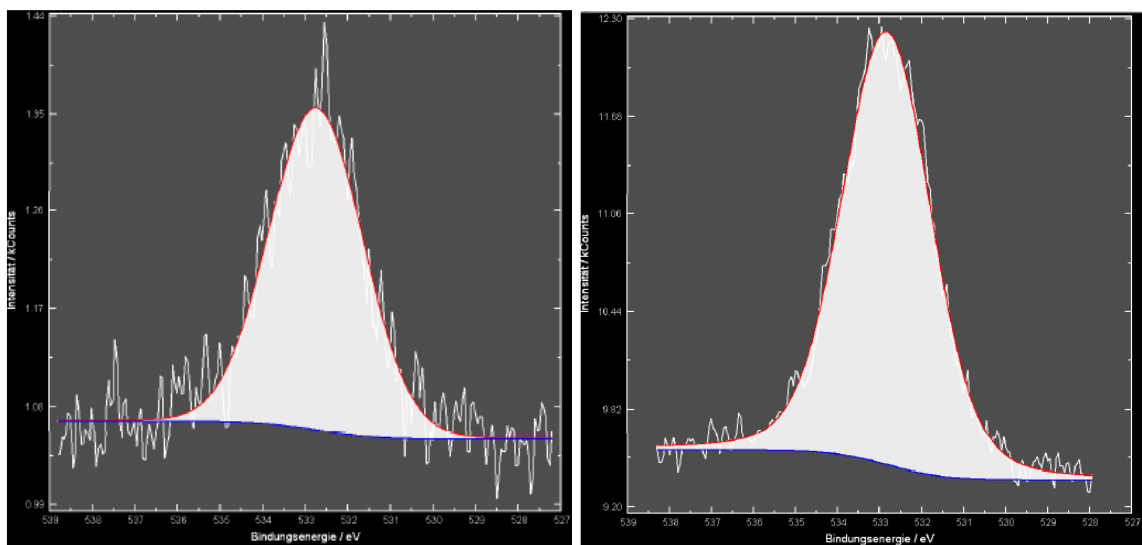


Figure 6.2.1.c-d: O1s Spectra of virgin AVR graphite sample, "light spot" (left) "dark spot" (right)

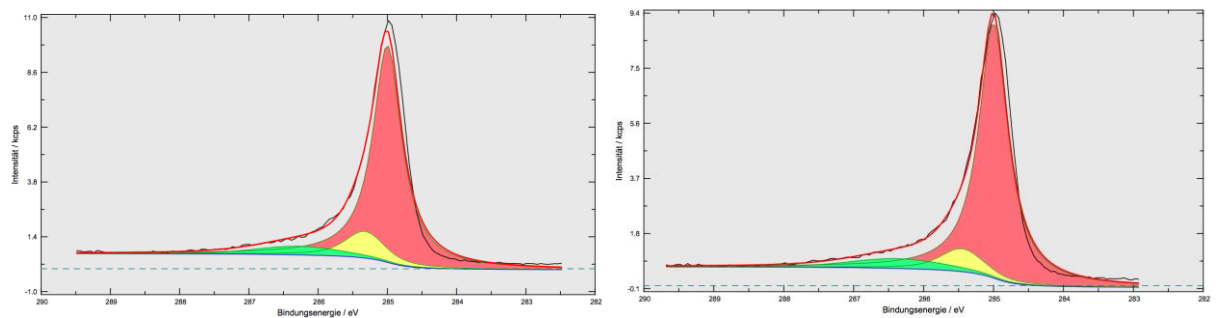


Figure 6.2.2.a-b: C1s Spectra of thermally treated AVR graphite sample, "light spot" (left) "dark spot" (right)

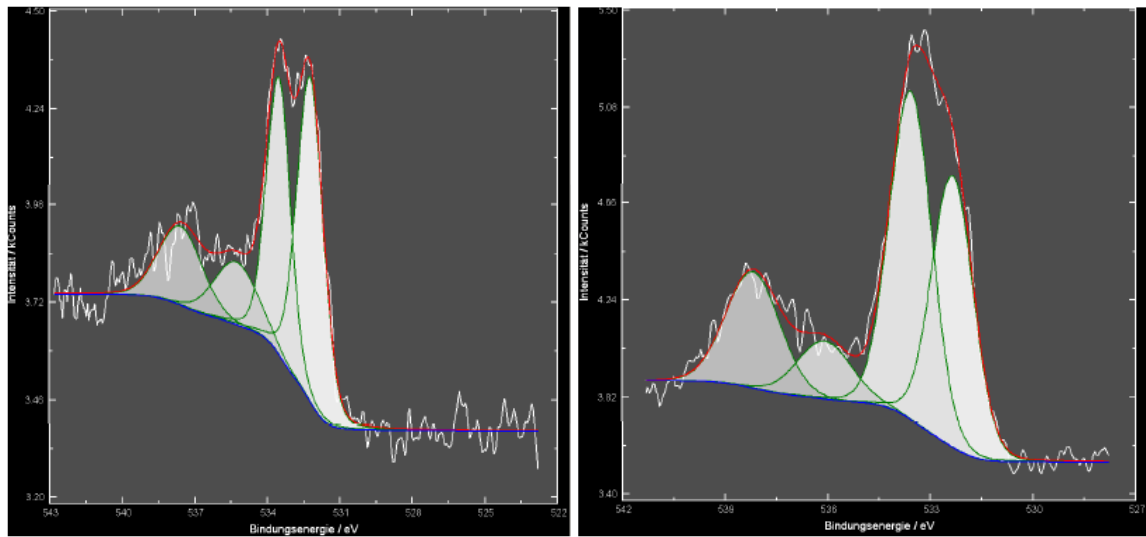


Figure 6.2.2.c-d: O1s Spectra of thermally treated AVR graphite sample, "light spot" (left) "dark spot" (right)

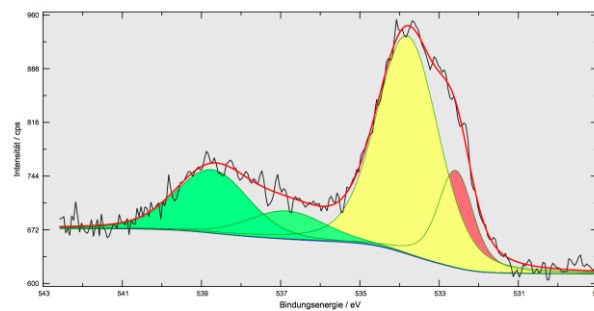


Figure 6.2.2e: Ca2p3 Spectra of thermally treated AVR graphite sample, "dark spot"

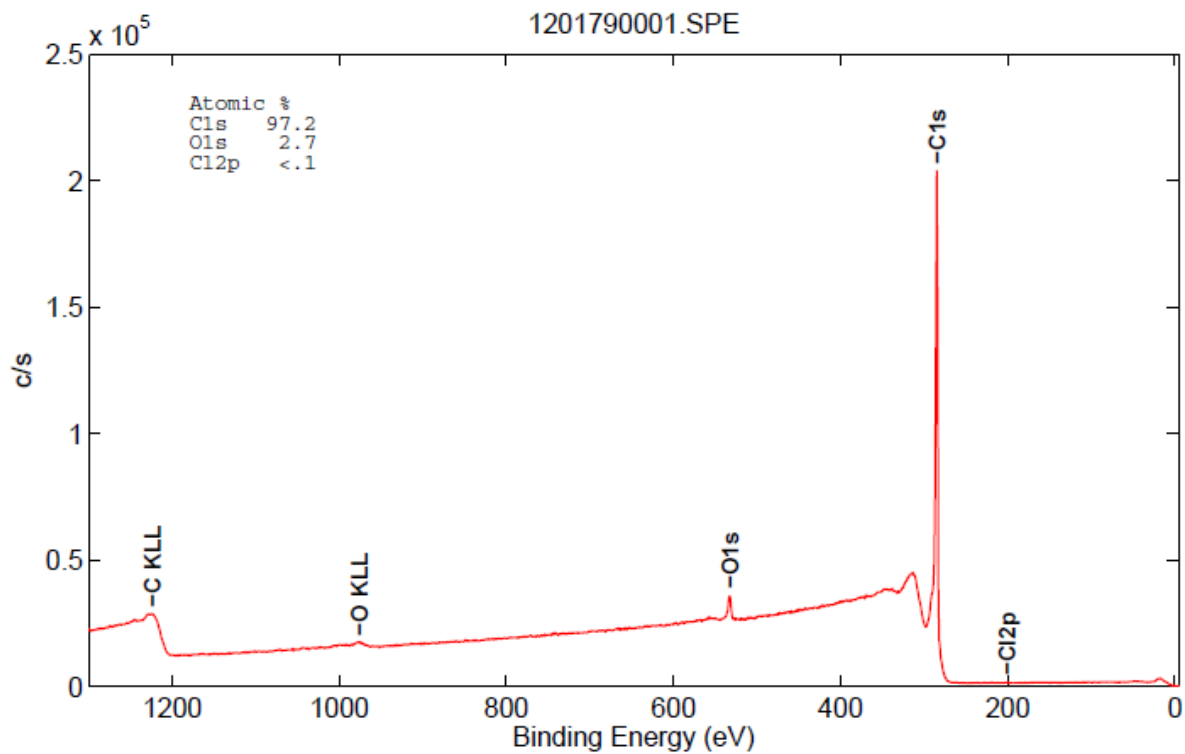


Figure 6.2.2f: Overall Spectra of virgin AVR graphite sample, "light spot"

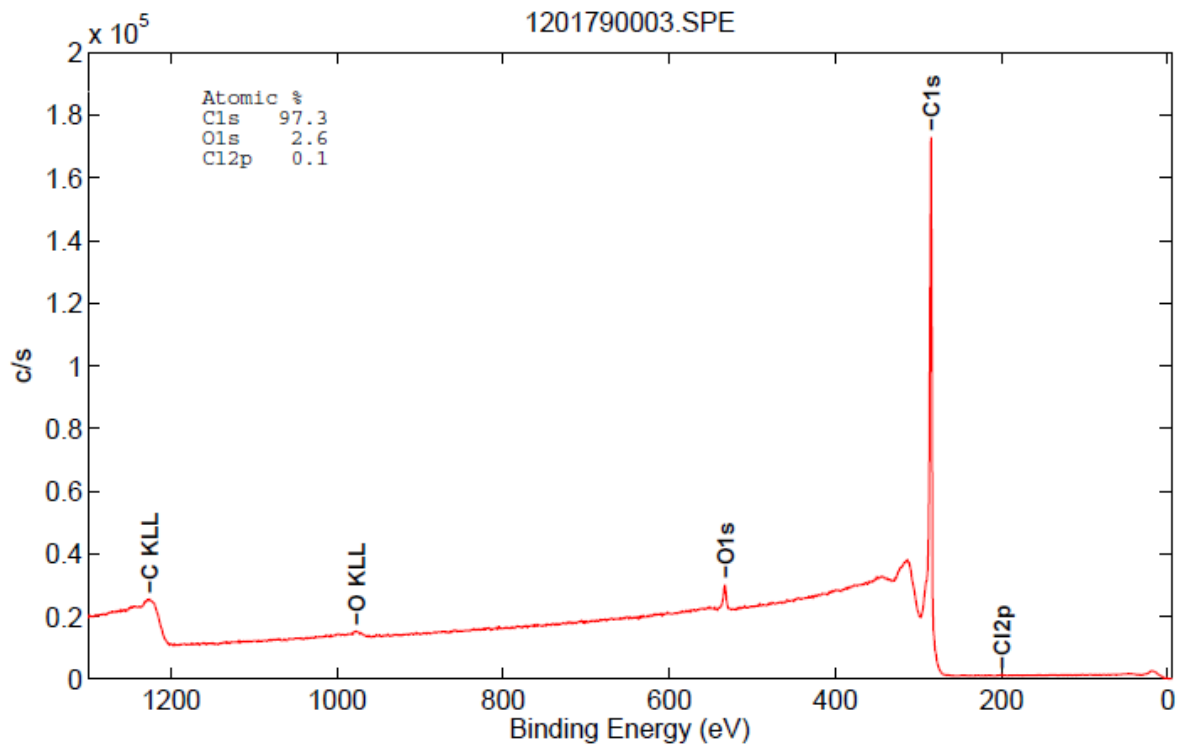


Figure 6.2.2g: Overall Spectra of virgin AVR graphite sample, "dark spot"

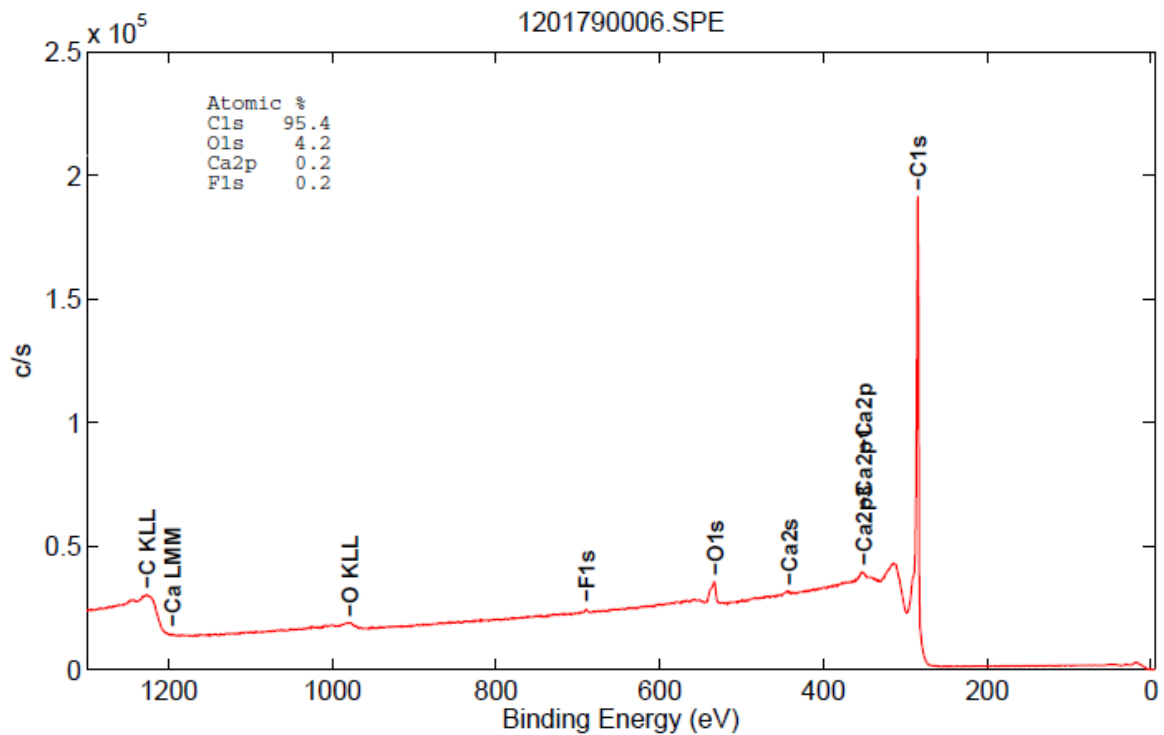


Figure 6.2.2h: Overall Spectra of thermally treated AVR graphite sample, "light spot"

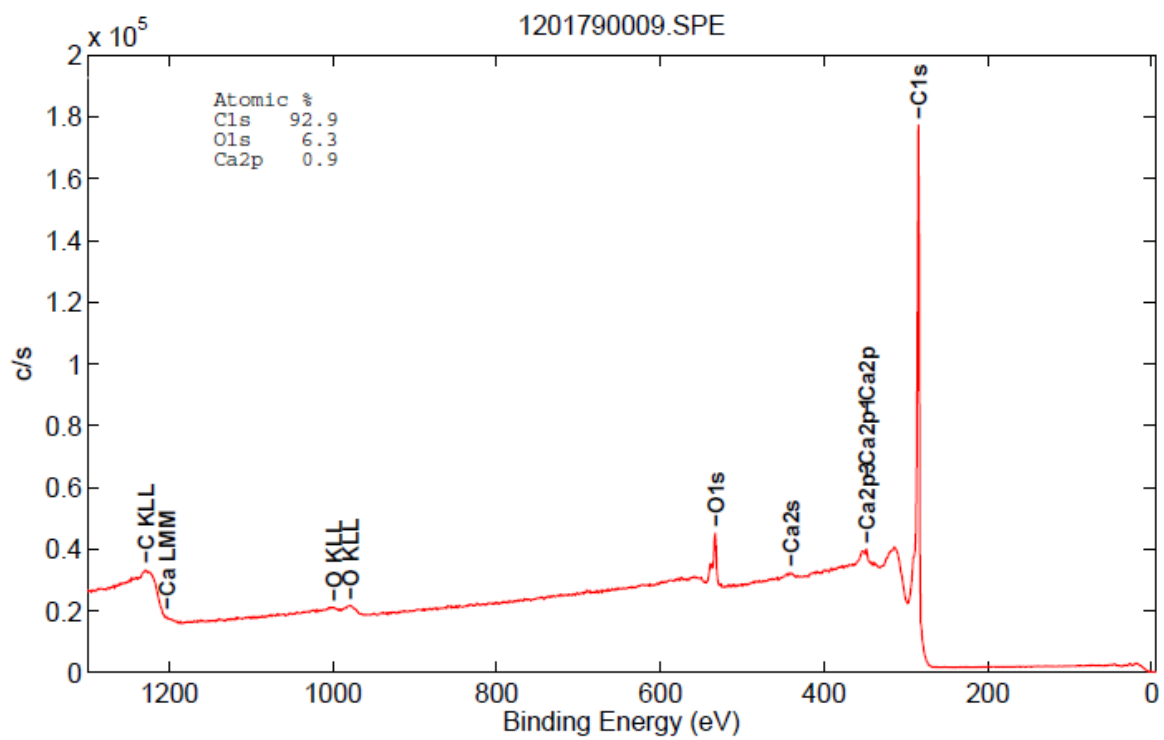


Figure 6.2.2i: Overall Spectra of thermally treated AVR graphite sample, "dark spot"

7. Evaluation of Treatment Options

It is shown in this report that radionuclides can be removed from neutron-irradiated nuclear graphite by several chemical and physical methods. By observing the progress and the products of these processes, the original locations and the chemical forms of these radionuclides in graphite can be deduced. If the chemical forms are known, the chemical bonds are also known. If the chemical bonds are known, the release or retention characteristics of radionuclides in neutron-irradiated nuclear graphite can be predicted. With this knowledge, methods for the conditioning of spent nuclear graphite can be developed.

The following can be said about the removability of radionuclides from neutron-irradiated nuclear graphite in detail: Tritium is removable nearly completely by simple thermal treatment in inert gases. This is possible because tritium is a small atom which is different from the carbon atoms and which can diffuse easily through the graphite matrix (also as tritiated water). Adsorbed tritiated water can be desorbed and covalently bound tritium can be pyrolysed by heating. For this process, temperatures higher than 1000 °C are necessary. Below 1000 °C, graphite is a good tritium accumulator.

The most challenging radionuclide in nuclear graphite is radiocarbon (^{14}C) because from the chemical point of view, there is no difference between radiocarbon and natural carbon (^{12}C , ^{13}C). The chemical reactions of radiocarbon and natural carbon are the same. But in neutron-irradiated nuclear graphite, there are regions of high enrichment of radiocarbon. If methods are available to oxidise these regions selectively, this part of radiocarbon can be removed selectively. Such specially engineered methods have to be designed in the future. Another part of radiocarbon is not removable from the graphite matrix because it is homogeneously distributed in the graphite matrix. There is no difference between radiocarbon and other carbon isotopes.

Those radionuclides which can be removed from neutron-irradiated nuclear graphite most easily and most quickly are the metallic radionuclides. If the metallic radionuclide is bound in graphite as water-soluble ion (like Cs^+), the radionuclide is removable by action of water or diluted acids. The effectiveness of this process is only dependent on the exfoliation grade of the graphite sample, that means dependent on the grade with which water or aquatic solutions can penetrate the pore system. If the metallic radionuclide is bound in graphite as metal-carbon compound (like Co-C), the radionuclide is not removable by simple action of water or diluted acids. In this case, strong oxidising acids (like mixtures of concentrated nitric and sulphuric acid) are necessary but these agents often cause strong corrosions of the graphite matrix. Otherwise, the graphite matrix is a good barrier for these carbidic radionuclides so it may make sense to not remove them.

8. Summary

The locations and the chemical forms (chemical bonds) of radionuclides in neutron-irradiated nuclear graphite have been determined in order to develop principal strategies for the management of graphitic nuclear waste. Due to the relatively low concentration of radionuclides in neutron-irradiated nuclear graphite (< 1 ppm) direct spectroscopic methods are not applicable to investigate chemical structures. Therefore, methods by analogy have been applied. Such methods are investigations of the chemically detectable precursors of radionuclides in neutron-irradiated nuclear graphite and subsection of irradiated graphite to different chemical reactions followed by measurements of the radionuclide-containing reaction products by sensitive radiochemical methods. The paper discusses the applicability of these methods. The radionuclides investigated in this study can be divided into three parts: tritium, radiocarbon and metallic activation and fission products. Tritium can be bound in neutron-irradiated nuclear graphite as strongly adsorbed tritiated water (HTO), in oxygen-containing functional groups (e.g. C—OT) and as hydrocarbons (C—T). Radiocarbon is covalently bound with the graphite structure. The activity can be described by a homogeneously distributed part and a heterogeneously distributed part (enriched on surfaces or in hotspots). Metallic radionuclides can be bound as ions or covalent metal-carbon compounds. The distribution of all these radionuclides is mainly dependent on the distribution of their inactive precursors.

9. References

- [1] J. Fachinger, W. von Lensa, T. Podruchina, Decontamination of nuclear graphite, *Nucl. Eng. Des.* 238 (2008) 3086–3091.
- [2] ANSYS Workbench, ANSYS, Inc., Release 12.0.
- [3] R.E. Nightingale (Ed.), *Nuclear graphite*, Academic Press, New York, 1962.
- [4] R. Dovesi, C. Pisani, F. Ricca, C. Roetti, Chemisorption of periodic over-layers of atomic nitrogen on graphite, *Surface Sci.* 77 (1978) 409–415.
- [5] T. Fromherz, C. Mendoza, F. Ruette, Chemisorption of atomic H, C, N and O on a cluster-model graphite surface, *Mon. Not. R. Astron. Soc.* 263 (1993) 851–860.
- [6] R.H. Telling, M.I. Heggie, Radiation defects in graphite, *Phil. Mag.* 87 (2007) 4797–4846.
- [7] R. Nabbi, H. Probst, Molecular dynamic simulation of the transport behavior of C-14 in irradiated nuclear graphite, Irradiation damage and ^{14}C formation in nuclear graphite. Joint meeting in conjunction with the FP7 CARBOWASTE program, Manchester, 28th Nov 2012.
- [8] P.G. Fischer, R. Hecker, H.D. Röhrig, D. Stöver, Zum Verhalten von Tritium in Reaktor-graphiten, *J. Nucl. Mater.* 64 (1977) 281–288.
- [9] M. Florjan, Dekontamination von Nukleargraphit durch thermische Behandlung, PhD thesis, Rheinisch-Westfälische Technische Hochschule Aachen, 2009.
- [10] W. Delle, K. Koizlik, H. Nickel, Graphitische Werkstoffe für den Einsatz in Kernreaktoren. Teil II: Polykristalliner Graphit und Brennelementmatrix, Karl Thieme AG, München, 1983.
- [11] R. Nieder, W. Sträter, Langzeitverhalten von Verunreinigungen in einem HTR-Primärkreislauf, *VGB Kraftwerkstechnik* 68 (1988) 755–760.
- [12] N. Nakashio, M. Nishikawa, Study on quantification of the system effects of tritium, *Fusion Technol.* 33 (1998) 287–197.
- [13] K. Katayama, M. Nishikawa, Release behavior of tritium from graphite material, *Fusion Sci. Technol.* 41 (2002) 53–62.
- [14] R. Larciprete, S. Gardonio, L. Petaccia, S. Lizzit, Atomic oxygen functionalization of double walled C nanotubes, *Carbon* 47 (2009) 2579–2589.
- [15] M.S. El-Genk, J.-M.P. Tournier, Development and validation of a model for the chemical kinetics of graphite oxidation, *J. Nucl. Mater.* 411 (2011) 193–207.
- [16] C. MacKay, M. Pandow, P. Polak, R. Wolfgang, The elementary chemistry of atomic carbon, in: *Chemical effects of nuclear transformations*, Vol. 2, International Atomic Energy Agency, Vienna, 1961, pp. 17–26.
- [17] L. Tian, M. Wen, L. Li, J. Chen, Disintegration of graphite matrix from the simulative high temperature gas-cooled reactor fuel element by electrochemical method, *Electrochim. Acta* 54 (2009) 7313–7317.
- [18] L. Tian, M. Wen, J. Chen, Analysis of off gas from disintegration process of graphite matrix by electrochemical method, *Atomic Energy Sci. Technol.* 44 (2010) 660–665.
- [19] R. Takahashi, M. Toyahara, S. Maruki, H. Hueda, T. Yamamoto, "Investigation of morphology and impurity of nuclear grade graphite, and leaching mechanism of carbon-14", p.7

- [A2] Cooper, B.E., S.S. Hill, and M. Tomlinson, Collected BEPO Graphite Oxidation Monitoring Data (November 1957 to December 1959), U. Harwell, Editor. 1961, National Archives (unclassified) p. 124.
- [A3] Thewlis, J., British Experimental Pile (BEPO) - Graphite Supplies, A.E.R.E. Harwell, Editor. 1945, National Archives (unclassified).
- [A4] Colmer, F.C.W., Density Measurements on Canadian Graphite used in BEPO, A.E.R.E. Harwell, Editor. 1946, National Archives (unclassified)
- [A5] Dickinson, J.L., et al., BEPO Wigner Energy Release, in A/CONF. 1958. p. 95.
- [A6] Wickham, A.J., Deposition of Graphite Samples from BEPO as Supplied to NIREX. 2007.

-
- 1 Bradbury, D., and Wickham, A.J. *Graphite Decommissioning: Options for Graphite Treatment, Recycling, or Disposal, including a discussion on Safety-Related Issues*. EPRI, Palo Alto, CA: 2006. 1013091.
 - 2 IAEA TECDOC-1521. *Characterization, Treatment and Conditioning of Radioactive Graphite from Decommissioning of Nuclear Reactors*. September 2006.
 - 3 Bradford, M.R., and Steer, A.G. A structurally-based model of irradiated graphite properties. *Journal of Nuclear Materials* 381 (2008) 137–144.
 - 4 Wickham A.J., "Caring for the Graphite Cores"; Proc. Seminar 'The Review of Safety at Magnox Nuclear Installations', London, March 1989, I.Mech E. pp. 79-8715
 - 5 Marsden, B.J., Hopkinson, K, L., Wickham, A.J. (March 2002) The Chemical Form of Carbon-14 within Graphite. Serco Assurance. SA/RJCB/RD03612001/R01 Issue 4.
 - 6 Marsden, B.J., Production, Location and Retention of Carbon 14 in irradiated Graphite, A report for UKAEA, SERCO Assurance, SA/RJCB/RD03510001/R01 Issue 2, July 2002.
 - 7 Standring, J., Ashton, B.W., The Effect of Radiolytic Oxidation by Carbon Dioxide on the Porosity of Graphite, *Carbon*, 3, 157-165, 1965.
 - 8 Sun, L., Hodgkins, A., Marrow, J., Fok, A.S.L., and Marsden, B.J. AN EXPERIMENTAL STUDY ON THE POROSITY NETWORKS IN NUCLEAR GRAPHITE in 2nd International Topical Meeting on HIGH TEMPERATURE REACTOR TECHNOLOGY. Beijing, CHINA, September 22-24, 2004.